
The Nature of AGN-host Co-evolution

Li Shao



Munich 2013

The Nature of AGN-host Co-evolution

Li Shao

Dissertation
an der Department of Physics
der Ludwig-Maximilians-Universität
München

vorgelegt von
Li Shao
aus Hangzhou, Zhejiang, China

München, den Oct. 23, 2013

Erstgutachter: Prof. Dr. Simon White

Zweitgutachter: Prof. Dr. Ralf Bender

Tag der mündlichen Prüfung: Dec. 2, 2013

Contents

Acronyms and Abbreviations	xi
Abstract	xiii
1 Background	1
1.1 Active Galactic Nuclei	1
1.1.1 Supermassive Black Hole and Accretion Disk	1
1.1.2 Corona and X-ray Emission	2
1.1.3 Jet	3
1.1.4 Broad- and Narrow-line Regions	3
1.1.5 Torus and AGN Unification Model	4
1.1.6 The AGN Family	5
1.2 AGN Host Galaxies	6
1.2.1 Normal Galaxies	7
1.2.2 AGNs in Green Valley and Red Sequence	8
1.2.3 Gas Inflow	9
1.2.4 Outflow and AGN feedback	10
1.3 Observational Facilities	11
1.3.1 <i>SDSS</i>	11
1.3.2 <i>WISE</i>	12
1.3.3 <i>Swift</i> BAT	12
1.3.4 <i>IRAS</i>	12
1.3.5 <i>Chandra</i> ACIS	13
1.3.6 <i>Herschel</i> PACS	13
2 AGN Torus Emission and Host Properties	15
2.1 Introduction	15
2.2 Data	16
2.2.1 <i>SDSS</i> Spectroscopic Catalog and <i>WISE</i> Counterparts	16
2.2.2 Optical Classification	19
2.2.3 <i>SDSS</i> quasars	22
2.3 Mid-IR colors of local galaxies	22
2.3.1 Stellar emission	22

2.3.2	AGN host galaxies	24
2.4	Mid-IR properties of local AGNs	27
2.4.1	AGN IR luminosity	29
2.4.2	AGN emissivity and host properties: comparing optical and IR . . .	32
2.5	AGNs selected by mid-IR colors	35
2.5.1	<i>WISE</i> IR AGN selection	35
2.5.2	The SEDs of IR color selected AGNs	37
2.5.3	Optical properties of IR color selected AGNs	39
2.5.4	Optically-unidentified IR color selected AGNs	39
2.6	Discussion	41
3	AGNs and Galaxy Interactions	43
3.1	Introduction	43
3.2	Data and Results	44
3.3	Discussion	46
4	AGN Activity and Star Formation at High Redshift	49
4.1	Introduction	49
4.2	Data	50
4.2.1	Local AGNs	50
4.2.2	AGNs at High Redshift	51
4.3	Results	52
4.3.1	Far-IR Luminosity as a Function of Redshift	52
4.3.2	Far-IR Luminosity as a Function of X-ray Obscuration	57
4.4	Discussion	58
5	Summary and Prospective	63
	Thanks	89

List of Figures

2.1	Definition of stellar mass complete sample	17
2.2	General properties of S1 and S2 galaxies	20
2.3	<i>WISE</i> luminosity versus stellar mass for normal galaxies	23
2.4	[3.4] – [4.6] versus 4000 Å break for normal galaxies	25
2.5	<i>WISE</i> color-color diagram	26
2.6	<i>WISE</i> colors versus 4000 Å break for AGNs	28
2.7	Cumulative number distribution of AGNs over IR luminosities	30
2.8	AGN IR luminosities versus [OIII] luminosities	31
2.9	Host properties of Seyfert galaxies	33
2.10	Host properties of IR-bright LINERs	34
2.11	The fraction of optical AGNs as a function of χ^2 cut	36
2.12	IR selected AGNs on the <i>WISE</i> color-color diagram	37
2.13	Median SEDs of IR selected AGNs	38
2.14	AGN/host properties of IR AGNs	40
3.1	Neighbor counts of Seyfert galaxies	45
3.2	Neighbor counts against various properties	47
4.1	Redshift distribution of GOODS-N X-ray AGNs	52
4.2	Far-IR luminosities of AGN hosts as a function of redshift	53
4.3	Optical to far-IR SEDs of $z \sim 1.2$ AGNs	54
4.4	Far-IR luminosity as a function of redshift and X-ray luminosity	56
4.5	Far-IR luminosity as a function of X-ray column density	57
4.6	Host star formation rate versus AGN luminosity	58
4.7	Host star formation rate versus AGN luminosity for <i>SDSS</i> optical AGNs	61

List of Tables

2.1	The stellar mass bins of local galaxy samples	18
2.2	The <i>WISE</i> detection rates of local galaxy samples	19
2.3	Optical classification of local galaxy sample	21
2.4	IR selected AGN samples	36
4.1	Average far-IR luminosities of different AGN subsamples	55

Acronyms and Abbreviations

Acronyms and abbreviations used in the text are listed here.

ACIS, Advanced CCD Imaging Spectrometer
ADAF, advection-dominated accretion flow
AGB, asymptotic giant branch
AGN, active galactic nucleus
BAT, Burst Alert Telescope
BH, black hole
BPT, Baldwin, Phillips & Terlevich
BLR, broad-line region
CCD, charge-coupled device
CDFN, *Chandra* Deep Field North
ESA, European Space Agency
FR, Fanaroff-Riley
FWHM, full width at half maximum
GOODS, the Great Observatories Origins Deep Survey
HIFI, the Heterodyne Instrument for the Far Infrared
IR, infrared
IRAC, the Infrared Array Camera
IRAS, Infrared Astronomical Satellite
LINER, low-ionization nuclear emission-line region
MIPS, the Multiband Imaging Photometer for *Spitzer*
NASA, National Aeronautics and Space Administration
NGC, New General Catalogue of Nebulae and Clusters of Stars
NLR, narrow-line region
PACS, the Photodetector Array Camera and Spectrometer
PEP, the PACS Evolutionary Probe
PSF, point spread function
QSO, quasi-stellar objects
SDSS, Sloan Digital Sky Survey
SED, spectral energy distribution
SNR, signal-to-noise ratio

SPIRE, the Spectral and Photometric Imaging Receiver

SSFR, specific star formation rate

ULIRG, ultra luminous infrared galaxy

UV, ultraviolet

WISE, the Wide-field Infrared Survey Explorer

Abstract

The central black hole and galaxy co-evolution is one of the most important open issues in astrophysics: whether the link between the central black hole growth and galaxy formation exists, and if yes, how the link is established. In local Universe, combining *SDSS* and *WISE* data leads to a sample of ~ 30000 optically selected AGNs. The nuclear IR emission, obtained by subtracting host component from the total IR luminosities, is found to be linearly correlated with the [OIII] line luminosities for 4 orders of magnitude, as a good indicator of the central black hole accretion rate. It is found that a major fraction of the total AGN radiation output comes from the galaxies with young stellar population ($D_n(4000) < 1.6$), confirming the strong AGN-host connection established in previous works. The emissivity distributions from the optical and IR indicators are similar for Seyfert 2 galaxies and IR-bright LINERs, supporting the validity of the standard AGN unification model. And the IR torus emission helps to reveal the hidden connection between AGN and galaxy mergers, by the excessive number of companions around the IR-brighter Seyfert galaxies when the clustering effect of star formation is carefully removed. This implies the galaxy mergers may be important to regulate the AGN-host co-evolution for local Seyfert galaxies. The study of hard X-ray selected local AGNs gives consistent result with the *SDSS* exercises, except that in low luminosity regime the AGN-host coupling appears to break down. The *Chandra-Herschel* data extend the study to redshift of 2. It also shows that the central black hole accretion rate and the host total star formation rate is probably only strongly correlated for high luminosity AGNs. At higher redshifts, the AGN-host connection seems weakened due to the elevated host star formation level. The increasing average host star formation rate with increasing redshift is consistent with current high redshift observations of normal galaxies. The AGN-host co-evolution may be redshift dependent.

Zusammenfassung

Die gemeinsame Entwicklung von Galaxien und ihrer zentralen schwarzen Löchern ist eines der wichtigsten aktiven Arbeitsgebiete der Astrophysik: Gibt es eine Verbindung zwischen dem Wachstum schwarzer Löcher und der Entstehung der Galaxien, und wenn ja, warum? Für das lokale Universum liefert die Kombination von WISE und SDSS Daten etwa 30000 optisch ausgewählte aktive galaktische Kerne (active galactic nuclei: AGN). Die zentrale infrarot Emission der AGN wurde durch das Entfernen der Galaxienkomponente (host) von der Gesamtemission ermittelt. Sie korreliert linear mit der Leuchtkraft der [OIII] Linie über vier Größenordnungen, als guter Indikator der Akkretionsrate des zentralen schwarzen Lochs. Ein Großteil der gesamten AGN Strahlung kommt von Galaxien mit jungen stellaren Populationen ($D_n(4000) < 1.6$), was die in vorangegangenen Arbeiten festgestellte enge AGN-host Verbindung bestätigt. Die Verteilung der Emissivität, bestimmt mittels Indikatoren im optischen und infraroten Licht, ähnelt der von Seyfert 2 Galaxien und infrarot-leuchtkräftigen LINERs. Diese Ergebnisse unterstützen die Gültigkeit des Vereinheitlichungsmodells für AGN. Die infrarot Emission des Torus lässt die versteckte Verbindung zwischen AGN und Galaxienverschmelzungen erkennen, angezeigt durch die - nach sorgfältiger Einbeziehung des Klumpungseffekts durch Sternentstehung - beobachtete übermäßig hohe Anzahl von Begleitgalaxien infrarot leuchtkräftiger Seyfert Galaxien. Das deutet auf die wichtige Rolle von Galaxienverschmelzungen bei der Regulierung der gemeinsamen AGN-host Entwicklung lokaler Seyfert Galaxien hin. Eine Untersuchung lokaler AGN, die aufgrund ihrer energiereichen Röntgenstrahlung ausgewählt wurden, stimmt mit der SDSS Studie überein. Allerdings bricht die AGN-host Verbindung bei niedrigen Leuchtkräften zusammen. Die Chandra/Herschel Daten dehnen die Studie bis Rotverschiebung $z = 2$ aus. Es zeigt sich, dass die Akkretionsrate der schwarzen Löcher möglicherweise nur bei hohen AGN Leuchtkräften mit der gesamten host-Sternentstehungsrate korreliert. Bei höheren Rotverschiebungen scheint die AGN-host Verbindung durch höhere Sternentstehungsraten der hosts geschwächt zu sein. Der Anstieg der mittleren host-Sternentstehungsraten stimmt mit heutigen Beobachtungen normaler Galaxien bei hohen Rotverschiebungen überein. Die gemeinsame AGN-host Entwicklung könnte von der Rotverschiebung abhängig sein.

Chapter 1

Background

1.1 Active Galactic Nuclei

Active galactic nuclei (AGNs) are a special class of extragalactic objects. Historically they are first identified by their broad optical emission lines with width as large as 1000 km/s. Despite the debates in past years, the origin of these broad lines is now commonly agreed to be virialized ionized gas cloud bounded by deep gravitational potential well. Recently some techniques have been applied successfully to measure the size of the emission region and the total mass enclosed within the region [257, 196, 195, 26]. The results show clear evidence of the presence of extremely compact object in the center of the system. It is believed that this massive compact central object is in form of black hole (BH), which was originally suggested as a theoretical solution of a point mass, under the general relativity theory [71, 216]. In modern picture, AGNs are supermassive black holes, located in the center of galaxies and actively accreting materials.

1.1.1 Supermassive Black Hole and Accretion Disk

AGN is one of the most energetic phenomena in the Universe. The luminosity could be as high as $10^{47} \text{ erg s}^{-1}$, much higher than normal galaxies. This kind of enormous energy output is hard to explain with energy production mechanisms for stars, like nuclear reaction. Instead, it is agreed that the accretion-powered scenario can solve the problem. In this picture, the central black hole is accreting materials from its surrounding gas clouds. A substantial fraction of the gas kinetic energy and potential energy, which has to be removed to make the materials fall into the black hole, is converted into thermal energy and finally carried away by photons. The accretion processes may continue, as long as the gas supply is sufficient. The AGN activity can also be viewed as the growth of the supermassive black hole [229].

Theoretically the maximum accretion rate/radiation flux is limited by the balance of the inward gravity and outward radiation pressure, i.e. Eddington luminosity. In case of isotropic accretion, i.e. Bondi accretion, and the in-fall gas is mainly ionized hydrogen, the

luminosity upper limit is:

$$L_{\text{Edd}} = \frac{4\pi GMm_p c}{\sigma_T} \approx 1.3 \times 10^{38} (M/M_\odot) \text{ erg s}^{-1}. \quad (1.1)$$

However, Bondi accretion is unlikely the case in real AGNs. The in-fall materials usually have initial angular momentum so that they are more likely to form a flattened structure, or say accretion disk. In this type of accretion, the removal of the angular momentum of in-fall materials is crucial. In spite that the key physical mechanism is still unknown, several simplified models have successfully given good approximations to the final solution. The standard thin disk model is applicable to an optically thick but geometrically thin disk at moderate accretion rate [220]. The angular momentum is assumed to be transported by viscous dissipation from internal turbulence of the accreted gas. At higher accretion rate, it is probable that a thick disk model is necessary [1]. Different from radiation efficient thin disk, the vertical structure of thick disk is supported by heated gas that is not cooled down quickly. At lower accretion rate, on the other hand, it may be necessary to introduce an advection-dominated accretion flow (ADAF) model to explain some observational features of low-luminosity AGNs [179]. The accretion modes may affect the observable characteristics of AGNs. The transition between different accretion modes is observed in Galactic accretion systems, like X-ray binaries. But it is still uncertain for AGNs due to their much longer transition time scale and the difficulty to completely sample the whole AGN population.

The radiation from the accretion disk is expected to be a thermal component with typical temperature of $\sim 3 \times 10^4$ K (though it is possible that the accretion disk has multiple temperature components, at different radii), dominating the observed ultraviolet (UV) and optical continuum. It is corresponding to the observed “big blue bump” of typical quasars, peaking at $\sim 1100\text{\AA}$ [221].

1.1.2 Corona and X-ray Emission

In spite of the high temperature of the accretion disk, the thermal component is not sufficient to explain the observed X-ray flux [178]. It is suggested that the origin of the X-ray emission is the UV seed photons Comptonized by hot gas [106]. The hot gas is distributed around the accretion disk, as a natural extension of the accretion disk along the vertical direction, forming so called corona. The electrons in the corona can have relativistic speed so that the region must be very close to the black hole. The small size of corona can also be confirmed by the strong variability of X-ray on short time scale.

The Compton up-scattered X-ray continuum spectrum is close to a power-law with a high energy cut-off, corresponding to the thermal distribution of the scattering electron energy. A part of the X-ray emission is reflected by the accretion disk or some other dense materials. It worths to mention that the observed broad iron line at 6.4 keV is consistent with single emission line from reflected X-ray component, affected by a rotating black hole and relativistic beaming [81]. The successful modeling also implies the existence of the central black hole. The X-ray photons are also reprocessed by absorption [250]. It is often

necessary to add an absorption component into the models to better fit the observed X-ray spectra.

X-ray emission is commonly used to identify AGNs, especially at high redshift. As the X-ray emission is the common feature of the accretion disk and the high energy photons are less affected by external absorptions, X-ray based AGN sample is considered to be close to complete. But it should be noted that, for a special class of AGNs, the whole spectral energy distribution (SED) of which is dominated by the Doppler boosted jet emission, the observed X-ray fluxes have very different origin. This issue will be discussed in the Section 1.1.3.

1.1.3 Jet

Some of AGNs are also featured by their prominent radio emission. The AGNs are often divided into two major classes depending on their radio luminosities: radio-loud and radio-quiet. It is known that this radio component is synchrotron radiation from relativistic plasma. The plasma is observed as beamed outflow, or say jet. Though the mechanism to drive the jet out of central engine and to constrain the outflow in a small cone is still unknown, it is usually suggested that the magnetic fields are playing important role here. It is also a potential way to remove excessive angular momentum from the central part of the system.

Traditionally, there are two subclasses of galaxies classified purely according to the radio morphology of the galaxy. The Fanaroff-Riley class I (FR-I) galaxies are low-luminosity objects with compact core, while the FR-II objects have high luminosity and totally driven by the large radio lobes [84]. A hidden AGN is a natural explanation to the powerful radio jet if there is no optical/X-ray signatures, so they are also included into the AGN family.

As the jet is beamed and the materials are moving relativistically, when the jet is along the line of sight, the dramatic Doppler boosting can “amplify” the luminosity, and shift the radiation to higher energy bands. For those objects, including blazars, flat-spectrum radio quasars, the SED is usually dominated or strongly affected by the jet components: a synchrotron component covering radio to optical bands and an inverse Compton component in higher energy regime. The radiation is not directly linked with accretion disk continuum or other AGN emissions, hence it is difficult to integrate this specific class into the whole picture. In this thesis, these objects are explicitly excluded.

1.1.4 Broad- and Narrow-line Regions

As mentioned above, the first AGNs are identified by their broad emission lines. Typical broad emission lines are $H\alpha\lambda 6563$, $H\beta\lambda 4861$, $H\gamma\lambda 4340$, $Ly\alpha\lambda 1216$, etc. The Doppler widths of the broad lines are usually 10^3 to 10^4 km/s, suggesting that the broad lines are emitted from the very central region of the gravitational potential well (broad-line region, BLR), close to the black hole. In addition to the broad lines, it is often shown additional much narrower component at the wavelengths of these and of some other forbidden lines (like $[OIII]\lambda 5007$, $[OI]\lambda 6300$, $[SII]\lambda 6716$, $[SII]\lambda 6737$). The full-width half-maximum (FWHM) is

typically 400–500 km/s. Different from the variable broad lines, narrow lines are lack of variability. These features suggest that the narrow lines are emitted from a much larger region (narrow-line region, NLR), so that the local variability is canceled at larger scale, and farther away from the central black hole.

The origin of the emission lines is the recombination of ionized gas in BLR and NLR. The gas is ionized by the photons emitted from the hot accretion disk. The ionization rate, which is affected by the strength of the radiation field, and the recombination rate, which decides the emission line strengths, are balanced. In case of BLR, a correlation between AGN continuum luminosity and the broad line equivalent width (which is a measure of line to continuum ratio) has long been established, known as Baldwin effect [11].

The NLR is less dense ($n_e \sim 10^3\text{--}10^5 \text{ cm}^{-3}$ versus $n_e \sim 10^9 \text{ cm}^{-3}$) but much larger ($R \sim 10^2\text{--}10^4 \text{ pc}$ versus $R \lesssim 1 \text{ pc}$) than BLR. The size of the NLR is correlated with the narrow line luminosity [25], similar to the Strömgen sphere one can see in Galactic HII regions, where the ionization source is young stars.

Like the broad lines, narrow lines can also be used to identify AGNs. However, as the characteristic narrow emission lines are also observed in Galactic HII regions, in case of lacking broad line in spectrum, identification is more complicated. The emission line ratios are used to help to classify AGNs. Usually the NLR has higher metallicity than HII regions. $[\text{OIII}]/\text{H}\beta$ versus $[\text{NII}]/\text{H}\alpha$ diagram, i.e. “BPT diagram” (Baldwin, Phillips & Terlevich diagram) [12], is often used to make optical classifications.

1.1.5 Torus and AGN Unification Model

According to X-ray and optical narrow line classifications, many of the AGNs are lack of optical broad lines and characteristic featureless optical-UV continuum, showing distinct SEDs. This leads to a major division of the AGN family into two types of objects: type 1 AGNs and type 2 AGNs. Usually type 1 AGN refers to the systems with observed optical continuum or broad lines and type 2 AGNs do not. However, these two subclasses can be integrated into one simple model, as the unification model does [252].

The basic idea of the unification is: the central engine for all AGNs are the same and the observed variety of AGNs can be simply attributed to different viewing angles from the observer. The type 2 AGNs do have BLR and accretion disk as the type 1 AGNs do, but the optical-UV continuum and the broad lines are obscured by some materials. The absorber are anisotropically distributed and the whole structure, i.e. torus, is toroidal-like. The torus is expected to be dusty, so that the absorbed power could be efficiently re-emitted in the infrared (IR) band to lower the temperature and stabilize the torus structure. The IR continuum from the torus, in fact, is another important component of the AGN radiation.

One strong evidence for the validity of the unification model is that in some type 2 AGNs the broad emission lines are observed in polarized emission, probably due to photon-electron scattering at large radii [7, 171, 241]. Detailed imaging of narrow lines, e.g. $[\text{OIII}]$, show that the ionized gas is concentrated in a cone [79]. If the ionization source is the accretion disk continuum, then the existence of torus gives a natural explanation to this phenomenon. In high energy regime, the X-ray obscuration is also roughly consistent with

optical classification: type 2 AGNs usually have higher X-ray column density than type 1 AGNs [10]. All these are well compromised by a pure geometrical effect.

However, this over-simplified model fails to explain all the features observed in real complicated systems. There are still many open questions and the model itself needs to be further modified. One of the issues is that the model may strongly depend on AGN luminosity: the AGNs shown hidden BLR usually have higher accretion rates [103, 248]. The decreasing type 2 fraction with increasing AGN luminosity is another problem which can also be resolved by introducing the luminosity dependence into the unification model [226]. The “receding torus” model suggests that the covering factor is larger at lower luminosity [148]. This is probably determined by the microphysics of the dust grains: the temperature of innermost part of the torus must be at a fixed value because the chemical bond in these molecules will be destroyed at too high temperature.

Though it was originally suggested that the dusty torus is uniform toroid, recent studies have shown a clumpy structure may better describe the real physical condition of the torus [73]. That allows the leaking of central emission, i.e. the difference between type 1 and type 2 is not only due to different viewing angles but also depends on the probability of encountering obscuring clouds along the line of sight. This better explains the objects with contradictory classifications from optical and X-ray [194].

The AGN unification model also tries to unify the radio loud and radio quiet AGNs. However this is out of the scope of this thesis. More discussions can be found in the textbook by V. Beckmann and C. Shrader [22].

1.1.6 The AGN Family

There are many subclasses of AGNs due to historical traditions. Although the unification model is rather successful, many traditional names and acronyms are preserved and still commonly used. In order to reduce the difficulty to read this thesis, I summarize the major subclasses here.

The first optically discovered AGNs are so called quasi-stellar objects (QSOs, also known as quasars) because they appear as point sources in optical images, but their spectra show they are clearly different from normal stars. Historical quasars are type 1 AGNs because they are identified by the existence of the broad lines and the prominent optical-UV continuum. The study of quasars were independent of other types of AGNs until the unification model is developed. Now the quasars are usually referred to AGNs with absolute magnitudes brighter than $M_B < 23$ [214], i.e. the most luminous AGNs. The type 2 quasars without broad lines are discovered by using X-ray observations [4]. Quasars are usually radio loud, sometimes detected as γ -ray sources.

The Seyfert galaxies are originally classified by their optical emission lines, which are discovered by C. Seyfert early in 1940s [219]. Both type 1 and type 2 objects can be identified in this way. The Balmer lines in Seyfert 1 galaxies have both broad and narrow components, while only narrow component is observed in Seyfert 2. Sometimes the broad component is observed in only one of the Balmer lines. This kind of objects are probably intermediate types (Seyfert 1.2, 1.5, 1.8, 1.9) [189]. For Seyfert 2 galaxies, it is essential

to distinguish them from normal galaxies that are actively forming stars. As mentioned before, the HII regions are known to produce narrow emission lines, similar to the spectra of Seyfert 2 galaxies. The emission line ratios (BPT diagram) are used to classify AGNs and non-AGNs [12, 255, 129, 133]. It should be noted that quasars also show strong emission lines. The major difference between Seyfert galaxies and quasars is probably the luminosity. Seyfert galaxies are usually detected as less luminous AGNs so that the whole SED is not totally dominated by the AGN continuum (if not obscured) and the host galaxy contribution is clearly not negligible.

Comparing to luminous AGNs, the supermassive black holes are more likely to be in less active stage. It is estimated that the supermassive black holes spend only 1% of their time on the most active stage, like quasars [100]. Hence it can be expected that there are many low luminosity AGNs. The low-ionization nuclear emission-line regions (LINERs) are one population of such objects. They show faint core and strong emission lines from low ionized gas. Their emission line properties are similar to Seyfert 2 galaxies, though they can be roughly distinguished by calculating forbidden-to-Balmer line ratios (e.g. $[\text{OIII}]/\text{H}\beta$, $[\text{SII}]/\text{H}\beta$) [133]. The LINERs are expected to be at very low accretion rate, so the ADAF accretion model may better describe their properties.

One special class of objects selected from IR properties is ultra luminous infrared galaxies (ULIRGs), defined as far-IR luminosity higher than $10^{11} L_{\odot}$. Majority of the ULIRGs are found to host AGNs in their cores [228], though it does not necessarily mean all ULIRGs are AGNs [34]. The star formation rates in ULIRGs are found to be high. A great fraction of the IR flux is due to starburst contribution [95]. The ULIRGs are strongly connected with galaxy mergers. Under the assumption that the mergers will cause both star formation and AGN activity, they are suggested as a stage of the AGN evolution, before the quasar stage [211]. The ULIRGs are more likely to be observed at high redshift. In local Universe, the ULIRGs are very rare.

There are still be some other subclasses of AGNs not discussed above, such as radio galaxies and beamed AGNs mentioned in Section 1.1.3. As this thesis mainly focus on the X-ray, IR and optical properties of AGNs, they will not be further discussed in details.

1.2 AGN Host Galaxies

One major active research area in the AGN study is the relationship between AGNs and their host galaxies. The massive galaxies are known to host supermassive black holes in their centers. The observed close correlation between black hole mass and the galaxy bulge mass ($M-\sigma$ relation) is a strong indication of connection between AGN activity and the galaxy star formation [142, 85, 92, 244, 166, 104]. AGN is probably the stage that every massive galaxies have experienced. It is suggested that there is common mechanism to drive both the star formation and the black hole accretion. However, the underlying physics is still not clear yet. This section will briefly review the recent progress on this issue.

1.2.1 Normal Galaxies

Before discussing the AGN-host connection, it would be useful to briefly introduce the normal galaxies first.

It is well known that the normal galaxies can be classified into different types on the Hubble sequence according to their morphological properties [122]. The Hubble sequence tells us that there are mainly four classes of galaxies: elliptical, lenticular, spiral and irregular galaxies. The elliptical galaxies are characterized by their elliptical shape, dynamically supported by chaotic stellar velocity dispersion. The spiral galaxies are featured by their large stellar spiral arms. The spiral arms usually have small thickness, so that the whole structure is called “stellar disk”. Unlike the elliptical galaxies, the disk is supported by rotation around the axis. In the center of spiral galaxy there is usually a thicker stellar structure with similar shape to elliptical galaxy, so called “bulge”. The bulges are either velocity dispersion supported (classical bulge) or rotation supported (pseudo bulge). The elliptical galaxies can be viewed as “naked” classical bulges.

The elliptical galaxies are further split into eight subclasses labeled from E0 to E7, with increasing ellipticity. The spirals also have subclasses from Sa to Sd, with increasing disk to bulge ratio, though the spirals are usually further organized into two branches: with and without bars in their centers. Lenticular galaxies S0 are the transition type between elliptical galaxies and spiral galaxies. These types forms a E0-E7-S0-Sa-Sd sequence. Since there are two branches of spirals, the Hubble classification diagram are also called “Hubble fork”. The irregular, however, are out of the sequence. They are usually low mass systems or strongly disturbed systems.

Although the classification is morphological, there is physics behind. Galaxy optical colors show the composition of the stellar emission: bluer colors means younger stellar population. Elliptical galaxies are usually redder than their spiral counterparts. On average, the stellar age of elliptical galaxies are older than spiral galaxies. The elliptical galaxies are also called “early type” galaxies (because the stars form earlier) and spirals “late type” galaxies. It is suggested the galaxies will evolve from irregulars to spirals then to ellipticals. Other properties also appear to be correlated with the Hubble types. The most massive galaxies are usually elliptical galaxies while the spirals are more frequent in low stellar mass regime. The ellipticals are also usually found to have higher metallicity.

By numbers the galaxies are found in a bimodal distribution on the color-magnitude diagram: red sequence and blue cloud [24]. The red sequence galaxies are mainly old elliptical galaxies covering a large range of luminosities, while the blue cloud is a gather of young spiral galaxies with relatively lower luminosities. Between these two population, there is region so called “green valley” on the color-magnitude diagram. The green valley galaxies are often found to be blue spirals with red cores (probably due to old bulge or heavy extinction). The galaxies are supposed to evolve from blue cloud to red sequence by some mechanisms. The green valley may show the objects on the transition phase.

1.2.2 AGNs in Green Valley and Red Sequence

The host galaxies of local luminous AGNs are consistent with green valley galaxies: they have clear bulges but show recent star formation [129, 110, 113, 87]. This is also true for high redshift AGNs [177, 112, 264, 46]. The powerful AGNs are usually found in host galaxies with young stellar population [129, 110], and a major fraction of the total AGN emissivity in local Universe is contributed by AGNs with green colors [110].

On the other hand, the AGNs are found to reside in massive galaxies [129, 112]. The AGN fraction drops dramatically at stellar mass $M_* < 10^{10} M_\odot$ [129, 29]. And it is clear that many AGNs, especially the optical emission line and radio selected AGNs, are hosted by massive elliptical galaxies [29, 239, 254]. The most massive galaxies are usually passive elliptical galaxies lack of recent star formation as the red sequence galaxies have shown.

The studies of the correlation between the AGN accretion efficiency and the stellar mass or the black hole mass give a better view of the AGN host properties. It is found that the AGNs with the highest accretion efficiency (expressed in the black hole mass normalized luminosity, i.e. Eddington ratio L/L_{Edd}) are actually not the most massive black holes. The Eddington ratio decreases with increasing black hole mass [110, 88]. The total [OIII] luminosity in the local Universe contributed by AGNs is peaking at intermediate stellar mass: the most luminous AGNs are hosted by galaxies with $M_* \sim 10^{10.5} M_\odot$ [110]. The volume averaged black hole growth time for the low mass black holes ($M_{\text{BH}} \sim 10^7 M_\odot$) is comparable to the cosmic time, while the high mass ones are clearly less efficient [110].

To simplify the picture, it is proposed that there are two modes of AGN activities: the green valley mode and the red sequence mode. It is evident that the switching of the mode depends on the cold gas supply [126]. In case of red sequence galaxies, the central black holes can hardly obtain cold gas because the gas has been depleted during the last wave of star formation. The AGNs hosted by red sequence galaxies are suggested to be fed by the stellar wind of evolved stars [187, 48]. The hot gas ejected by the evolved stars is inefficient in feeding, so it is not possible to support high accretion rate. The supermassive black holes are probably constantly starving. On the other hand, the AGNs hosted by green valley galaxies are probably fed by cold gas, which can also support the observed star formation in host galaxies [127]. When the cold gas supply is sufficient, the black holes could accumulate masses at high accretion rates, probably limited only by the microphysics of the accretion systems themselves [126].

Recent studies suggest that the objects in the green valley actually have similar host star formation rates as the blue cloud galaxies. The peaking of AGN fraction in the green valley is likely caused by the bias against red sequence objects at low stellar mass end in luminosity-limited samples [225]. If the dust extinction is appropriated corrected, the AGN hosts are not dramatically peaking at intermediate colors but more consistent with the color distribution of normal galaxies [46, 206]. The observed “green valley” AGNs are at least partly contributed by intrinsically blue galaxies, with obscured strong ongoing star formation. The tendency of AGN hosts in green valley may still exist at low redshift [213, 143], but seems to disappear at higher redshifts [206].

For these green valley AGNs, like Seyfert galaxies, although the trend that more power-

ful AGNs show stronger host star formation is observed, the correlation shows large scatter [184, 260, 19]. The scatter decreases if the star formation rate is measured in smaller scale [260]. This implies that the AGN accretion is more closely connected with star formation in the center, while less relevant to the star formation in outer region, e.g. on the stellar disk. This could be easily understood if one assumes that the common driver of the black hole accretion and the star formation is cold gas feeding. Both processes will consume materials with relatively low temperature, which can be bounded by the gravity more easily. There are evidences that the observed cold molecular gas inflow rates are able to support the AGN activity [63, 176]. The host star formation can happen at scale of hundreds of parsecs to kiloparsecs, while the supermassive black hole can only trap the materials within a radius of a few parsecs. It takes long time ($\gtrsim 10^8$ yr) for gas to move from galactic star forming regions to AGN central engine, probably comparable to the duration of the whole AGN phase [168, 121]. The triggering of the AGN is only likely determined by the physical status of the innermost ~ 10 – 100 pc region. It is important to understand the physics of gas inflow in AGN host galaxies.

1.2.3 Gas Inflow

The M – σ relation implies the AGN is an important factor in the processes to form bulge. The location of AGN in the green valley naturally leads to the hypothesis that the AGNs are triggered during the processes responsible for the galaxy morphological transition, from blue cloud to red sequence. And the feeding of cold gas also requires some mechanisms to drive the gas inflow.

The currently favored mechanism is galaxy-galaxy merger. It has long been suggested that the AGN is triggered after the merger of two galaxies. Merging can cause gravitational torques and greatly accelerate the gas inflow. As long as one of the two galaxies has enough undisturbed cold gas, the star formation will be enhanced [180, 230, 262, 261, 65, 75, 149, 139]. In merging events, especially the major merger (the two merging galaxies have similar stellar masses), the regularly rotating disks can be destroyed and the mass will finally settle down onto bulges, forming elliptical galaxies as result. When merger induced gas inflow activates the star formation, it can also replenish the gas supply around the supermassive black hole in the galaxy center. So it is expected that the connection between nuclear activity and excessive star formation will be observed in merging systems. Numerical simulations have shown supporting results, though it is noticed that the major merger induced black hole accretion is not dominating the total black hole mass growth [117].

Observationally, the ULIRGs show clear evidence of merging events [49]. The large IR luminosities also suggest high star formation rates in their host galaxies. The ULIRGs are suggested as the stage right after the merging in the major merger driven AGN evolution scenario [211, 67, 120]. The black hole growth is heavily obscured in ULIRGs [242, 269], and the obscuring materials are expected to be expelled later by strong AGN or supernova feedback (see Section 1.2.4). The high accretion rate in quasars also favor the dramatic merger scenario [125, 231, 119]. It is expected that the quasars are on the stage right after the obscuring materials are removed.

This scenario well describes the mechanism to trigger the most luminous AGNs. However, these extreme objects are rare. For the majority of AGNs with intermediate luminosities, the importance of merger is still under investigation. One of the methods commonly used to identify merging systems is the morphological identification. Massive galaxies showing asymmetric and irregular signatures could be classified as merging systems. However, contradictory results are presented [96, 62, 140, 51, 32]. In general, most morphological studies show results against major merger scenario although the role of minor merger is still unclear. Alternatively, another way to identify merging galaxies is to search for galaxy pairs. Comparing to the morphological identification, the galaxy pairs method can detect earlier stage of the merging event at larger galaxy separations. Debates also exist [5, 150, 75, 74, 224, 153]. The origin of these discrepancies are unknown, probably due to different AGN samples and different merger definitions. The merger stages are still not well defined in observation and it is difficult to establish one-to-one relation from observations to numerical simulation results [201].

Besides the galaxy mergers, other mechanisms, external like mild interactions, internal like bars, spiral structures and gas instabilities, can also cause gas inflow. Unlike the dramatic merger events, they are relatively “slow” and may not change the galaxy morphology, so called “secular evolution” [141]. The importance of the secular evolution in AGN hosts is unclear yet, though examples have shown the possibilities to trigger AGNs [165, 144, 188, 74]. A subclass of Seyfert 1 galaxies, narrow line Seyfert 1 galaxies, featured by relatively narrower broad lines, are found to reside in pseudo bulges [188]. This excludes the major merger as a possible mechanism for these objects. It is probably that the bars are responsible for gas transportation in these objects [53]. It is also suggested that the secular evolution may be more efficient for gas rich galaxies at high redshift [172, 38, 94, 36].

1.2.4 Outflow and AGN feedback

The direct observation of gas inflow in AGN hosts is difficult, especially for high luminosity AGNs. This is because in these systems, the spectra are often dominated by strong outflow features [235, 63, 236]. The outflow could be expected because continuous accretion needs to remove the angular momentum from the inflow gas. The removed angular momentum must be carried by some other materials and they will gain additional angular velocity, and finally escape from the gravitational bounded system.

The outflows are in two forms: the jet and the wind. The jet is an important part of the AGN unification model (see also Section 1.1.3). There is clear observational evidence that the jet can inject energy into the surrounding medium on scale of kiloparsecs or more [82]. This energy injection can heat up the cold gas in the host galaxy or even in the dark matter halo, and prevent further gas accretion onto the galaxy nucleus [29, 200, 70]. This kind of “feedback” can suppress the host star formation rate and the black hole accretion rate.

Different from jets, which are more common in AGNs with low Eddington ratio, the winds are expected to be observed in high Eddington ratio objects, driven by the high radiation pressure. The winds are often observed on scale of several tens of parsecs, and

even smaller scales close to the accretion disk [235, 268, 63, 236]. They are probably common characteristics for quasars and moderately luminous Seyferts [253, 204, 33, 89, 202]. The winds are also expected to interact with interstellar medium and hence affect the growth of host galaxy.

It is natural to link the AGN feedback to the observed black hole-bulge connection [223, 80, 134]. The black hole accretion may be strongly regulated by the feedback. Instead of external reasons, e.g. lack of cold gas in the environment, the AGN feedback is an internal factor that stops endless feeding and naturally shuts down the ongoing star formation in the host galaxy. Some recent models have shown that the AGN feedback is probably playing an important role in host bulge formation [231, 67, 66, 135]. It is probably necessary to include the AGN feedback in any galaxy formation models.

1.3 Observational Facilities

This thesis is based on large variety of observational data. It is necessary to understand the capabilities as well as the limitations of the observational facilities used here. Below I briefly review the major telescopes/instruments used in this thesis.

1.3.1 *SDSS*

SDSS (Sloan Digital Sky Survey) [267] is one of the biggest astronomical surveys till today. It is started in year 2000 and has continuously observed for 13 years (*SDSS-I*, 2000-2005; *SDSS-II*, 2005-2008; *SDSS-III*, 2008-now). It is an optical survey using a 2.5-meter telescope located at Apache Point Observatory, including photometric and spectroscopic observations. The photometric images are with size of 2048×2048 pixels and each pixel corresponds to $0.396''$ on the sky. There are 5 optical filters u, g, r, i, z , with effective wavelengths of 3590 \AA , 4810 \AA , 6230 \AA , 7640 \AA and 9060 \AA , respectively [105]. With $1''$ seeing, airmass of 1.4 and exposure time of 55 seconds, the estimated $5\text{-}\sigma$ detection limits are 22.3, 23.3, 23.1, 22.3 and 20.8 in magnitude, respectively. The *SDSS* spectra are obtained with $3''$ diameter fibers, which are manually pointed to the targets. There are at most 640 fibers working simultaneously in one exposure, feeding the light to two spectrographs. The resulting spectra have typical resolution of ~ 2000 , covering wavelength range of $3900\text{--}9100 \text{ \AA}$. Different from traditional long slit spectra, the *SDSS* spectra only reflect the core of the objects if their angular sizes are larger than the fiber aperture. The *SDSS* consists of several individual sub-surveys, like the Sloan Legacy Survey, the Sloan Extension for Galactic Understanding and Exploration (SEGUE), Apache Point Observatory Galactic Evolution Experiment (APOGEE), Baryon Oscillation Spectroscopic Survey (BOSS), etc. This thesis mainly uses the data from the Legacy Survey in Data Release 7 (DR7), which covers more than 7500 square degrees at the North Galactic Cap and 740 square degrees in the South Galactic Cap.

1.3.2 *WISE*

The Wide-field Infrared Survey Explorer (*WISE*) [263] is a space-based IR telescope, launched on December 14, 2009. The 40 cm diameter telescope carries an all sky survey, with four channels, centered at $\sim 3.4 \mu\text{m}$ (W1), $\sim 4.6 \mu\text{m}$ (W2), $\sim 12 \mu\text{m}$ (W3) and $\sim 22 \mu\text{m}$ (W4), with a field of view of $47' \times 47'$. In single exposure, the spatial resolutions are $6.1''$, $6.4''$, $6.5''$ and $12.0''$, respectively. The scientific atlas is generated by over-projecting multiple exposures from various scans. The coadding procedures make the spatial resolution slightly worse but greatly suppress the noise level of the image. The spatial resolution is high enough to separate one galaxy to another, but the galaxies themselves at $z > 0.02$ are usually not well resolved. When building up the *WISE* all-sky catalog, source detection is performed on the atlas images while the flux measurement is done on the single exposure images. The *WISE* images are sufficiently deep to detect almost all the local galaxies with stellar mass higher than $10^{10} M_{\odot}$ at redshift $z < 0.06$. The sky coverage of *WISE* data is extremely high (close to 100%). The overall astrometry error is less than $0.5''$ for objects with signal-to-noise ratio larger than 20 so it is safe to directly match with optical catalogs, e.g. *SDSS* catalog. We use it, in combination of *SDSS* data, to gain good statistics for local AGN study.

1.3.3 *Swift* BAT

The *Swift* Gamma-ray burst observatory [93] is a space-based telescope mainly designed for alert of gamma-ray bursts and observing their afterglows in X-ray, UV and optical bands with autonomous rapid slewing satellite, launched on November 20, 2004. There on board are three science instruments: Burst Alert Telescope (BAT) [16] X-ray Telescope and UltraViolet/Optical Telescope. This thesis only the data from BAT are used. BAT, boarding a CdZnTe detector, is capable to observe hard X-ray/gamma-ray in photon energy range of 15–150 keV, with a field of view of 1.4 steradian (partly coded) and spatial resolution of $17'$. The energy resolution at 60 keV is around 3.3 keV ($E/\Delta E \approx 20$). The sensitivity of the detector is $\sim 10^{-8} \text{ erg cm}^{-2} \text{ s}^{-1}$ (15–150 keV). Though the main scientific aim of BAT is tracking transient gamma-ray bursts, it also scans the whole sky region, detecting a large number of permanent high energy sources, like AGNs. Due to relatively large PSF size and shallow depth of BAT images, it is only possible to use BAT catalog to study low redshift AGNs. However, the high photon energy of BAT band means the flux is much less affected by neutral gas absorption, comparing to soft X-ray bands. This leads to a complete AGN sample against obscuration bias.

1.3.4 *IRAS*

The *IRAS* [185] is an IR space telescope cryogenically cooled with liquid helium, launched on January 26, 1983. The on-board survey array is capable to take scan images in four different bands, 8.5–15 μm (centered at $\sim 12 \mu\text{m}$), 19–30 μm (centered at $\sim 25 \mu\text{m}$), 40–80 μm (centered at $\sim 60 \mu\text{m}$) and 83–120 μm (centered at $\sim 100 \mu\text{m}$). As one of the earliest

IR telescopes, the beam size is $\sim 30'$, much worse than typical optical observations. This hampers the usage of *IRAS* data for high redshift studies. In this thesis, *IRAS* data are used to study nearby AGNs at redshift lower than 0.3.

1.3.5 *Chandra* ACIS

The *Chandra X-ray Observatory* [259] is an X-ray space telescope operated by the National Aeronautics and Space Administration (NASA), launched on July 23, 1999. It supports X-ray observation in photon energy range of 0.08-10 keV. On board there are two main science instruments: the High Resolution Camera and the Advanced CCD Imaging Spectrometer (ACIS) [90], and two ancillary transmission grating instruments for high quality spectra. In this thesis, we use the X-ray survey data obtained with ACIS. ACIS is capable for taking images at high spatial resolution ($\sim 0.5''$) with a field of view of $16.9' \times 16.9'$ and with 4–6 pieces of 1024×1024 CCDs, meanwhile producing spectra with moderate energy resolution ($E/\Delta E \approx 10\text{--}40$). The hard X-ray band (2-10 keV) is less affected by absorption along the line of sight. These characters allow us to build up a relatively unbiased AGN sample at high redshift.

1.3.6 *Herschel* PACS

Herschel [197] is a space telescope launched on May 14, 2009, administrated by European Space Agency (ESA), with capabilities of observing far-IR and sub-millimeter emissions at 55–671 μm . There are three major observational instruments on board: the Photodetector Array Camera and Spectrometer (PACS) [198], the Spectral and Photometric Imaging REceiver (SPIRE) [101] and the Heterodyne Instrument for the Far Infrared (HIFI) [64]. In this thesis, we only use the photometric images from PACS. In photometry mode, PACS is capable to observe simultaneously the same sky region in two bands, 60–85 μm (blue, centered at $\sim 70 \mu\text{m}$) or 85–125 μm (green, centered at $\sim 100 \mu\text{m}$) and 125–210 μm (red, centered at $\sim 160 \mu\text{m}$), with a field of view of $\sim 1.75' \times 3.5'$, and pixel size of $3.2'' \times 3.2''$ (blue/green) and $6.4'' \times 6.4''$ (red). The images are usually obtained by scanning the sky region. At scan speed of $10''$ per second, the beam sizes (FWHM) of blue, green and red bands are $\sim 5.5''$, $\sim 6.7''$ and $\sim 12''$, respectively. At higher scan speed, the spatial resolution is slightly worse. With such high spatial resolution, as well as much higher sensitivity than any other IR facility in this wavelength range, the PACS data are used for high redshift AGN studies (see Section 4.2).

This thesis aims to study the relation between the AGN activity and the host galaxy formation. The results will be presented in three chapters, each relatively independent but also closely related. Chapter 2 will focus on the host galaxies of low and moderate luminosity AGNs at low redshift, i.e. Seyfert galaxies and LINERs, studying their host properties using the IR luminosities from dusty torus. Chapter 3 will discuss the relation between AGN activity and the galaxy-galaxy interactions for these low redshift AGNs, revealing the possible mechanism driving the observed black hole–bulge connection today. Chapter 4 will then extend the study to higher redshifts and give a grand overview of the AGN–host connection in the Universe, current and past. Finally in Chapter 5, I will briefly summarize the results and point out some unresolved problems for future research.

Chapter 2

AGN Torus Emission and Host Properties

2.1 Introduction

In order to study the AGN host properties, it is important to extract the host galaxy emission from the observational data. But this is difficult in case of the most luminous AGNs, like type 1 quasars. The high nuclei-to-host contrast prevents accurate estimation of the host component, especially in UV and optical bands. Instead, thanks to the reduced contrast due to obscuration of the nuclear emission, we can observe type 2 AGNs to acquire better measurements of host properties, like stellar mass. However, in this case, it is a question that how to estimate the black hole accretion rate. There are several methods to indirectly estimate the AGN activity level. High energy (hard X-ray, γ -ray) radiation is hardly affected by absorption due to small effective cross section with neutral gas. Hard X-ray photon can penetrate the neutral gas barrier even with column density as high as 10^{24} cm^{-2} , so that it is widely used in recent AGNs studies. Photons with lower energy, like optical/UV photons, are usually not able to survive the torus absorption, so only geometrically unobscured emission could be used. Fortunately, as the obscuring material seems not isotropically distributed, some interstellar medium far away from the nuclei can be excited by the unobscured AGN radiation and re-emits in form of optical emission lines, such as narrow [OIII] λ 5007 line [110]. On larger scale, radio emission from jet is used to indicate the AGN activity by assuming the jet power is proportional to accretion rate. And finally, the IR continuum emission from the torus can also be used to indicate the black hole accretion rate [115, 146]. It directly measures the absorbed optical/UV radiation.

Previous studies based on large sample of optically selected AGNs, using [OIII] luminosity as AGN activity indicator, have established a close AGN-bulge formation relation [110, 126, 181]. T. Heckman et al. [110] find that for AGNs with $L[\text{OIII}] > 10^{6.5} L_{\odot}$, i.e. AGNs with luminosity above $10^{43.5} \text{ erg s}^{-1}$ if given their assumed bolometric correction of $L_{\text{bol}}/L[\text{OIII}] \approx 3500$ [270, 167, 110], the growth time of the host bulge is closely tracing that of the black hole. The ratio between the star formation rate and the accretion rate is close

to the observed bulge mass to black hole mass ratio.

However, it seems that different AGN indicators are not fully consistent with each other, which may cause the results somehow biased. Deep X-ray surveys are considered to be capable to build up AGN samples close to complete [3]. But there are evidences that they miss extremely obscured AGNs with column density larger than 10^{25} cm^{-2} , or so called Compton-thick AGNs [111, 193, 97, 170, 243, 99]. Optically, the $[\text{OIII}]/L_X$ ratio decreases with increasing X-ray luminosity [183, 247], implying that narrow line regions are sometimes still affected by the obscuration or some other complicated physical processes. Accretion around low mass black holes are probably missing from the optical surveys [98]. The radio jet, though clearly free from the dust obscuration, is somehow worrisome indicator in case of lower-luminosity FR-I type radio AGNs, probably due to different accretion modes and jet mechanisms [29]. And finally, the IR selected AGN samples are reported biased against weak and type 2 AGNs, and heavily contaminated by strongly star forming galaxies [45, 42].

These discrepancies imply that any AGN sample based on single AGN indicator may be biased in some fashion. Hence it is necessary to cross check the results using different AGN indicators, i.e. a multi-wavelength study is very important. Some previous works have exposed systematical differences between AGNs selected in different ways. A recent study using data from the AGN and Galaxy Evolution Survey (AGES) shows that the host properties of radio-selected AGNs are clearly different from that of the X-ray or IR-selected AGNs while the latter two populations are generally consistent with each other [112]. They attribute the discrepancies to different evolution stages of AGN, which may affect the observed AGN-host connection in different wavelength ranges. In this chapter, we will follow a similar approach of the work by T. Heckman et al. [110] to investigate the host properties of AGNs. We use nuclear mid-IR luminosity, which originates from the very central part of the galaxy with a size of several parsecs [124, 245, 21, 44, 246, 138, 136, 137, 114], instead of $[\text{OIII}]$ luminosity, which is from hundred of parsecs away from the central region, as AGN activity indicator. We compare the results using these two AGN indicators.

2.2 Data

2.2.1 *SDSS* Spectroscopic Catalog and *WISE* Counterparts

We perform our analysis based on a large sample of local type 2 AGNs, extracted from *SDSS* (see also Section 1.3.1) spectroscopic catalog. The parent sample includes all galaxies with r band magnitudes $r < 17.6$ from the MPA/JHU *SDSS* DR7 catalog¹. We drop all the galaxies with $r > 14.5$, to remove the nearby galaxies with very large angular sizes, because the *SDSS* pipeline photometry will fail for highly extended sources. We limit our sample to redshift range of $0.02 < z < 0.21$. The stellar mass is obtained by SED fitting using the methods suggested by S. Salim et al. [210]. The uncertainty of the stellar

¹<http://www.mpa-garching.mpg.de/SDSS/>

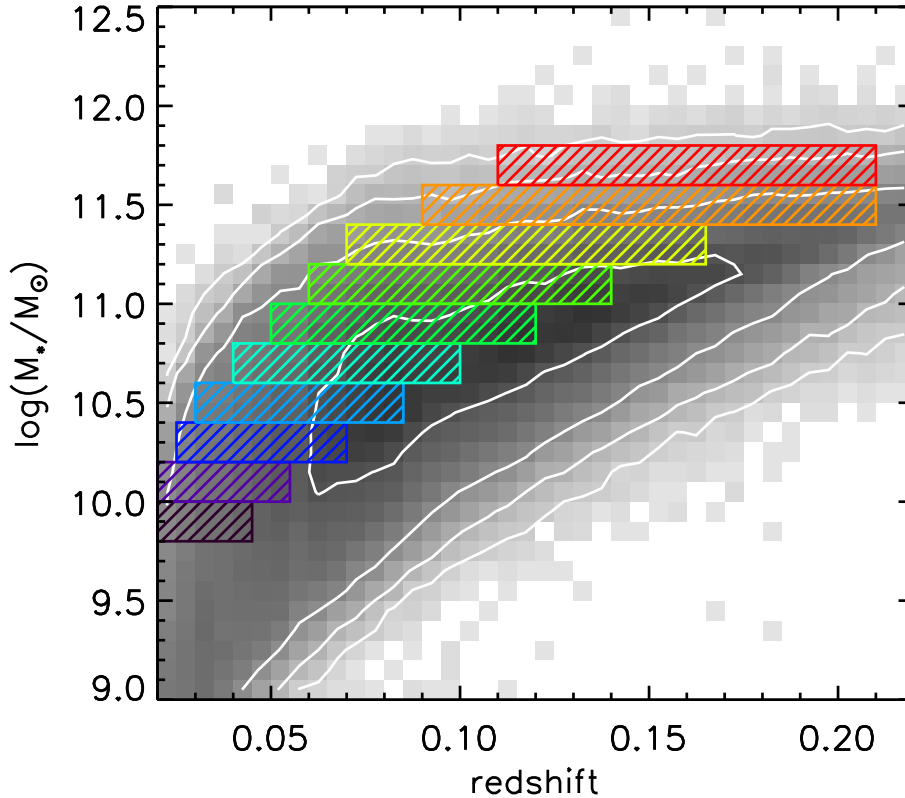


Figure 2.1: The redshift versus stellar mass. The grey-coded background and the white contours show the distribution of the whole SDSS spectroscopic sample with a $14.5 < r < 17.6$ cut on the r -band model magnitude. The colored boxes show different stellar mass bins and redshift ranges for the volume-limited subsamples.

mass estimation is ~ 0.15 dex. We only focus on massive galaxies with stellar masses of $10^{9.8} M_{\odot} < M_{*} < 10^{11.8} M_{\odot}$, because the majority of local AGNs are hosted by massive galaxies [129].

We first define a stellar mass “complete” sample of galaxies. We divide the galaxies into stellar mass bins of width 0.2 dex in $\log(M_{*})$. In each stellar mass bin, we evaluate the redshift interval over which all such galaxies are detected in the *SDSS* spectroscopic sample (see Figure 2.1). The upper redshift limits show where we are not able to detect all the galaxies within given stellar mass range by putting the $r < 17.6$ flux limit. The cuts are similar to the sample definition adopted by A. von der Linden et al. [256] in their Figure 5. The lower redshift limits are corresponding to the $r > 14.5$ flux limit which removes nearby galaxies with too large angular size to make reliable *SDSS* photometry. In total there are 216272 galaxies in these volume-limited subsamples. The details of the samples are listed in Table 2.1.

These *SDSS* galaxies are matched to the *WISE* catalog within a search radius of $3''$ from the optical position. Given the high astrometry precision of both *SDSS* and *WISE*, the probability of mismatching is negligible. We ensure reliable *WISE* detections by adopting

M_*/M_\odot	Redshift	Number
$10^{9.8} - 10^{10.0}$	0.020 – 0.045	5673
$10^{10.0} - 10^{10.2}$	0.020 – 0.055	9661
$10^{10.2} - 10^{10.4}$	0.025 – 0.070	18066
$10^{10.4} - 10^{10.6}$	0.030 – 0.085	30201
$10^{10.6} - 10^{10.8}$	0.040 – 0.100	36404
$10^{10.8} - 10^{11.0}$	0.050 – 0.120	41500
$10^{11.0} - 10^{11.2}$	0.060 – 0.140	36133
$10^{11.2} - 10^{11.4}$	0.070 – 0.165	23083
$10^{11.4} - 10^{11.6}$	0.090 – 0.210	13212
$10^{11.6} - 10^{11.8}$	0.110 – 0.210	2338

Table 2.1: The stellar mass bins for the sub-samples that make up the volume-limited sample. The corresponding redshift ranges and the number of sources in each bin are also listed.

a SNR cut of 3 in each of the bands. A large number of objects are extended sources in *WISE* bands. In this case, we use the total magnitudes derived from elliptical aperture photometry instead of the default *WISE* pipeline profile-fitting photometry, which will underestimate the total flux. The parameters of the elliptical apertures, such as axis ratios and position angles, are not derived from the *WISE* images themselves, but taken from the *2MASS* Extended Source Catalog [227]. In general, the elliptical magnitudes better capture the total flux. But it is reported that for well-resolved galaxies the total flux is still underestimated by about 30% [59]. However, we note that our results are barely affected by the choice of photometry apertures, probably because we simply focus on the nuclear emission that is irrespective to the very outer part of the galaxy.

The original *WISE* Vega magnitudes are converted into AB magnitudes. In order to get monochromatic fluxes, we apply color corrections to the observed broad band fluxes based on the spectral shape [263]. For simplicity, only the table entries for power law forms $F \propto \nu^\alpha$ are used, and the correction factors are obtained by interpolating between the *WISE* colors, which are typically less than 3% for 3.4 (W1), 4.6 (W2) and 22 μm (W4) bands (12 μm i.e. W3, is very broad so the corrections can be as large as 10%).

In the whole sample, 213789 (98.9%) sources are simultaneously detected by *WISE* in W1 and W2 bands at the 3σ level. However, only 54324 (25.1%) sources have $> 3\sigma$ detections in all *WISE* bands. W4 has the lowest detection rate. We thus construct a subsample by adopting a 22 μm flux cut of 7 mJy. This flux level is where the *WISE* images with average coverage depth will recover $\sim 95\%$ of “real” sources [59]. There are 21942 sources in this subsample (hereafter we call the whole volume-limited sample as S1 and this subsample as S2), and 21254 (96.9%) of them are detected in all *WISE* bands. We will use S2 in case of comparing all the *WISE* bands. In Table 2.2 we summarize the *WISE* detection rates of our various samples.

We weight each galaxy by the inverse of V_{max} , which is defined as the total volume within which this galaxy can be observed and make it into our sample. S1 is a sample

Detection	S1	S2
Any band	213789 (98.85%)	21942 (100.00%)
W1+W2	209142 (96.70%)	21330 (97.21%)
W4	56697 (26.22%)	21942 (100.00%)
All bands	54324 (25.12%)	21254 (96.86%)

Table 2.2: The detection rates in *WISE* bands. S1 and S2 are samples we use (see Section 2.2). “W1+W2” means detection in both 3.4 and 4.6 μm bands. “W4” means detection in 22 μm band.

selected by stellar mass, while S2 is a 22 μm flux limited sample, it is natural that S1 and S2 have different weightings. Figure 2.2 shows the volume-weighted number distributions over some galaxy properties for S1 (black curve) and S2 (red curve) galaxies. Comparing with S1, S2 galaxies have lower stellar masses, bluer $g - i$ colors and lower concentrations. The differences arise because passive galaxies are generally not detected at 22 μm , that we will discuss later. The shape of the stellar mass distribution of S1 galaxies is consistent with stellar mass function measurement using *SDSS* and *2MASS* [23].

2.2.2 Optical Classification

In order to classify the galaxies as star forming galaxies or AGN, we use the classical [NII]/ $\text{H}\alpha$ versus [OIII]/ $\text{H}\beta$ diagnostics (BPT diagram) [12, 255, 129, 133]. The fluxes of the key emission lines ($\text{H}\alpha$, $\text{H}\beta$, [OIII] λ 5007, [NII] λ 6584 and [SII] λ \lambda6717,31) are directly taken from the MPA/JHU catalog. The errors on the emission lines measurements from the original catalog are scaled up by a factor of 2.473, 1.882, 1.566, 2.039 and 1.621 for the five lines respectively, following the recommendations on the webpage of MPA/JHU catalog². We only consider the emission lines that are clearly detected with $\text{SNR} \geq 3$. In S1, there are 27755 objects above the line suggested by G. Kauffmann et al. (K03 line) [129], which is used to separate the galaxies with [OIII] line luminosity dominated by AGN activity. We call them “optical AGNs” hereafter.

We use the [OIII] line luminosity as an optical indicator of black hole accretion rate as previous works did [110]. We use the Balmer decrement to correct the dust extinction, using the reddening curve optimized for emission lines which is suggested by V. Wild et al. [260], and assuming an intrinsic $\text{H}\alpha/\text{H}\beta$ ratio of 2.87 for star forming galaxies and 3.1 for AGN [190]. 67.6% (18751) of the optical AGNs fall in the region between the K03 line and the maximum starburst line suggested by L. Kewley et al. [132]. A non-negligible fraction (between 10% and 50%) of their [OIII] luminosities can be contributed by star formation in the host galaxy [126]. In order to estimate the [OIII] luminosity from the narrow-line region, we use the simple method suggested by G. Kauffmann & T. Heckman [126] to separate the total [OIII] luminosity into AGN and star formation components. The fraction of AGN contribution is calculated based on the galaxy’s position on the BPT

²http://www.mpa-garching.mpg.de/SDSS/DR7/raw_data.html

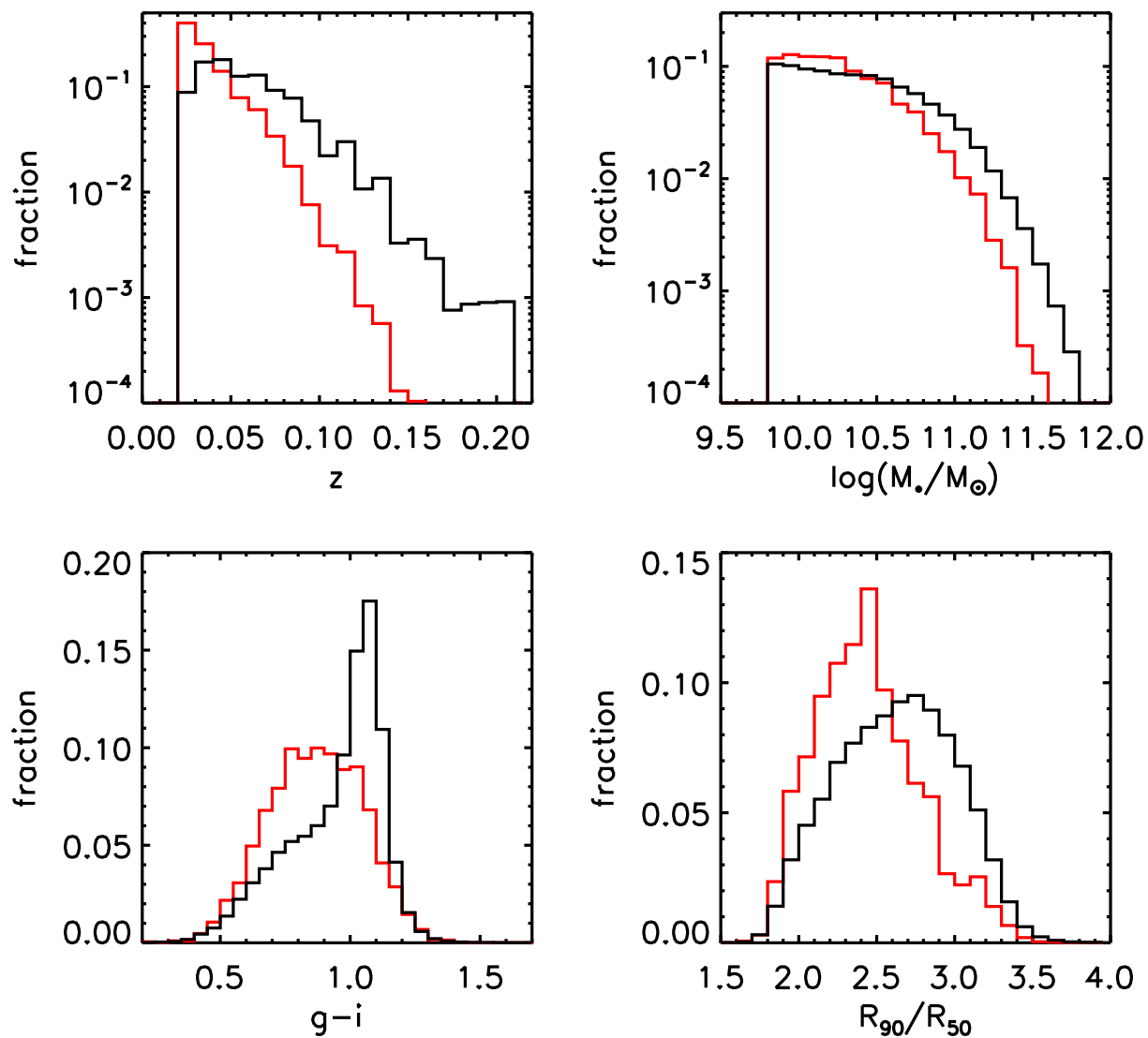


Figure 2.2: The normalized number distributions of redshift, stellar mass, K-corrected $g-i$ color and r -band concentration index (defined as the ratio of the radii enclosing 90% and 50% of the total r -band light). The black and red lines are for samples S1 and S2, respectively.

Opt-class	S1	S2
All	216272 (100.00%)	21942 (100.00%)
AGN	27755 (12.83%)	8133 (37.07%)
Strong AGN	7613 (3.52%)	4105 (18.71%)
Seyfert	9776 (4.52%)	4171 (19.01%)
LINER	16377 (7.57%)	3873 (17.65%)
SF	23604 (10.91%)	11077 (50.48%)
Passive	49401 (22.84%)	9 (0.04%)
Non-AGN	73005 (33.76%)	11086 (50.52%)
Ambiguous	115512 (53.41%)	2723 (12.41%)

Table 2.3: Sample S1 and S2. The numbers and the fractions of each type of galaxies are listed.

diagram (see their Figure 3).

“Strong” AGNs are defined as optically-identified AGNs with [OIII] luminosities larger than $10^7 L_{\odot}$. G. Kauffmann et al. [129] show that false BPT classification because of dilution by emission from HII regions in the surrounding host galaxy falling within the SDSS fiber aperture is not important for AGNs with [OIII] luminosities greater than this value. Similar test is carried out to what they did by calculating the fraction of strong AGNs in narrow bins of stellar mass and redshift, and our results are similar to theirs.

We also classify the AGNs into Seyfert galaxies and LINERs (low ionization nuclear emission-line regions), according to the [SII]/H α ratio using Function 7 in the paper by L. Kewley et al. [133]:

$$0.72/[\log([\text{SII}]/\text{H}\alpha)] + 1.30 < \log([\text{OIII}]/\text{H}\beta). \quad (2.1)$$

A small fraction of AGNs are classified neither as Seyferts nor as LINERs, simply due to low signal-to-noise ratio of the [SII] lines.

We select a sample of AGN-free galaxies (“non-AGN”) which are either star forming galaxies (“SF”) or galaxies without detected emission lines (SNR less than 2, “passive”). In order to minimize mis-classifications due to observational bias, the passive galaxies are also required to have large concentration index $R_{90}/R_{50} > 2.6$, high stellar mass surface density $\mu_* > 10^{8.5} M_{\odot}/\text{kpc}^2$ and large 4000 Å break strength $D_n(4000) > 1.6$. These values correspond to the sharp transitions from young star-forming galaxies to old passive galaxies [131].

In table 2.3 we summarize the optical classification of our local galaxy samples. Because of the 22 μm flux cut, the fraction of passive galaxies in sample S2 is much smaller than that in sample S1. We note because we use relatively strict cuts, a large fraction of objects (115512, 53.4% of S1, “ambiguous”) are not classified into any of the subclasses described above. We do not use them in our further analysis.

2.2.3 SDSS quasars

In our S1 and S2 samples, only narrow-line AGNs are included. We have extracted a sample of low redshift ($z < 0.7$) type 1 AGN from the SDSS DR7 quasar catalogue [222, 215]. The upper redshift limit is chosen to ensure that the [OIII] line still falls in the SDSS spectrum. We match this sample to the *WISE* catalogue within a 3" matching radius. Our type 1 sample includes 3165 quasars, of which 3086 (97.5%) are detected in all *WISE* bands. Since the quasars are usually core-dominated, we use *WISE* magnitudes based on PSF-fit photometry. The [OIII] line is corrected for extinction using the Balmer decrement measured from the narrow components of the $H\alpha$ and $H\beta$ lines. We only use the emission lines with signal-to-noise ratio larger than 3. There are totally 3011 quasars with reliable [OIII] fluxes and detected in all *WISE* bands, but only 592 of them have reliable Balmer decrement measurements, mostly because $H\alpha$ line is in SDSS spectrum range only at $z \lesssim 0.4$. For the other 2419 quasars, we apply the extinction correction assuming a typical Balmer decrement ($H\alpha/H\beta \approx 4.31$), which is estimated by taking the median value of the 592 quasars. The K-correction to the *WISE* luminosities are done by using the QSO1 template from the galaxy SED library by M. Polletta et al. [199]. The K-correction is small, less than 0.05 dex for W2 luminosity and less than 0.01 dex for W4 luminosity, because the typical quasar SED is flat in this wavelength range. Different libraries [8] may give slightly different K-correction values. But this uncertainty is negligible, comparing with the observed scatter, as we will show later.

Throughout this thesis, the concordance 0.7-0.3-0.7 cosmology [240] is adopted.

2.3 Mid-IR colors of local galaxies

2.3.1 Stellar emission

The *WISE* 3.4 μm and 4.6 μm bands are in a wavelength range that the emission in galaxy is dominated by stars with intermediate and old age [169, 78, 123].

The $L-M_*$ relations of the S2 inactive galaxies are shown in Figure 2.3. The four panels show 3.4 μm , 4.6 μm , 12 μm and 22 μm luminosities respectively. In order to check the sensitivity of *WISE* luminosities to star formation, we split the sample into 3 different bins of 4000 \AA break strength, $D_n(4000)$, which can be regarded as an indicator of the specific star formation rate (SSFR). Comparing to emission lines, such as $H\alpha$, the commonly used star formation rate indicator for star formation in past ~ 100 Myr, $D_n(4000)$ is only measuring an integrated star formation activity over a timescale of $\sim \text{Gyr}$, but is scarcely affected by dust extinction and the ‘‘contamination’’ from AGN power. It allows a direct comparison of the stellar populations of AGN hosts and inactive galaxies in an unbiased way [130]. As can be seen from Figure 2.3, all the *WISE* luminosities have clear correlation with stellar mass, despite that the star formation is making a substantial contribution. With increasing wavelength, the offset between young and old galaxies becomes bigger. In the two short wavelength bands, W1 and W2, the small offset implies that the 3–5 μm wavelength range is indeed dominated by the emission from old stellar population. the

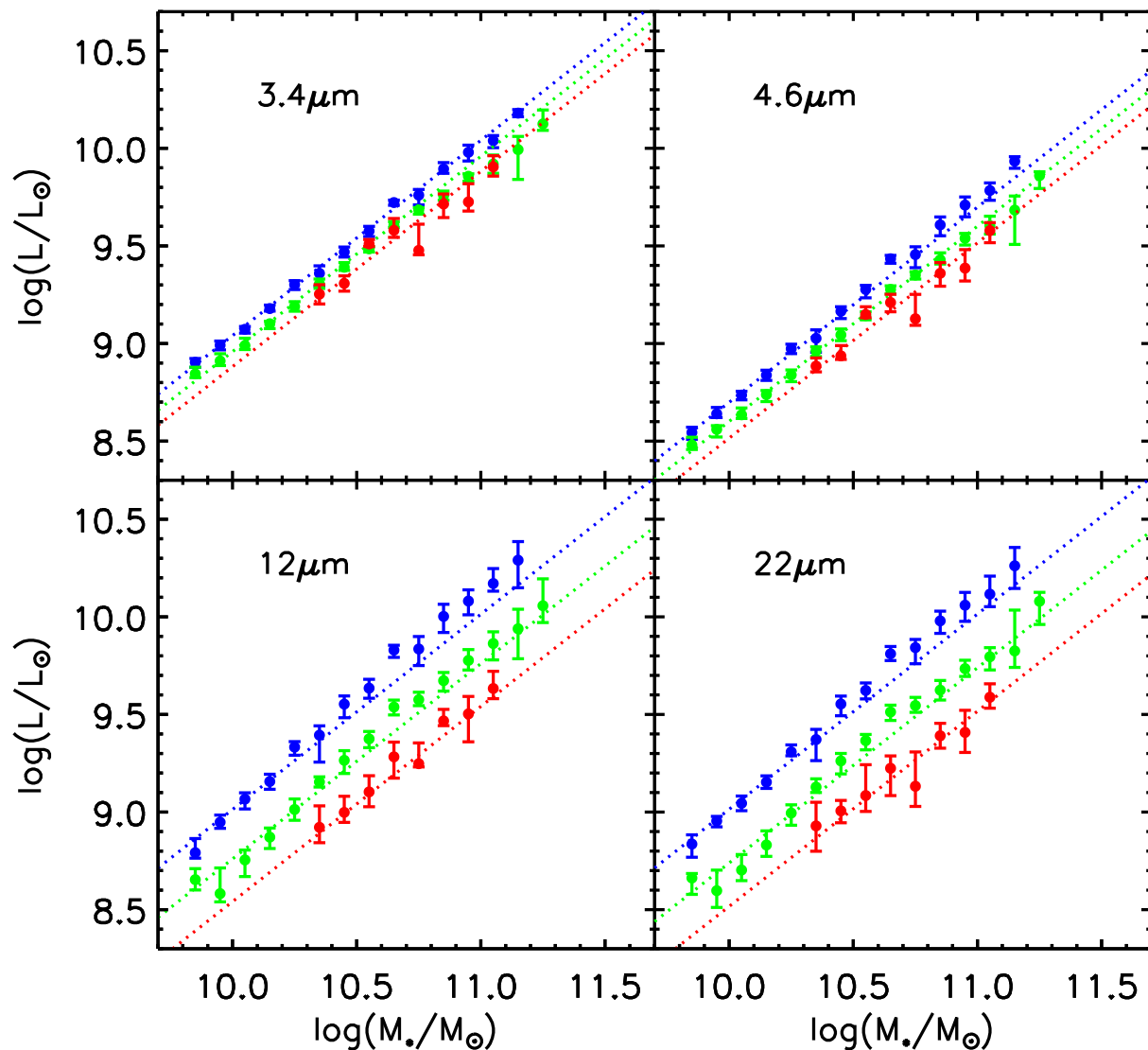


Figure 2.3: The *WISE* monochromatic luminosity as a function of stellar mass for S2 non-AGN galaxies. The blue, green and red points are for three different 4000 \AA break strength bins: $1.0 < D_n(4000) < 1.3$, $1.3 < D_n(4000) < 1.5$, $1.5 < D_n(4000) < 1.8$. Any data bin with source number lower than 20 is dropped. The error bar shows the error on the median value at a confidence level of 95%, estimated by bootstrapping within each data bin. The dotted lines are the best linear fits to the data, assuming a slope of 1.

lower mass-to-light ratios in younger galaxies are probably due to additional contribution from thermally pulsing asymptotic giant branch (TP-AGB) stars. In W3 and W4, the offset between galaxies of the same stellar mass with different 4000 Å break strengths becomes very large. In these bands the dust emission replaces the star light to become the dominant contributor to the total flux.

In Figure 2.4, we show the distribution of S1 non-AGN galaxies on the $[3.4] - [4.6]$ color versus stellar age (indicated by 4000 Å break) plane. In this study, we mainly focus on 3.4 μm and 4.6 μm bands. We use the S1 sample to prevent bias against galaxies not actively forming stars, because we are aiming to investigate the emission from stars in this section. Instead of performing K-correction to the colors, we split the sample into 5 narrow redshift bins, within which the K-correction could be ignored. The non-AGN objects clearly show a bimodal distribution on the color-age plane, reflecting the star forming blue cloud and the passive red sequence of nearby galaxies. On average, the young star forming galaxies are redder than old galaxies.

We overplot stellar population synthesis models built by Bruzual & Charlot [43] (BC03, and an updated version CB07) on our observed galaxy distribution. The two sets of models mainly differ in the treatment of the TP-AGB stars. In CB07 (squares), the dusty TP-AGB emission contribution is higher than that in BC03 (circles). CB07 curve predicts much redder IR colors at intermediate ages. In this plot, we show the predicted color of a “simple stellar population” (SSP) at a range of different ages, and for two different metallicities (solar, $Z = 0.02$, and sub-solar, $Z = 0.008$, metallicities). At ages between ~ 200 Myr and ~ 2 Gyr, the CB07 SSPs are clearly redder than the BC03, forming a red “bump” on the low metallicity CB07 curve. At low 4000 Å break, the $[3.4] - [4.6]$ colors of the galaxies with the lowest 4000 Å break strengths are well matched to the low metallicity case of CB07 instead of BC03. This implies the color difference between young and old galaxies is caused by essential TP-AGB contribution.

None of the model curves indicate $[3.4] - [4.6] \gtrsim 0.7$. Also from our data it seems there are very few normal galaxies with such red colors. In the next section, we will study the mid-IR colors of AGN host galaxies and show that the colors may help to identify AGNs.

2.3.2 AGN host galaxies

We show the distribution of S2 galaxies on the $[3.4] - [4.6]$ versus $[12] - [22]$ *WISE* color-color plane. There is a clear peak at $[3.4] - [4.6] \approx 0$ and $[12] - [22] \approx 2$. We also indicate the locations of different galaxy subclasses, as well as *SDSS* quasars. Weak AGNs have very similar color distribution as star forming galaxies do. The distribution of strong AGNs are shifted towards slightly redder $[3.4] - [4.6]$ and $[12] - [22]$ although the overlap is still substantial. Only the *SDSS* quasars have clearly disjoint *WISE* colors from those of normal galaxies. The quasar colors reflect a “pure” AGN SED profile, as the host galaxy contamination is small in these objects. Thus we conclude that $[3.4] - [4.6]$ colors of most nearby type 2 AGNs are strongly affected by the host stellar emission. Only a small fraction of strong type 2 AGNs show red $[3.4] - [4.6]$ and $[12] - [22]$ colors similar to those of quasars.

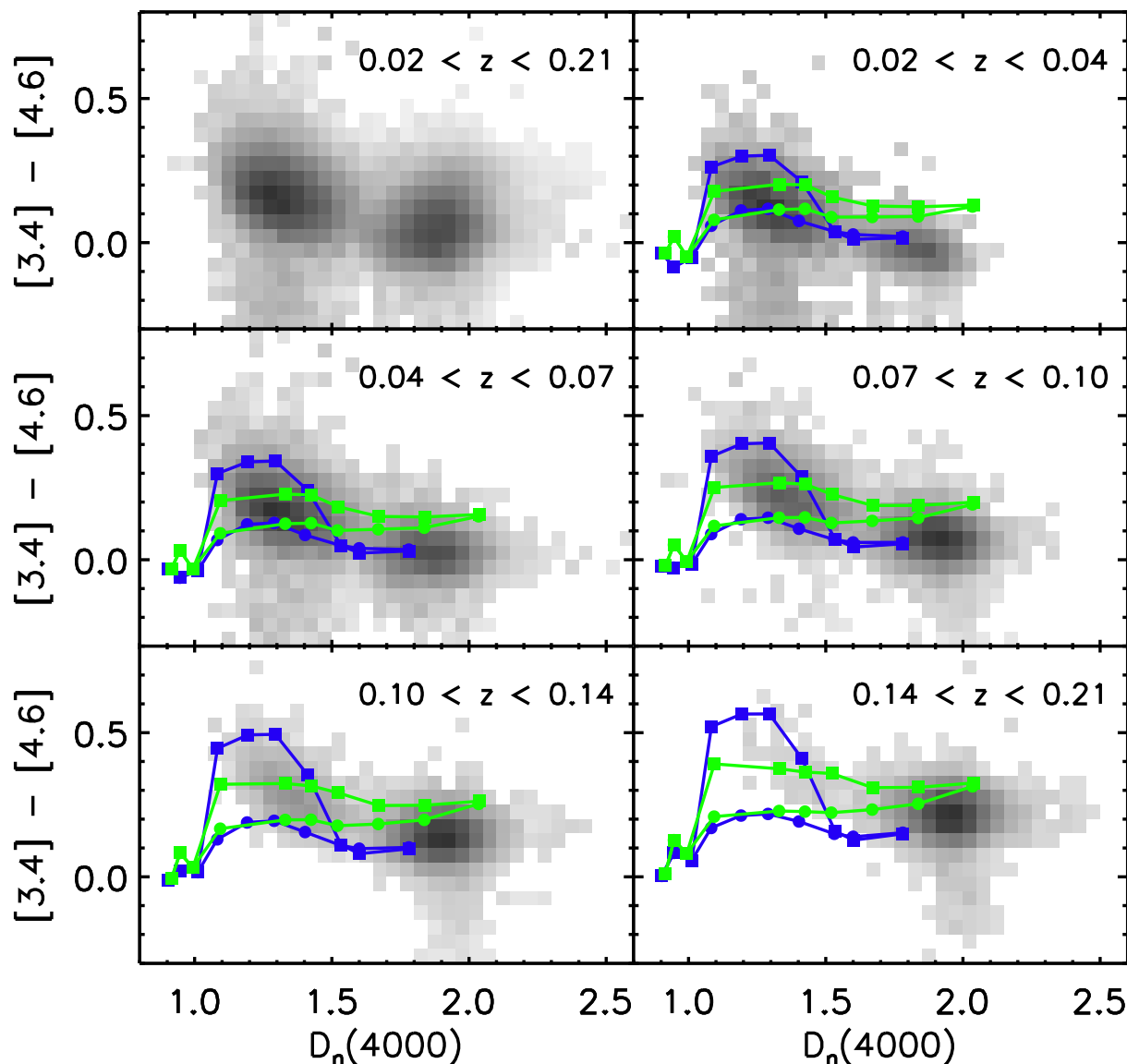


Figure 2.4: The $[3.4] - [4.6]$ color versus 4000 \AA break plane. The distribution of S1 non-AGN galaxies is displayed as background grey scaled histogram. Stellar population models are overplotted as blue (sub-solar metallicities, $Z = 0.008$) and green (solar metallicities, $Z = 0.02$) curves. The circles are BC03 data points and squares are CB07. The data points on the curve are from the templates with stellar age of 0.005, 0.025, 0.1, 0.29, 0.64, 0.9, 1.4, 2.5, 5 and 11 Gyr, respectively. The model curves for each redshift bin are from the models convolved with *WISE* band filters at redshifts of 0.03, 0.05, 0.08, 0.12 and 0.17, respectively.

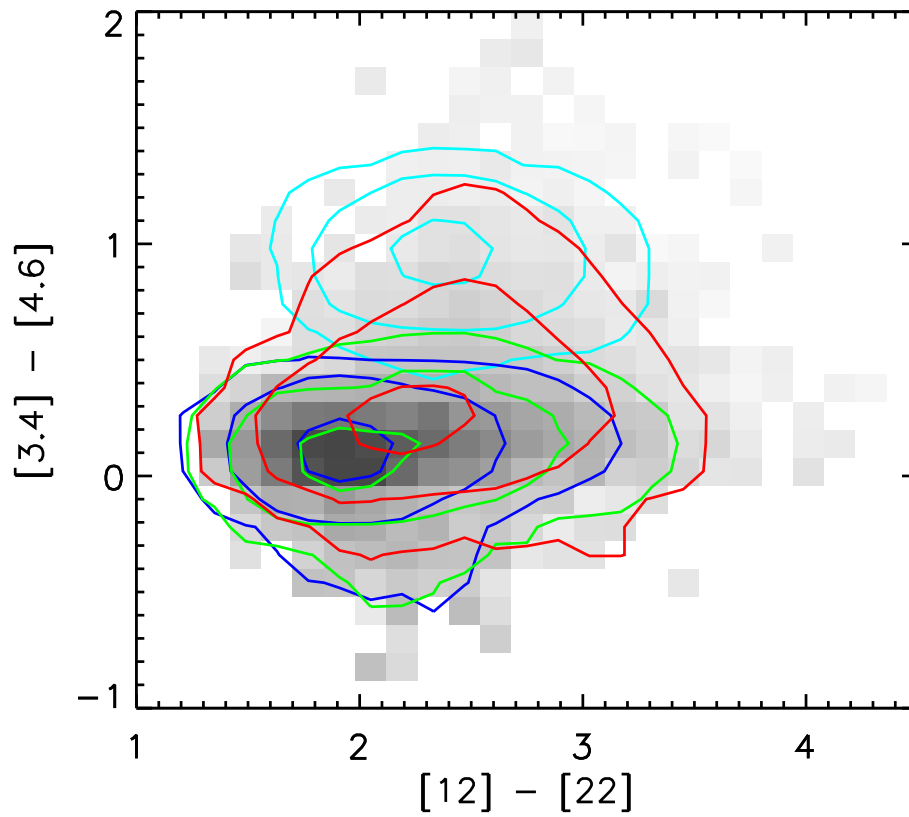


Figure 2.5: The *WISE* color-color diagram. The grey-scale background is the distribution of S2 galaxies on this plane. The blue, green, red and cyan contours are the distributions of star forming galaxies, weak AGNs, strong AGNs and *SDSS* quasars, respectively.

We now examine how the *WISE* colors of AGNs vary as a function of 4000 Å break (i.e. recent star formation) and as a function of BH accretion rate. The latter quantity is estimated based on the extinction-corrected [OIII] line luminosity. We adopt an empirical $M_{\text{BH}}-\sigma$ relation [104] to calculate the BH mass:

$$\log\left(\frac{M_{\text{BH}}}{M_{\odot}}\right) = (8.12 \pm 0.08) + (4.24 \pm 0.41) \log\left(\frac{\sigma}{200 \text{ km s}^{-1}}\right). \quad (2.2)$$

The velocity dispersions in the MPA/JHU catalogue are estimated by fitting the absorption lines in SDSS fiber spectra using a set of template spectra³. The statistical uncertainty is around 10 km/s, leading to ~ 0.05 – 0.2 dex uncertainty of black hole mass, smaller than the intrinsic scatter of the $M_{\text{BH}}-\sigma$ relation (0.44 dex) [104]. Due to SDSS spectral resolution of ~ 70 km/s, the black hole mass estimation is no longer reliable at $\lesssim 10^{6.2} M_{\odot}$. Only a very small fraction of our objects are in this range and they do not affect our results. We do not perform aperture corrections to the derived velocity dispersions because they are small in early type galaxies where AGNs are usually hosted [27]. In this chapter, we will use the Eddington parameter $L[\text{OIII}]/M_{\text{BH}}$ as the optical indicator of the central BH accretion activity level.

The results are displayed in Figure 2.6. The *WISE* colors are shown as a function of 4000 Å break (i.e. host SSFR). The AGNs are divided into 3 different ranges in $L[\text{OIII}]/M_{\text{BH}}$ (see caption). The star forming galaxies are also shown in blue for comparison. Because our *WISE* colors are not K-corrected, we limit the analysis in a relatively small redshift range $0.07 < z < 0.11$, which also lead to an effective stellar mass range of $10^{10.4} M_{\odot} < M_{*} < 10^{11.6} M_{\odot}$ (see Figure 2.1). The conclusions will not change if we use other redshift and stellar mass ranges.

In general, *WISE* colors are redder at higher SSFR. The [3.4] – [22] color is the most sensitive to the star formation. No difference between AGNs and star forming galaxies is observed in the top right panel of Figure 2.6. It indicates that this color is insensitive to AGN activity. In other *WISE* colors, the AGN contribution is more prominent. Stronger AGNs are usually redder at any fixed $D_n(4000)$. The [3.4] – [4.6] and [12] – [22] are the most sensitive colors to BH accretion, and the least to star formation. This is consistent with the observed peak shift between strong AGNs and other populations in Figure 2.5.

In the next sections, we focus on the $4.6 \mu\text{m}$ luminosity as our main IR indicator of AGN activity. Although the difference in color between different Eddington parameter bins is in fact larger for [12] – [22] than [3.4] – [4.6], the loss in sample size is too large due to requiring the AGN samples to be complete at $22 \mu\text{m}$.

2.4 Mid-IR properties of local AGNs

In this section, we will use the $4.6 \mu\text{m}$ luminosity, corrected for stellar contribution, to parametrize the IR properties of AGNs. We will compute how the total IR emissivity from

³<http://spectro.princeton.edu/>

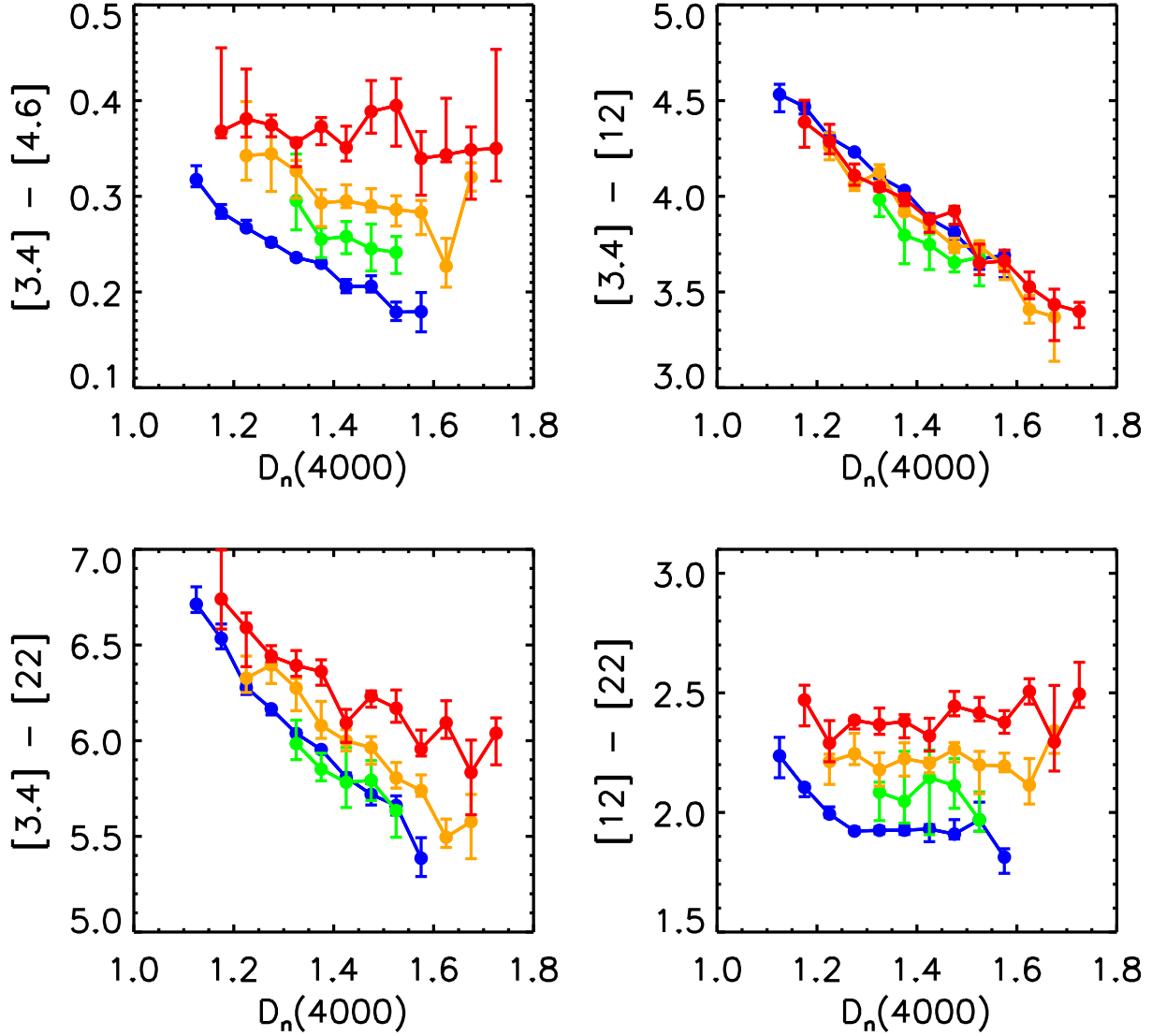


Figure 2.6: The *WISE* colors versus 4000 Å break. The data points are from S2 galaxies in redshift range of $0.07 < z < 0.11$. Blue lines are from normal star forming galaxies. Green, orange and red lines are for strong AGNs with different Eddington ratios: $\log(L[\text{OIII}]/M_{\text{BH}}) < -0.56$, $-0.56 < \log(L[\text{OIII}]/M_{\text{BH}}) < 0.01$, $\log(L[\text{OIII}]/M_{\text{BH}}) > 0.01$ (solar units). The error is 1- σ error of the median value, estimated from bootstrap resampling in each data bin. The data bin with objects less than 20 is discarded.

local AGNs is contributed among galaxies with different AGN and host properties. Finally we will compare these distribution functions to the ones obtained from [OIII].

2.4.1 AGN IR luminosity

In Section 2.3, we have shown that the [3.4] – [4.6] color is the best AGN indicator among the *WISE* colors. This implies that the 4.6 μm luminosity can be used to estimate the mid-IR luminosity which originates from the torus, if we are able to subtract the contribution from stars. In this section, we propose a method to perform this subtraction.

Due to the large sample size of S1, we are able to find non-AGN control galaxies with host properties that can closely match those of the AGNs. For each AGN host galaxy, we search for non-AGN galaxies with similar stellar mass, 4000 Å break, redshift and stellar mass surface density. Matching in stellar mass and $D_n(4000)$ makes sure that the control galaxies have the same total stellar mass and central stellar population ages as that of AGN hosts. Matching in both redshift and stellar surface mass density ensures that the same fraction of the total light of the hosts is inside the *SDSS* fiber aperture. To minimize the scatter, we use strict matching criteria: stellar mass within ± 0.01 dex, 4000 Å break within ± 0.025 , redshift within ± 0.02 , and stellar mass surface density within ± 0.2 dex. For each AGN the contribution of stars to the total 4.6 μm luminosity is estimated from the median 4.6 μm luminosity of all the matched control galaxies. Typically for each AGN hosts, there are 8 non-AGN “neighbours” to give reasonable estimation of the non-AGN component. Then this non-AGN component is subtracted from the observed 4.6 μm luminosity to get a “pure” AGN 4.6 μm luminosity $L_{4.6\mu\text{m,AGN}}$. We note that this correction is only a statistical one. We perform K-correction to this “pure” AGN component with the QSO1 template from galaxy library of M. Polletta et al. [199]. In our redshift range, the correction is less than 5% due to a flat quasar SED in this wavelength.

In some cases, particularly when the AGN is relatively weak, the host-subtracted flux will be negative. Figure 2.7 shows that a great fraction of objects have negative fluxes when $L[\text{OIII}] \lesssim 10^7 L_\odot$ or $L_{4.6\mu\text{m,AGN}} \lesssim 3 \times 10^8 L_\odot$. We also estimate the uncertainty of individual object by calculating the scatter of the 4.6 μm luminosities of its non-AGN “neighbours” used for host subtraction. This yields typical uncertainty of $\sim 2\text{--}7 \times 10^8 L_\odot$ in 4.6 μm luminosity. For AGNs below this luminosity level, the nuclear emission is poorly determined due to low AGN-to-host contrast. Comparing to the whole AGN sample, the Seyfert galaxies are less affected due to their higher nuclear luminosities. Seyferts with positive fluxes always account for a larger proportion even when summing up to the lowest luminosities bins. The 4.6 μm luminosities of Seyferts are better recovered individually, allowing a direct comparison between nuclear IR and [OIII] luminosities. The exact definition of BPT AGNs does not affect the results because the host star formation contribution to both the [OIII] and IR luminosities has been subtracted. Hereafter the AGN IR luminosity refers to host-subtracted luminosity.

The left panel of Figure 2.8 shows that there is a good correlation between the 4.6 μm monochromatic (νL_ν) AGN luminosity and the [OIII] luminosity for Seyferts, although the scatter is large (~ 0.28 dex on average). We exclude the LINERs from the plot, because

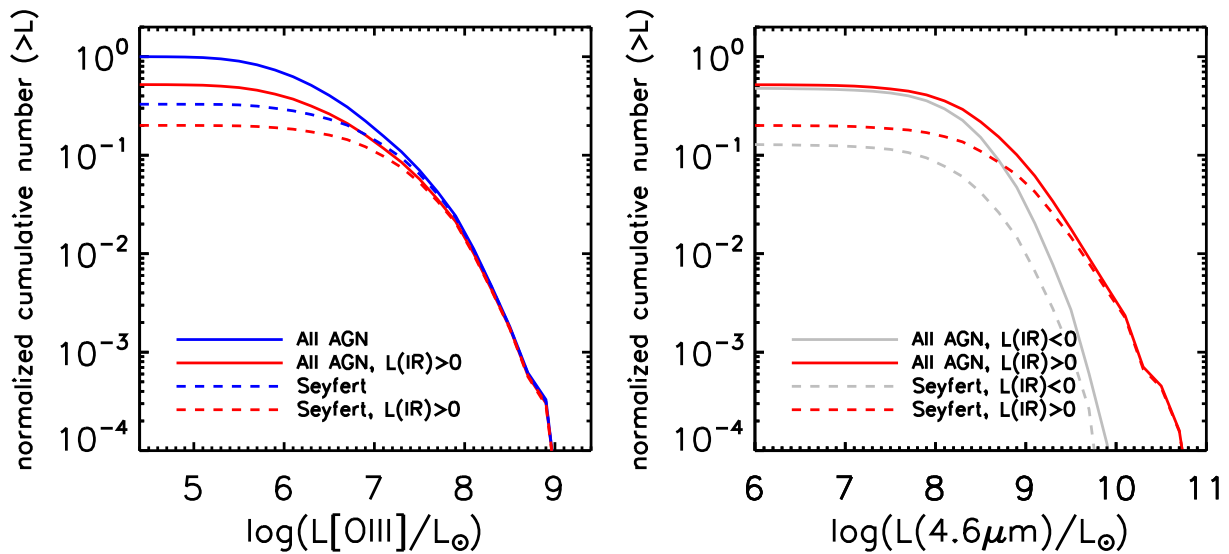


Figure 2.7: The number of objects as a function of [OIII] luminosity (left panel) and $4.6\mu\text{m}$ “pure” AGN luminosity (right panel), normalized by the total number of S1 AGNs. The solid and dashed lines are for all optically selected AGNs and Seyfert galaxies, respectively. In left panel, the blue curve is for all the objects in the subsample and the red curve is for the objects with positive $4.6\mu\text{m}$ luminosities. In right panel, the red curve is the same as left panel. The grey curve is the AGNs with negative $4.6\mu\text{m}$ luminosities, binned by the absolute values of their luminosities. The errors are estimated by bootstrapping within the whole S1 AGN sample.

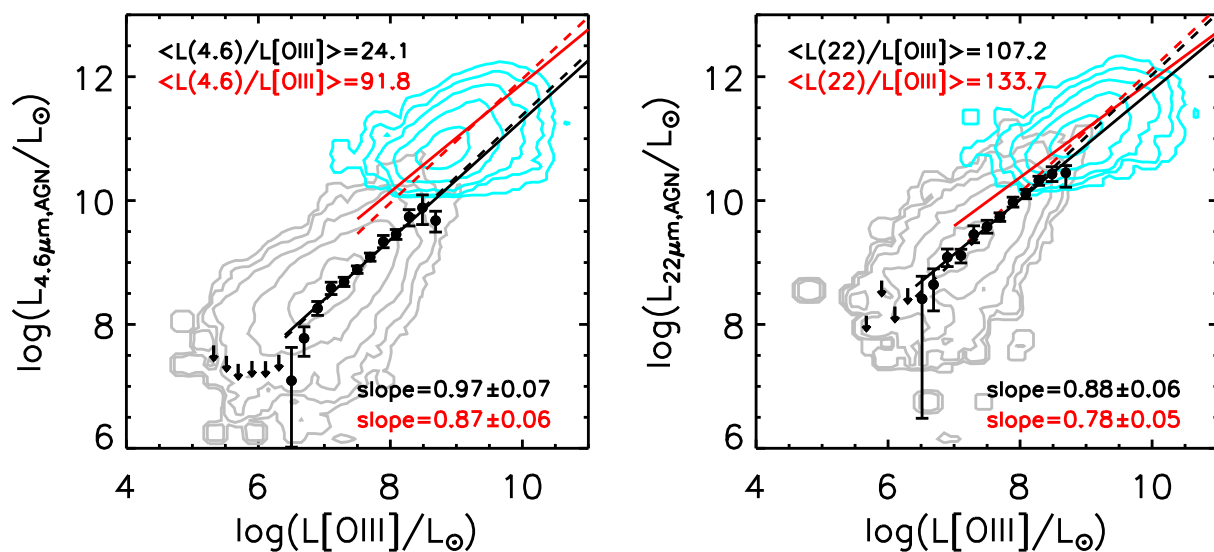


Figure 2.8: Left: $4.6\ \mu\text{m}$ AGN luminosity versus [OIII] luminosity. The grey and cyan contours are S1 Seyferts (with positive AGN $4.6\ \mu\text{m}$ luminosities) and *SDSS* quasars respectively. The black dots and upper limits show results of stacked Seyferts in each [OIII] luminosity bins. The black solid line is a linear fit to the black dots and the resulting slope is shown in bottom-right corner. The black dashed line is a linear fit assuming a constant IR-to-[OIII] ratio. The median value of the IR-to-[OIII] ratio is shown on top-left corner. The red lines are similar to black lines but for quasars. Right: similar to the left panel, except that we use $22\ \mu\text{m}$ luminosities and the local Seyferts are from S2 sample.

the $4.6\ \mu\text{m}$ fluxes of LINERs are not estimated accurately. We stack the Seyferts, no matter they have positive or negative fluxes, in different [OIII] luminosity bins to reduce the uncertainty (black dots and upper limits). The linear fittings are limited to the galaxies with $L[\text{OIII}] > 3 \times 10^6 L_\odot$ because in lower luminosity regime the nuclear emission is not well recovered even with stacking technique. The linear fit to the bright narrow line Seyferts gives a correlation of $L_{4.6\ \mu\text{m,AGN}} \propto L[\text{OIII}]^{0.97 \pm 0.07}$. If we assume the IR luminosity is proportional to [OIII] luminosity, then we get a median IR-to-[OIII] ratio of ~ 24 . These values are, however, only valid for bright objects. We also compare the results with *SDSS* quasars. The quasars extend the correlation a further 2 orders of magnitude in [OIII] and IR luminosities, though there is a systematic offset between quasars and Seyfert galaxies.

Interestingly, if we plot the AGN IR luminosities at $22\ \mu\text{m}$ estimated with similar host subtraction methods, the Seyfert-quasar offset becomes much smaller (see right panel of Figure 2.8). We thus hypothesize that offset may be caused by the intrinsic obscuration of torus: longer wavelengths are less absorbed, and type 1 AGNs may be systematically less obscured than type 2 AGNs. We note that we do not find correlation between the $[4.6] - [12]$ or $[4.6] - [22]$ colors of the AGN component and [OIII] luminosity within Seyfert sample or within the quasar sample.

2.4.2 AGN emissivity and host properties: comparing optical and IR

T. Heckman et al. [110] have investigated the integrated [OIII] luminosity from type 2 AGNs as a function of stellar mass, of stellar surface mass density, of concentration index and of $4000\ \text{\AA}$ break. It was shown that most of the accretion traced by the [OIII] line today is taking place in galaxies with intermediate stellar masses (10^{10} – $\text{few} \times 10^{11} M_\odot$), high surface mass densities (3×10^8 – $3 \times 10^9 M_\odot/\text{kpc}^2$), intermediate concentrations ($R_{90}/R_{50} = 2.2$ – 3.0), and young stellar ages ($D_n(4000) < 1.6$). Here we carry out the same exercise using the integrated $4.6\ \mu\text{m}$ luminosity and compare the results with that obtained from the integrated [OIII] luminosity. We note that in this study we use $4.6\ \mu\text{m}$ luminosities that are corrected for emission from stars and [OIII] luminosities that are corrected for extinction and for the contribution from star formation.

In Figure 2.9 we show the distributions of integrated [OIII] (blue histogram) and $4.6\ \mu\text{m}$ (red histogram) luminosity as a function of a wide variety of different host galaxy parameters. From left to right and from top to bottom, the host galaxy properties investigated in Figure 2.9 are:

1. The [OIII] line luminosity normalized by the black hole mass (Eddington parameter) $L[\text{OIII}]/M_{\text{BH}}$.
2. The black hole mass estimated from the stellar velocity dispersion M_{BH} .
3. Stellar mass M_* .
4. Stellar mass surface density μ_* .

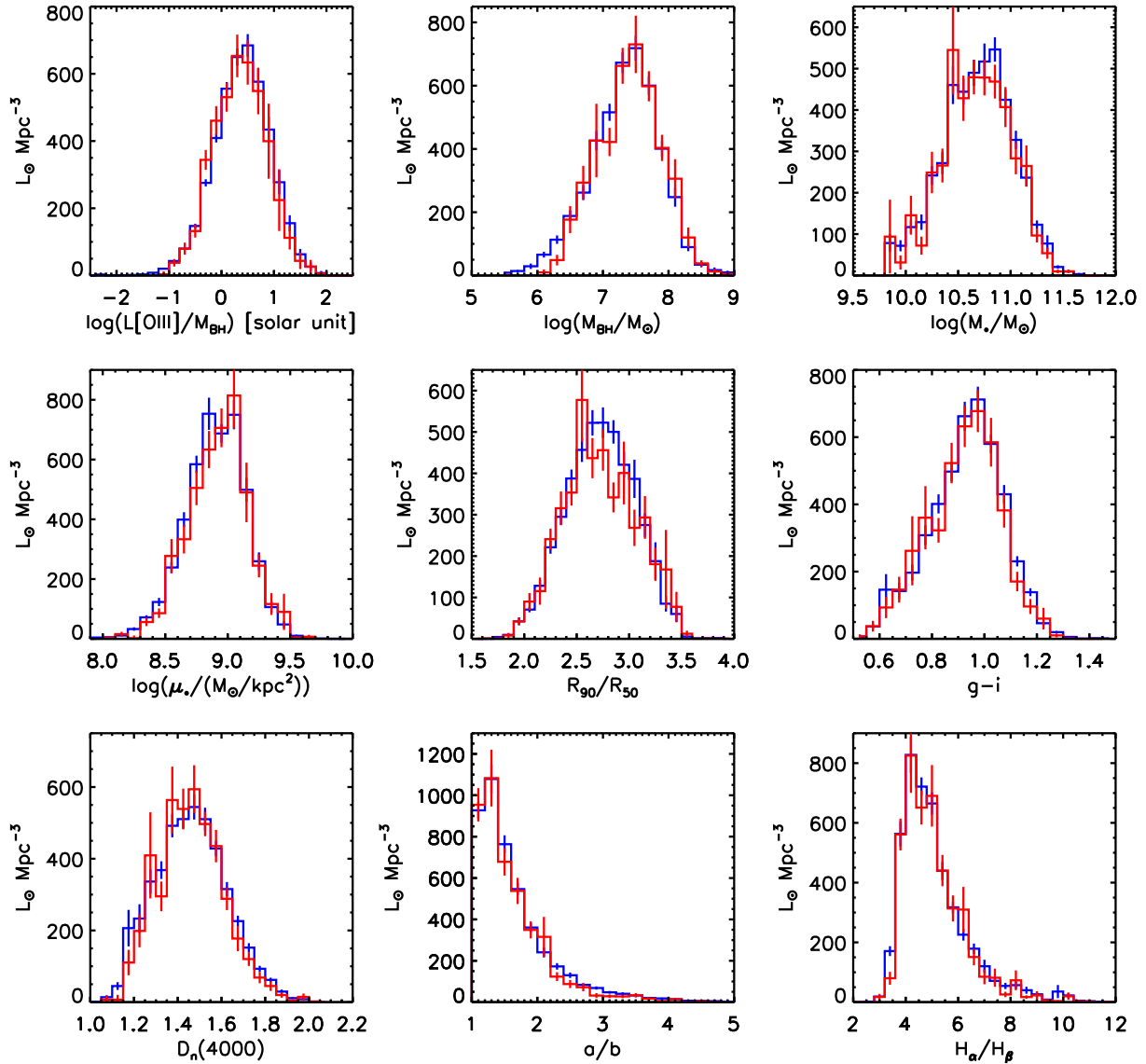


Figure 2.9: The total [OIII] and IR emissivity as a function of various AGN properties for Seyferts (see Section 2.4.2 for details). The blue histogram is for the [OIII] luminosity density and the red histogram is for the $4.6 \mu\text{m}$ luminosity density. The red histogram is scaled down by a factor of 24.2 to compensate the constant ratio between $4.6 \mu\text{m}$ and [OIII] luminosities calibrated in Figure 2.8.

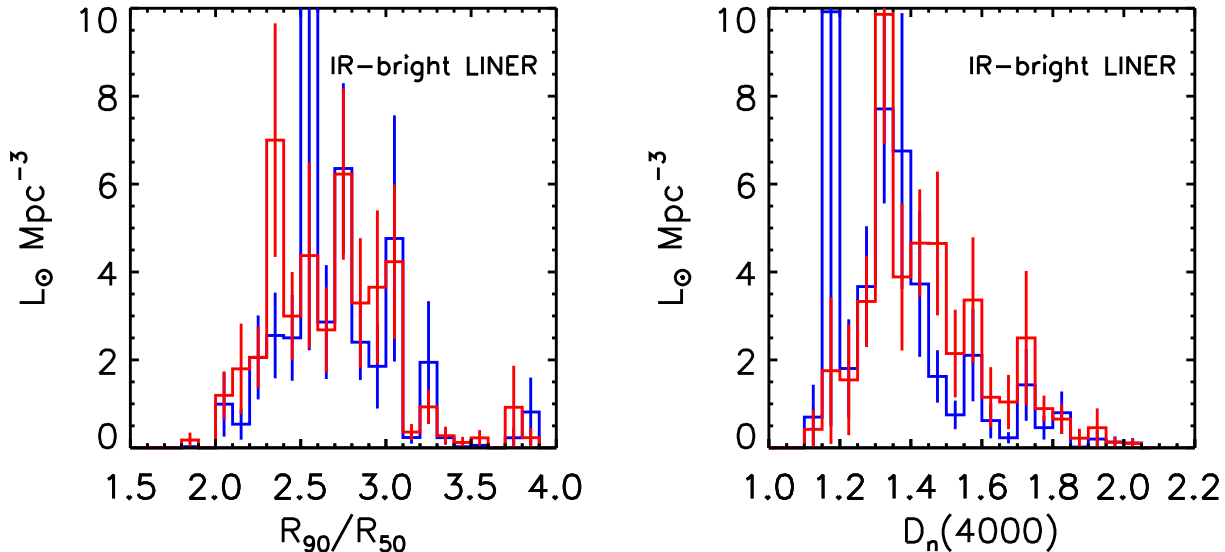


Figure 2.10: Similar to Figure 2.9 but for IR-bright LINERs. Only two of the parameters, concentration index R_{90}/R_{50} and 4000 Å break $D_n(4000)$ are shown here.

5. The concentration index, defined as the ratio between 90% light radius and 50% light radius ratio R_{90}/R_{50} .
6. Rest-frame $g - i$ color.
7. 4000 Å break, $D_n(4000)$.
8. Galaxy inclination estimated from the ratio of the major-to-minor axes, a/b .
9. The Balmer decrement calculated from the ratio of $H\alpha$ to $H\beta$ line fluxes.

Comparison of the red and blue histograms in Figure 2.9 indicates that the host galaxies of the Seyferts producing the integrated $4.6 \mu\text{m}$ luminosity and the integrated [OIII] are identical. This provides strong support for the standard unification model [252]. We again note, however, that in our sample, detection of low luminosity mid-IR emission from the central source is impossible because of host galaxy contamination. In order to avoid spurious result due to objects with negative IR luminosities, we check the emissivity distributions of a sample of 671 IR-bright Seyferts with positive AGN $4.6 \mu\text{m}$ luminosities larger than $10^{9.5} L_{\odot}$. At this level, the AGN component is comparable or stronger than the host component at $4.6 \mu\text{m}$. The individual detection of AGN component is relatively reliable.

We also investigate a sample of 134 IR-bright LINERs, as shown in Figure 2.10. Despite the large uncertainties, the IR-bright LINERs show consistent [OIII] and IR luminosity distributions. However, we fail to establish this kind of [OIII]-IR link for all the LINERs. We find the [OIII] luminosity distribution of the whole LINER sample shifts towards bulge-dominated galaxies with high 4000 Å break strengths. It is probably due to the fact that

LINERs hosted by old elliptical galaxies have relatively weaker AGN luminosities than Seyferts, and we are not able to detect the nuclear IR component for these low luminosity objects.

2.5 AGNs selected by mid-IR colors

In this section, we study a sub-population of galaxies identified as AGN purely from their *WISE* colors, independent from the optical emission line diagnostics. We start from a brief review of IR-color based AGN selection methods.

2.5.1 *WISE* IR AGN selection

The original IR color-color selection techniques were based on the *Spitzer* IRAC colors [145, 233, 203, 69]. This selection method was extended to *WISE* bands by using multi-wavelength synthesized data and galaxy templates [8]. It is then tested with real data, leading to a simpler criterion $[3.4] - [4.6] > 0.8$ [232]. However, we note that their selection methods are tuned for searching AGNs at higher redshifts. If we adopt this cut, we only find 435 objects from sample S1.

Another similar but stricter way to select AGNs is the IR power-law selection, which was first applied to *Spitzer* IRAC data [6]. It is based on the knowledge that the AGN continuum in quasars has a power-law form. In practice, we make use of all four *WISE* bands and fit the broadband SED as follows:

$$0.4 \times M_{\text{AB}} = -\alpha \times \log(\lambda/1 \mu\text{m}) + c. \quad (2.3)$$

Here M_{AB} is the monochromatic AB magnitude and λ is the effective wavelength in each *WISE* bands. The free parameter α is spectral slope ($f_\nu \propto \nu^\alpha$). AGNs are required to have spectral slope that are sufficiently red ($\alpha < -0.5$). The quality of the fit, i.e. the similarity of the SED shape to a pure power law, can be quantified by χ^2 . A sample selected with looser χ^2 threshold will include more galaxies, but also be contaminated by more star forming galaxies. In Figure 2.11, we plot the fraction of optically-selected AGNs as a function of threshold in reduced χ^2 statistics. Results are shown for all AGN (open symbols) and for strong AGN (filled symbols). As can be seen the fraction of optically-identified sources drops sharply above $\chi^2 \approx 1.5$, particularly for strong AGN. We therefore select this as a threshold, which yields a sample of 503 IR-selected power-law AGNs.

Table 2.4 shows the number of the IR AGNs with different selection methods. In total, we find 654 IR AGN. The fraction of optically identified AGN is high (85.3%). We note that this is a much smaller number than could be identified optically. It is clear that IR AGN selection methods based on *WISE* colors will miss a large fraction of type 2 AGNs at low redshift. It is not a surprising result. Previous works based on AGN samples selected in other bands have shown that this is the same situation at higher redshifts [45, 42, 9]. Simple mid-IR color selected AGN samples are clearly biased. It is necessary to use decomposition methods in mid-IR regime for an unbiased AGN study [174].

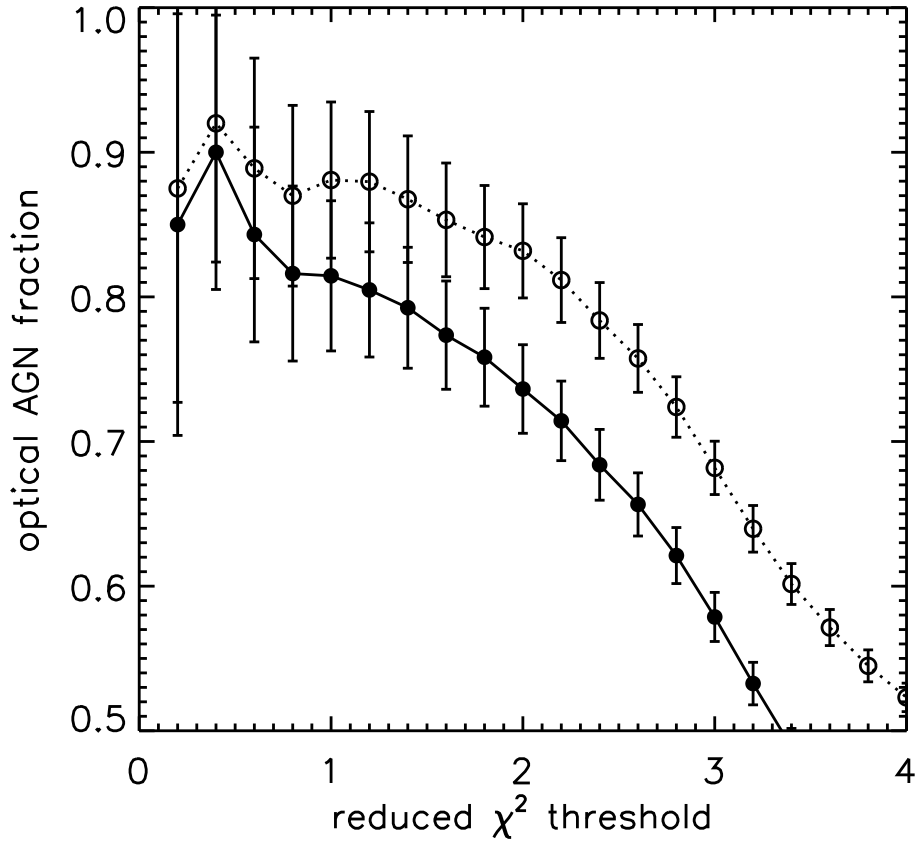


Figure 2.11: The fraction of optically-identified AGNs in the population that meet our mid-IR power-law selection criterion $\alpha < -0.5$ as a function of reduced χ^2 threshold. The solid circles and empty circles indicate strong and all optical AGNs, respectively. The errors are estimated by assuming simple Poisson noise in counting.

IR selection	All	optical AGN	optical strong AGN
col	435	379 (87.1%)	358 (82.3%)
pow	503	434 (86.3%)	394 (78.3%)
col & pow	284	255 (89.8%)	243 (85.6%)
all	654	558 (85.3%)	509 (77.8%)

Table 2.4: The numbers of IR selected AGN samples. “col” and “pow” are the [3.4] – [4.6] color selection and the power law selection, respectively. Symbol “&” means the sources are selected by both methods. “all” means the sources selected by any of the IR selections.

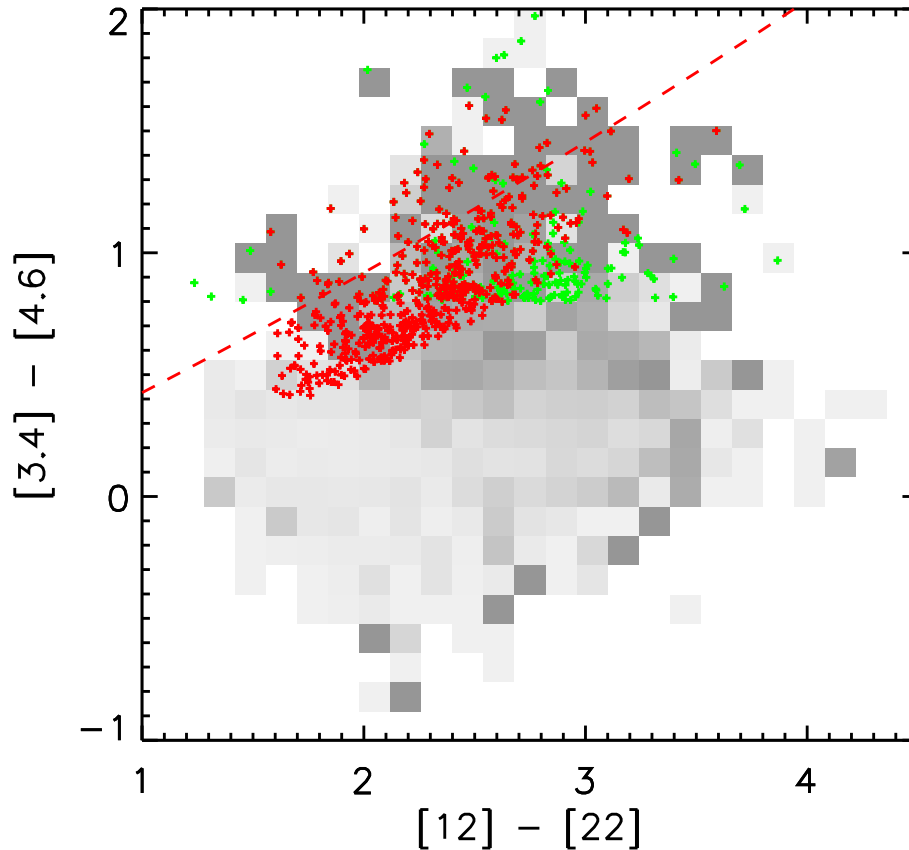


Figure 2.12: Similar to Figure 2.5 but the grey scaled background shows the fraction of strong optical AGNs among S2 galaxies. The green and red crosses indicate $[3.4] - [4.6]$ color and power-law selected AGNs. The red dashed line is the track of a pure power-law spectrum.

2.5.2 The SEDs of IR color selected AGNs

Figure 2.12 shows the distributions of the IR AGN samples on the *WISE* color-color diagram as in Figure 2.5. Green and red crosses indicate sources selected by the simple $[3.4] - [4.6]$ color cut and the power-law method. The colors of IR AGNs are consistent with typical quasar SEDs and clearly different from those of star forming galaxies.

We use all the available photometric data, which covers 5 *SDSS* bands, 3 near-IR bands (*2MASS* bands, from NYU Value-Added Galaxy Catalog [31]) and 4 *WISE* bands, to build SED for each source. The SEDs are shown in AB magnitudes in the rest frame, interpolated from neighboring data points. The detection rates of *WISE* $12\ \mu\text{m}$ and $22\ \mu\text{m}$ bands are relatively low in S1, so we use sample S2 instead. We note this does not affect our conclusion.

Figure 2.13 shows that the two IR selection methods lead to similar SED shapes. IR AGNs are similar to field galaxies in the optical and near-IR bands, but clearly different beyond $3\ \mu\text{m}$. All galaxies, except the passive ones with little dust emission, show a

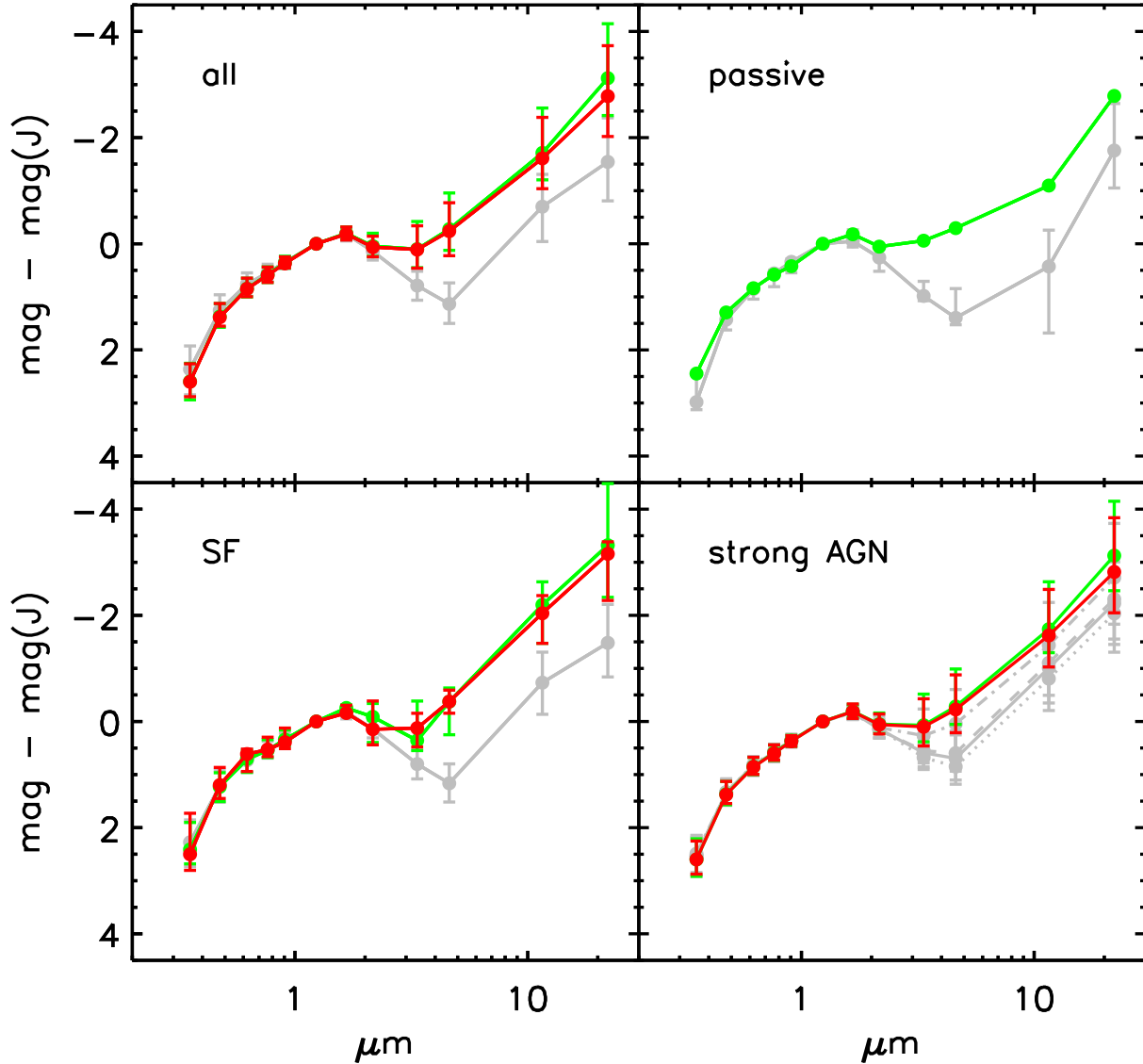


Figure 2.13: Rest frame median SEDs of different subclasses of S2 galaxies. All SEDs are normalized at $\sim 1 \mu\text{m}$ (J band). Grey, green and red curves are for the whole S2 sample, IR color selected AGN and power law selected AGN, respectively. In the bottom-right panel, all S2 strong AGNs with positive $4.6 \mu\text{m}$ luminosities are further split into three luminosity bins, $L_{4.6 \mu\text{m}, \text{AGN}} < 10^{8.8} L_{\odot}$ (dotted line), $10^{8.8} L_{\odot} < L_{4.6 \mu\text{m}, \text{AGN}} < 10^{9.3} L_{\odot}$ (dashed line) and $L_{4.6 \mu\text{m}, \text{AGN}} > 10^{9.3} L_{\odot}$ (dash-dotted line). The error bar is the 1σ scatter. The four panels are for galaxy subsets with different optical classifications, indicated as labels.

clear turnover at $\sim 5 \mu\text{m}$. This wavelength is the point where the dust emission starts to dominate the total radiation output, for galaxies with ongoing star formation and/or AGN activity. In most cases the AGN component is not prominent in mid-IR. Only the AGNs with the highest nuclear IR luminosities ($L_{4.6 \mu\text{m}, \text{AGN}} > 10^{9.3} L_{\odot}$, dash-dotted line) can be distinguished by their mid-IR colors when the turnover moves to shorter wavelength ($\sim 3 \mu\text{m}$). This can strongly affect the $[3.4] - [4.6]$ colors. There are 9 passive galaxies in S2, shown in the top-right panel. The origin of their $12 \mu\text{m}$ and $22 \mu\text{m}$ fluxes is still unknown. One possible explanation is highly dust obscured star formation and/or AGN activity, which the optical emission line diagnostics may fail to identify [205, 39].

2.5.3 Optical properties of IR color selected AGNs

As shown in the previous section, both IR AGN selection methods lead to consistent SED shapes, so we simply combine the two IR AGN samples. In Figure 2.14 we compare IR AGNs with optical weak and strong AGNs, on the number distributions over [OIII] luminosity, Eddington parameter, 4000 \AA break and D(BPT), the distance to the K03 line [129] on BPT diagram (“pure” AGNs have the largest D values). Unlike Figure 2.9, this plot shows fraction by number rather than fraction of the integrated IR or [OIII] emissivity. We find that at low redshift the IR selected AGNs have similar [OIII] luminosities and 4000 \AA break strengths as strong optical AGNs, but have even higher Eddington parameters and D parameters. This is because the mid-IR colors are much more sensitive to star formation in host galaxy than optical emission lines, i.e. [OIII]/ $H\beta$ and [NII]/ $H\alpha$ ratios. Only strongly accreting black hole with the highest Eddington parameters are selected by IR color-based techniques.

2.5.4 Optically-unidentified IR color selected AGNs

Though the IR AGNs are found to be similar to strong optical AGNs, there is a small fraction of objects not identified as AGNs from their optical emission lines. This holds for both IR selection methods. In total there are 96 (14.7%) IR AGNs that are not classified as AGN in the optical. We call them “IR-only” AGNs for short.

In general there are two cases that optical identification will fail. One is that they are mis-classified as star forming galaxies, due to the host contamination. The second possibility is that at least one of the four key emission lines used in BPT classification is not detected.

We find about 20% of IR-only AGNs are optically identified as star forming galaxies (hereafter we call them SF-IR-only AGNs). Most of them (15 out of 19 sources) are relatively metal rich ($\log([\text{NII}]/\text{H}\alpha) > -0.6$) and are located close to the star formation/AGN separation line. Since this separation line is not physical, they might host AGNs despite the high host contribution to emission lines. There are also 4-metal poor SF-IR-only AGNs ($\log([\text{NII}]/\text{H}\alpha) < -0.6$) that fall on the left side of the BPT diagram. Metal-poor AGNs are rare and occur in less massive galaxies [102]. Three of them have $[3.4] - [4.6]$ and $[12] - [22]$ consistent with normal galaxies, so it is difficult to judge whether these galaxies

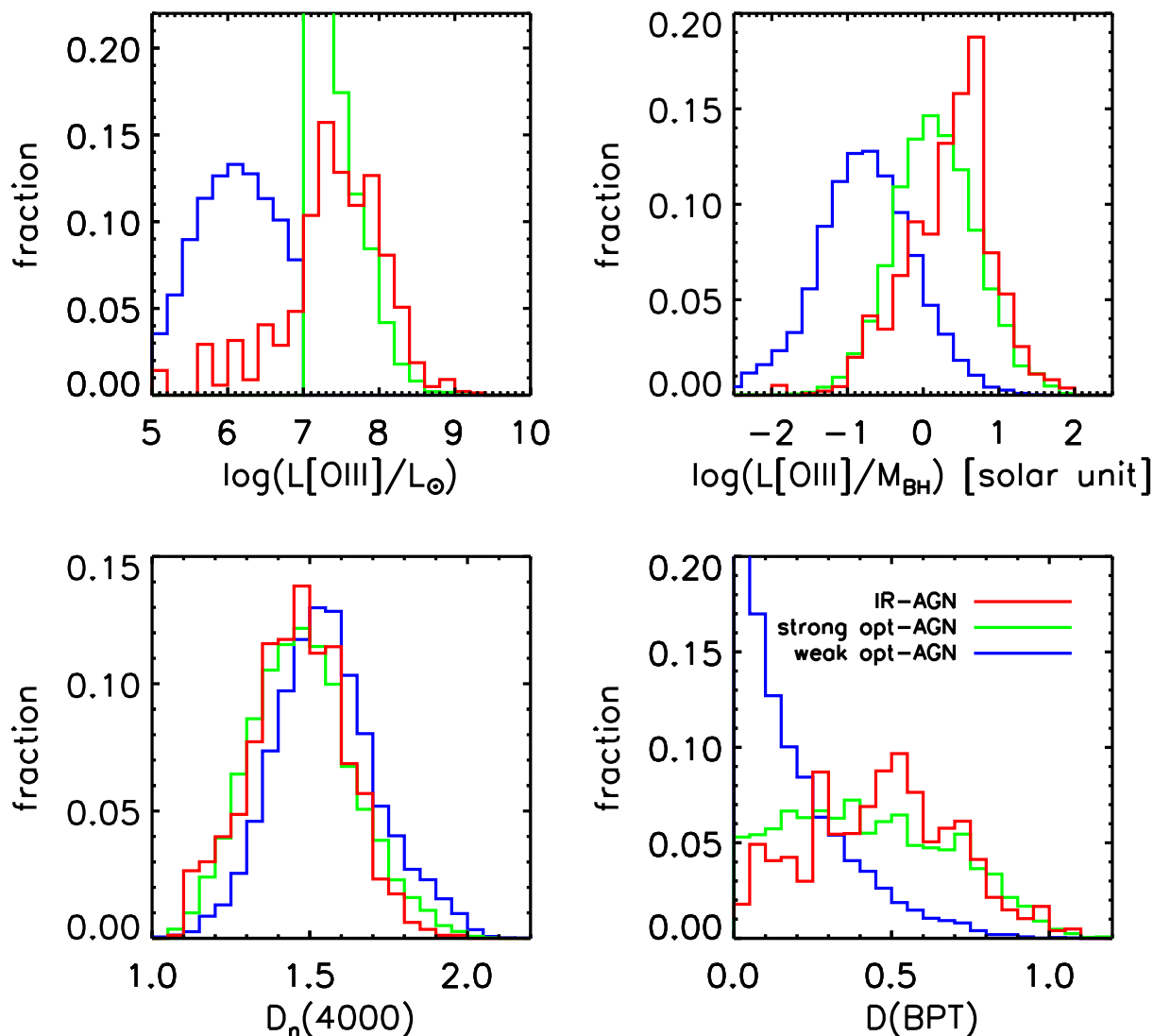


Figure 2.14: The number distributions of IR AGNs (red), strong optical AGNs (green) and weak optical AGNs (blue) over AGN/host properties. The properties shown here are [OIII] luminosity, Eddington parameter, 4000 Å break and $D(\text{BPT})$. $D(\text{BPT})$ is the distance to the K03 line [129] on the BPT diagram. “Pure” AGNs have the largest $D(\text{BPT})$ values.

are true AGNs or not. However, interestingly, the left one object has $[3.4] - [4.6] = 1.1$ and $[12] - [22] = 7.2$. It is clearly an AGN-dominated object with relatively low stellar mass $M_* \approx 10^{9.8} M_\odot$.

The majority of our IR-only AGNs (77 objects, 80% of the population), are optically unidentified, just because one or more emission lines are not detected. In most cases, it is the $H\beta$ line measurement that has low SNR. We find they are consistent with Seyfert galaxies by estimating the lower limit on their $[\text{OIII}]/H\beta$ ratio. In conclusion, as far as we can tell, the IR AGNs without optical classification do not constitute a special class of object.

2.6 Discussion

In this chapter, we have matched a large sample of *SDSS* galaxies at redshift $0.02 < z < 0.21$ with mid-IR photometry from *WISE*. The aim of this study is to investigate the host galaxy properties of AGNs by using the mid-IR luminosity as our AGN activity indicator, and compare the results with previous studies using $[\text{OIII}]$ line luminosities.

As an AGN activity indicator, $[\text{OIII}]$ line luminosity has an advantage that it is relatively insensitive to contamination by young stars. In HII regions the $[\text{OIII}]$ luminosity is known to be weak. However, the ionized gas which is emitting $[\text{OIII}]$ line is located at distances of hundreds parsecs from the galaxy center. The $[\text{OIII}]$ luminosity is an indirect indicator of current accretion onto the central black hole. In contrast, from recent high-resolution mid-IR observations it is indicated that the scale of the “torus” around the black hole is no more than a few parsecs [124, 245, 21, 44, 246, 138, 137, 136, 114]. It provides a better probe to ongoing accretion on much smaller scales. However, a large fraction of the total mid-IR emission in the galaxies are from stars. At around $3 \mu\text{m}$ the emission from stars older than 1 Gyr dominates. At longer wavelength, the emission from dusty interstellar medium is important.

We use the 4000 \AA break strength, from *SDSS* spectra, as the main indicator of the stellar age, i.e. the average star formation in past a few Gyr. We first systematically study the *WISE* colors of AGN hosts as a function of both stellar age and optical “Eddington parameter” ($L[\text{OIII}]/M_{\text{BH}}$). We find that the $[3.4] - [4.6]$ color has the weakest dependence on $D_n(4000)$, but strong dependence on $L[\text{OIII}]/M_{\text{BH}}$. We use a “pair-matching” technique [128] to statistically subtract the $4.6 \mu\text{m}$ stellar emission contributed by the host galaxies, by searching for non-AGN galaxies with similar redshifts, stellar masses, sizes and 4000 \AA break strengths as the AGN host galaxies. We use these corrected $4.6 \mu\text{m}$ luminosities to probe the strength of the central torus emission for the AGN in our sample. We show that intrinsic $4.6 \mu\text{m}$ AGN luminosities can be recovered for most Seyferts, but only statistically for LINERs.

By combining the Seyfert galaxies with a sample of *SDSS* quasars at $z < 0.7$, we find the linear correlation between $[\text{OIII}]$ and $4.6 \mu\text{m}$ luminosities expands for 4 orders of magnitude in luminosity. However, there is an offset between Seyferts and quasars, as well as substantial scatter, in this relation, probably due to intrinsic torus obscuration which is not

accounted in this study and the uncertainty of the host subtraction processes. In order to gain further insight, we perform a systematic comparison of the AGN host galaxy properties if the nuclear luminosity is presented by $4.6\ \mu\text{m}$ luminosity instead of [OIII] luminosity. We quantify the change using the partition function of the total integrated IR/[OIII] line luminosity from type 2 AGNs as a function of a variety of host galaxy properties, including stellar mass, structural properties, stellar population ages and interstellar medium dust content.

We find identical distributions of total $4.6\ \mu\text{m}$ and [OIII] line luminosity for Seyfert galaxies and IR-bright LINERs, in strong support of the standard unification model [147]. We also note that if we divide our sample by optical Eddington parameter or $4.6\ \mu\text{m}$ luminosity scaled by black hole mass and if we repeat the comparisons using the 25% of the emission coming from the IR and optical sources with the *highest accretion rates*, host galaxy properties are also identical.

Finally, we note that we searched the entire *SDSS* spectroscopic catalogue for AGN that could only be identified as such using *WISE* photometry. We found a total of 96 such systems. A detailed analysis revealed that there was nothing special about these objects: in most of them, the S/N in the $\text{H}\beta$ line was simply too low to allow a reliable BPT classification. One might be tempted to conclude, therefore, that no differences exist between the optical and IR “views” of low redshift AGN.

Chapter 3

AGNs and Galaxy Interactions

3.1 Introduction

In Chapter 2 we have discussed the AGN torus emission and the AGN host properties in IR view. The result implies a close link between the host star formation and the existence of torus. However, one may ask what is causing this close connection. Just as mentioned in Section 1.2.2, it is commonly believed that the cold gas is the major source to feed both the star formation and the central supermassive BH growth [129, 110, 126, 181]. It is probable that the gas supply and feeding mechanisms are the key factors to regulate both processes.

There are several mechanisms, internal and external, to transport the cold gas from outskirts, where the baryon material is not dense enough to collapse and form stars, to inner region of the galaxy (see also Section 1.2.3). Galaxy mergers and interactions are well known as one of the most important external factors to cause the gas inflow, which can enhance the star formation in galaxies, observationally [262, 261, 75, 149, 139] and theoretically [180, 230, 65]. This naturally leads to a hypothesis that there is a tight connection between AGN activity and galaxy-galaxy interactions [5, 74, 153, 51]. However, many previous studies show results against this hypothesis [75, 96, 62, 224, 140, 32]. Some of the discrepancies could be attributed to the differences of sample sizes, methods used to define merger/interaction, evolutionary effect at different redshift, etc. The definition of AGN activity may also be important in this kind of studies.

Based on the knowledge that there is strong correlation between star formation and the strength of clustering, C. Li et al. show that *at similar host star formation level*, AGNs with higher accretion rate do not require *additional* interaction strengths [150]. This means although the galaxy-galaxy interactions accelerate the host star formation, the nuclear activity is somehow not directly enhanced. If the probed AGN activity is purely supported by the cold gas accretion, then their result suggests that the galaxy-galaxy interactions can feed the gas to host galaxy but do not drive the gas from the kiloparsec scale to parsec scale. Some other mechanisms may contribute to this gas inflow [77, 158].

C. Li et al. use narrow [OIII] emission line as the AGN activity indicator [110]. However,

as mentioned in Chapter 2, the [OIII] line luminosity is an indirect measurement of the black hole accretion rate. In this chapter, we will use the IR emission as AGN activity indicator, as we did in Chapter 2, to study the effect of galaxy clustering. Their study is based on sample including both Seyfert galaxies and LINERs. But we have already shown that the IR nuclear emission of LINERs are not well recovered. It is also suggested that local AGNs hosted by old passive galaxies, which are consistent with general properties of the LINER population, are fed by stellar wind of evolved stars [126]. If this is the case, then the triggering of LINERs are not necessarily connected with interactions. Including LINERs into this study may dilute the merging signal. Also there are debates on whether the LINERs are true AGNs or not [47, 266]. Hence, in this study we will focus only on Seyfert galaxies.

3.2 Data and Results

In this chapter, the database is identical to that we use in Chapter 2, i.e. the galaxies with *SDSS* spectra within r -band magnitude range of $14.5 < r < 17.6$, stellar mass range of $10^{9.8} M_{\odot} < M_{*} < 10^{11.8} M_{\odot}$ and redshift range of $0.02 < z < 0.21$. The optical classifications, the star formation and extinction correction to AGN [OIII] luminosity is performed in exactly the same way. The IR AGN luminosities are again, obtained by subtracting host contribution from the observed luminosities, in each of the *WISE* bands. In later text of this chapter, the IR luminosities refer to the AGN component unless specifically noted. The only difference is that in this chapter, we do not use the redshift limits for each stellar mass bin, so that the parent galaxy sample is no longer "stellar mass complete" sample. By doing this we gain a much larger parent sample S0: in total there are 18727 Seyferts in S0.

We calculate the averaged number of close neighbors of AGNs using the method described by Li et al. [151]. We count the number of galaxies in the *SDSS* photometric sample with a given r -band magnitude limit, within a given value of projected radius R_p . We estimate the background due to chance projection by calculating the counts around randomly placed galaxies within the *SDSS* coverage. The error is estimated by bootstrapping within the sample.

Figure 3.1 shows the background-subtracted averaged number of close neighbors within certain projected radius for different subsamples of Seyferts and with different limiting magnitudes. In top, middle and bottom panels, the magnitude limits of the photometric sample, which is used to counting the neighbors, are 20.0, 19.0 and 18.0, respectively. From bottom to top, fainter magnitude limits means more and more fainter neighbors are included in the counting analysis. In left, middle and right panels, the Seyfert galaxies are split into 2 subsamples, binned by different $L[\text{OIII}]/M_{\text{BH}}$, $L_{4.6\mu\text{m,AGN}}/M_{\text{BH}}$ and $L_{22\mu\text{m,AGN}}/M_{\text{BH}}$, respectively. In each individual panel, the 2 subsamples are matched at redshift, stellar mass, concentration and 4000 Å break. The matching box is small: $\Delta z < 0.01$; $\Delta(\log(M_{*})) < 0.1$; $\Delta(R_{90}/R_{50}) < 0.2$ and $\Delta D_n(4000) < 0.05$. So we make sure that they are compared at similar redshift, with similar Hubble type and at the same level

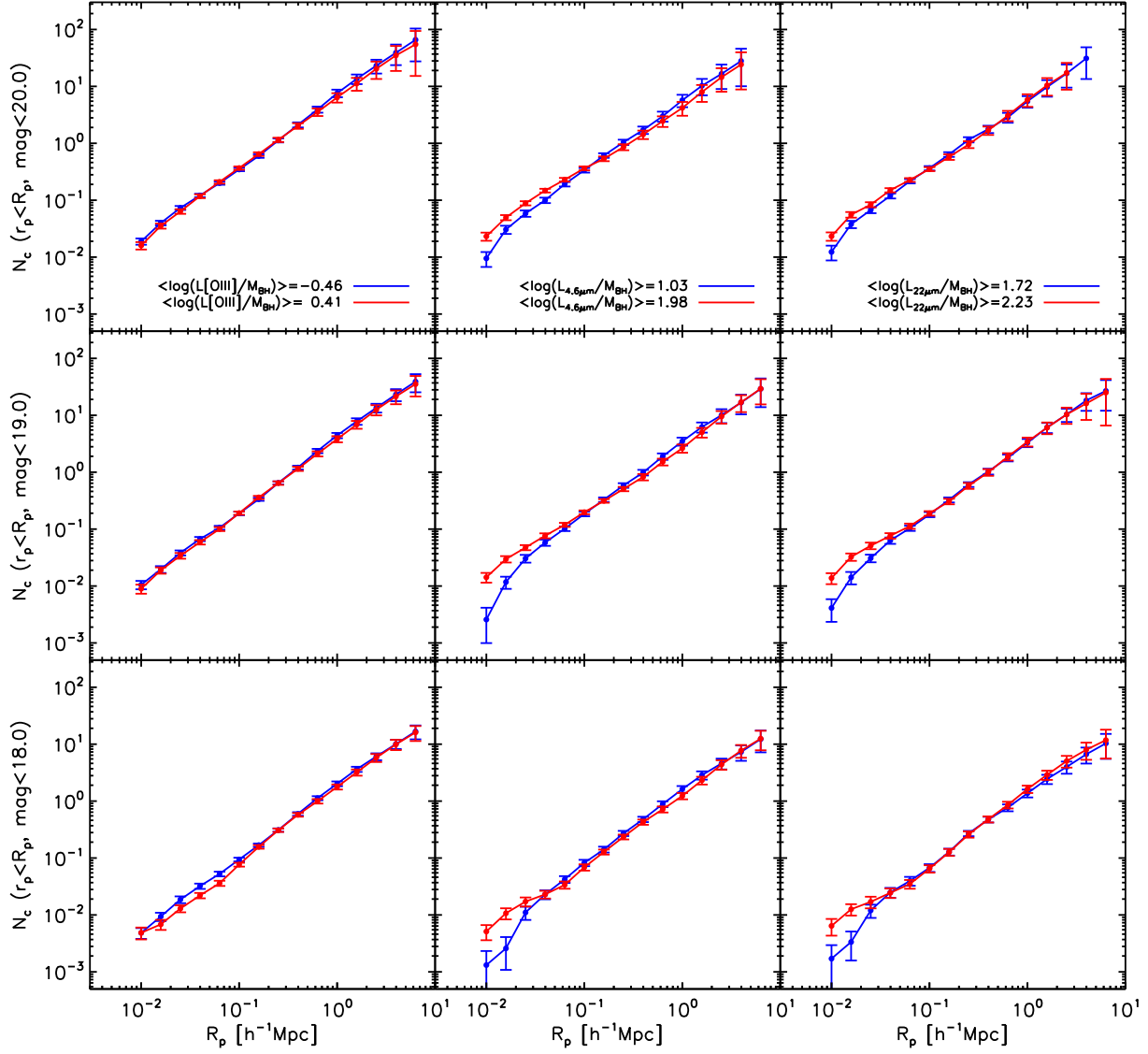


Figure 3.1: The average number of neighbors within a given value of projected radius. Top, middle and bottom panels are for different magnitude limits of the SDSS photometric sample used for neighbor counting. Left, middle and right panels are Seyferts binned by different $L[\text{OIII}]/M_{\text{BH}}$, $L_{4.6\mu\text{m,AGN}}/M_{\text{BH}}$ and $L_{22\mu\text{m,AGN}}/M_{\text{BH}}$, respectively. The results from different bins are displayed in different colors, as shown in the legend.

of star formation activity.

From left panels, we can see that the AGN activities indicated by [OIII] line emission have no dependence on the existence of neighbor galaxies, consistent with the results shown by Li et al. [150]. At large scale > 100 kpc, this is still true if we compare the AGNs with different $L_{4.6\mu\text{m,AGN}}/M_{\text{BH}}$ or $L_{22\mu\text{m,AGN}}/M_{\text{BH}}$. However, at small scale of 10 to 100 kpc, there is neighbor counts excess for AGNs with higher $L_{4.6\mu\text{m,AGN}}/M_{\text{BH}}$ and $L_{22\mu\text{m,AGN}}/M_{\text{BH}}$. The excess signal seems strong at the high magnitude limit $r = 18.0$ and $r = 19.0$, and becomes weaker at $r = 20.0$. It may imply the signal is mainly contributed by the brightest neighbors. We find consistent results for AGN subsamples divided by different $L_{4.6\mu\text{m,AGN}}/L[\text{OIII}]$ and $L_{22\mu\text{m,AGN}}/L[\text{OIII}]$ either (see Figure 3.2).

The scatter of the [OIII]IR relation is expected to be (at least partly) contributed by the absorption (see also Section 2.4.1). This may cause complex interpretation to the observed connection between IR emission and neighbor count excess. However, as we have already shown that at $22\mu\text{m}$ the intrinsic obscuration is no longer important in Figure 2.8, the detection of neighbor excess at both $4.6\mu\text{m}$ and $22\mu\text{m}$ suggests result is unlikely affected by the obscuration. A further test of obscuration against neighbor counts excess confirms this (see Figure 3.2).

3.3 Discussion

In this chapter, we have used the neighbor counts technique to study the relation between of AGN activities and the galaxy interactions. The conclusion is rather clear and simple: for local Seyfert 2 galaxies, the IR-bright AGNs are connected with galaxy-galaxy interactions. AGNs with higher IR luminosities or IR-to-optical ratios are more likely to be surrounded by companion galaxies within the projected distance of 100 kpc. As we will show later in Chapter 4, the local Seyfert 2 galaxies are probably affected by “merger-like” mechanism.

As mentioned in Chapter 1, it is known that the powerful AGNs are linked with star formation and the link is stronger at smaller scales. On the other hand, the star formation is known to be enhanced by galaxy interactions. So it seems plausible to find a connection between AGN and galaxy interactions. However, this link was not well established, especially for local AGNs. In the 2008 work by C. Li et al., the attempt to find neighbor counts excess for [OIII] bright AGNs was somehow failed. In contrary, our result using mid-IR luminosities suggests the IR emission can reveal the hidden link.

The contradictory results urge for better understanding the difference between AGN [OIII] and IR emission. The IR luminosity from the torus is reflecting the obscured part of the total AGN radiation power, while the [OIII] luminosity is actually indicator of the unobscured part. The IR-to-optical ratio is a direct probe of the torus covering factor, which is a global physical quantity directly related to the thickness of the torus. In a recent theoretical paper, P. Hopkins et al. suggest that the torus could form during the cold gas inflow, and the large thickness of torus could be caused by inflow-induced instabilities, like warps [118]. This model clearly links the torus covering factor to the cold gas inflow, which will be enhanced by galaxy interactions. The IR-neighbors connection implies that

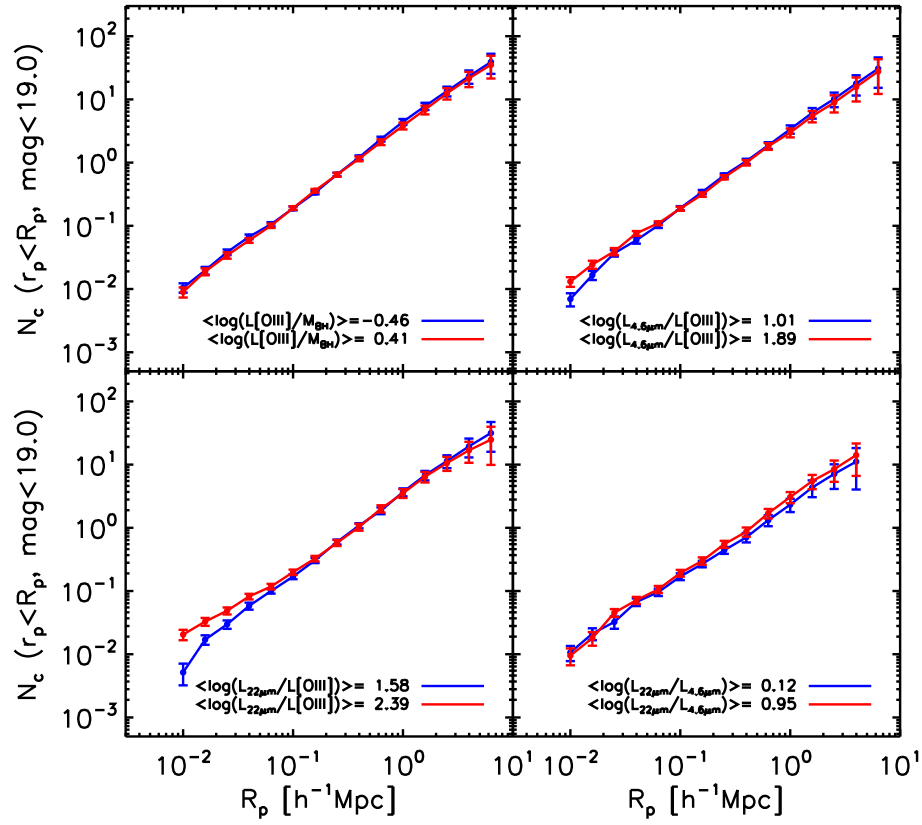


Figure 3.2: Same as Figure 3.1 but with photometric sample magnitude limit of $r < 19.0$ and the Seyfert sample binned by different properties: $L[\text{OIII}]/M_{\text{BH}}$, $L_{4.6\mu\text{m,AGN}}/L[\text{OIII}]$, $L_{22\mu\text{m,AGN}}/L[\text{OIII}]$ and $L_{22\mu\text{m,AGN}}/L_{4.6\mu\text{m,AGN}}$.

the galaxy interactions are responsible to transport the cold gas into the region where the dusty torus resides (usually the central ~ 100 parsecs).

This thicken torus may effectively reduce the luminosity and hence also the visibility of [OIII] narrow line. It is possible that there is a time delay between the galaxy interaction and the unobscured nuclear emission to be revealed, simply due to this obscuration, as C. Li et al. suggested in their 2008 paper. When the interaction occurs, the host star formation, the torus formation and the AGN activity will be triggered. The inflow-induced torus thickening will cause significant IR emission while the [OIII] emission will be relatively suppressed due to increased covering factor, similar to the case of ULIRGs. At later stage, the constant heating of torus by the radiation from accretion disk will gradually destroy the dusty torus. The torus will become thinner if the interaction stops and there is no longer sufficient gas inflow to maintain the thick structure. This time delay will cause the missing link between [OIII] and neighbor counts excess, while the link to IR emission will be largely unaffected by the obscuration. However, we have already known that the host galaxies of IR and optical AGNs have the same stellar mass and black hole mass distribution (see Section 2.4.2). If this kind of delay exists, the time scale must be very short comparing to the whole AGN duration, so that the stellar mass or black mass accumulated in this period is negligible. This naturally requires such kind of “obscured” objects to be very rare, like local ULIRGs. In fact, we note that in practice the neighbor counts excess is indeed contributed by a very small fraction of objects.

The missing link between [OIII] and companion galaxies may also be because the external gas driving power does not work on small scales (i.e. from torus to accretion disk). This discontinuity could be explained by a simple model of self-regulated black hole growth on small scale. The accretion driven by the inward gravitational torque is balanced by the outward feedback. On small scale, the radiation pressure is relatively high. This regulation may be so strong that the accretion rate of the black hole will be mainly decided by the microphysics of the accretion disk, when the gas supply is sufficient. The driving mechanism is rather internal instead of external. However, the feedback may not dominate on the scale of torus structure, as the numerical model suggests [118]. On larger scale, it can be expected that the feedback impact becomes weaker. The formation of torus is probably more depending on the external factors, like galaxy interactions. If this is the case, one may expect that the link between interaction and star formation is stronger than that between interaction and AGN. Roughly, the neighbor counts excess from IR bright AGNs is weaker than that from typical starburst galaxies [151], consistent with this picture.

Further detailed studies on small scales are necessary to make a clear picture of the link between galaxy interactions and AGN activity. Disentangling the effect of star formation and AGN activity on the galaxy interactions may be essential in this kind of studies.

Chapter 4

AGN Activity and Star Formation at High Redshift

4.1 Introduction

As mentioned in previous chapters, various evidences have shown that there is a close connection between AGN activity and host evolution [142, 85, 92, 244, 166, 104]. The similarity of the overall cosmic star formation history and the black hole accretion density as a function of redshift is also an implication of this kind of connection [159, 160, 109, 152, 37]. Both the brightest quasars and the strongest star forming galaxies are peaking at similar redshift [108]. However, these are indirect evidences. A direct way to verify the existence of this connection is to simultaneously measure the AGN accretion rate and the host/bulge star formation rate individually or by averaging over a well defined AGN population. Since the accumulation of mass is an integration along the cosmic time, and it seems that the active galaxies at different epochs are not the same populations [251, 109], it is necessary to build up the relation not only in present $z = 0$ Universe but also at higher redshifts.

There are already many previous studies trying to establish a clear picture of the AGN-host co-evolution. In local Universe, a tight correlation between AGN activity and host/bulge star formation is found for luminous Seyfert galaxies [182]. From the result of Chapter 3, it seems the galaxy interaction induced gas inflow is indeed responsible for regulating the black hole accretion, hence linking up the host star formation with nuclear activity by common external trigger. However, at higher redshift, such kind of study is limited by observational difficulties. Both the identification of AGN and the measurement of host star formation rate are more complicated than that at low redshift. Although the X-ray identification can help to acquire well defined AGN samples [17], and the host star formation rates can be well estimated from far-IR/sub-mm observations where the AGN contamination is minimized [192, 163, 156], the form of the AGN-host connection is not well constrained due to poor statistics and the strong redshift-luminosity degeneracy in any given AGN sample.

In this chapter, I will describe how we directly estimate the black hole accretion rates

and the star formation rates with some of the most powerful telescopes to date. We establish the relation between AGN activity and host galaxy formation and investigate the evolution of this relation from low to high redshifts.

4.2 Data

We start from AGN samples extracted from high energy maps. X-ray/soft γ -ray photometry is considered as the least biased way to select AGNs [3]. All-sky hard X-ray/soft γ -ray survey, carried by *Swift* BAT [55, 57, 249, 56, 58, 20], detects hundreds of AGNs in local Universe, which are not biased by obscuration. On the other hand, at higher redshifts, deep X-ray survey performed by *Chandra* provides unique opportunity to detect both unobscured and moderately obscured AGNs in a uniform way. GOODS [68] regions are two sky regions, one in north hemisphere (GOODS-N) while the other in south hemisphere (GOODS-S), with extremely deep X-ray observation coverage [40, 208, 2, 155, 265] as well as intensive multi-wavelength coverage.

The far-IR blackbody radiation is a good star formation indicator. In principle, to get a reliable star formation rate, one needs to integrate all the IR radiation to get a total IR luminosity. We notice, however, a measurement around the peak of the SED, i.e. $\nu L_\nu(60\ \mu\text{m})$ is a good approximation. Also the AGN contamination to $60\ \mu\text{m}$ seems negligible [182]. So either in local Universe or at high redshift, we use *rest-frame* $60\ \mu\text{m}$ luminosity as the star formation rate indicator. This of course leads to some uncertainties. I will discuss this later.

4.2.1 Local AGNs

We make our local AGN sample based on 39 months version of the Palermo *Swift* BAT Hard X-ray Catalog [55]. We adopt the identification of the published catalog to remove Galactic objects and non-nuclear hard X-ray sources from the catalog. All the other extragalactic objects are considered as AGNs. Among these AGNs, we exclude radio loud objects by checking their radio counterparts and the SED shape. This is because in case of radio loud, non-thermal, e.g. synchrotron, radiation may contaminate the $60\ \mu\text{m}$ band. We also exclude the objects at low galactic latitude $|b| < 15$, because the IR emission from the Milky Way itself is very strong, which will, in practice, affect the $60\ \mu\text{m}$ flux measurement of the extragalactic source. We limit the analysis at redshift $z < 0.3$, because at higher redshift, the measured $60\ \mu\text{m}$ flux is no longer a probe to rest-frame far-IR emission. We measure the AGN accretion rate by estimating the intrinsic rest-frame 2-10 keV luminosities, which are extrapolated from the observed BAT luminosities, assuming an intrinsic AGN photon index of 1.8.

The $60\ \mu\text{m}$ fluxes are obtained by matching the objects with the *IRAS* Faint Source Catalog [173]. The fluxes of unmatched objects, i.e. non-detections, are measured by fitting model profiles at the optical position of the source. This procedure is done by using online

web toolkit Scanpi¹. The resulting values may be negative due to noise. Hence we stack a large number of objects, detections and non-detections together, to get the estimation of average $60\ \mu\text{m}$ luminosities.

4.2.2 AGNs at High Redshift

At higher redshift, *Swift* BAT is no longer suitable for searching AGNs. The detection rate is too low at redshift ~ 1 for such shallow survey. Instead we use deep X-ray survey in GOODS-N, which is included in the *Chandra* Deep Field North (CDFN). The CDFN 2Ms *Chandra* X-ray catalog [2] provides 503 X-ray sources at sensitivity level of $\sim 2.5 \times 10^{-17}\ \text{erg cm}^{-2}\ \text{s}^{-1}$. 328 of them are located within the *Herschel* PACS image coverage, which will be used to measure rest-frame $60\ \mu\text{m}$ luminosities. At this sensitivity level, the X-ray detections may include a large number of star forming galaxies. In order to remove these objects, we use an updated version of the criterion suggested by F. Bauer et al. [17] to separate star formation dominated objects from AGNs, based on the X-ray luminosity, obscuring gas column density or X-ray hardness ratio, optical spectroscopic classifications and X-ray-to-optical flux ratio. There are totally 224 X-ray selected AGNs in the final sample. Different from local Universe where usually the redshift is available by matching to a nearby NGC galaxy, at higher redshift it is more difficult to get spectroscopic redshifts for a large number of galaxies. Thanks to intensive follow-up observation coverage, 57% of our X-ray AGNs have spectroscopic redshifts (spec-z) [15]. For the other objects, the redshifts are estimated by F. Bauer, using photometric data (phot-z) based on the method suggested by A. Barger et al. [13] (see Figure 4.1). F. Bauer also kindly provides the intrinsic X-ray luminosities $L_{2-10\ \text{keV}}$ and the obscuring column density N_{H} by performing model fitting to the X-ray spectra. The model is an intrinsic simple power-law spectrum absorbed by neutral gas with variable column density at the redshift of the object, as well as absorbed by Galactic neutral gas at redshift 0 with fixed column density of $1.6 \times 10^{20}\ \text{cm}^{-2}$. The photon index is allowed to vary for objects above 150 net counts in the 0.5–8 keV band, and is fixed to 1.85 for objects below 150 net counts. This is because the degeneracy between photon index and column density to the X-ray spectrum is not easy to break when the photon counts are too low.

The rest-frame $60\ \mu\text{m}$ fluxes are estimated by using *Herschel* PACS (see Section 1.3.6) image. We use the v2.2 100 and $160\ \mu\text{m}$ images of GOODS-N field [28], corresponding to the rest-frame $60\ \mu\text{m}$ at redshift ~ 1 . We match the X-ray AGNs to the PACS catalog, which is extracted based on the *Spitzer* IRAC/MIPS $24\ \mu\text{m}$ detections as priors [161, 28, 162], to a 3σ depth of $\sim 3.0\ \text{mJy}$ at $100\ \mu\text{m}$ and $\sim 5.7\ \text{mJy}$ at $160\ \mu\text{m}$, respectively. In cases that the *Chandra* sources are not detected at $24\ \mu\text{m}$ we compare them to a blind catalog extracted from the PACS images without position priors [28], to make sure that we do not miss any PACS detections simply due to the lack of $24\ \mu\text{m}$ detection. Only 21% of the X-ray AGNs are detected by PACS. For the non-detections, we stack the PACS residual map, which is obtained by subtracting the detected PACS sources from the original PACS map, on

¹<http://scanpi.ipac.caltech.edu:9000/applications/Scanpi/index.html>

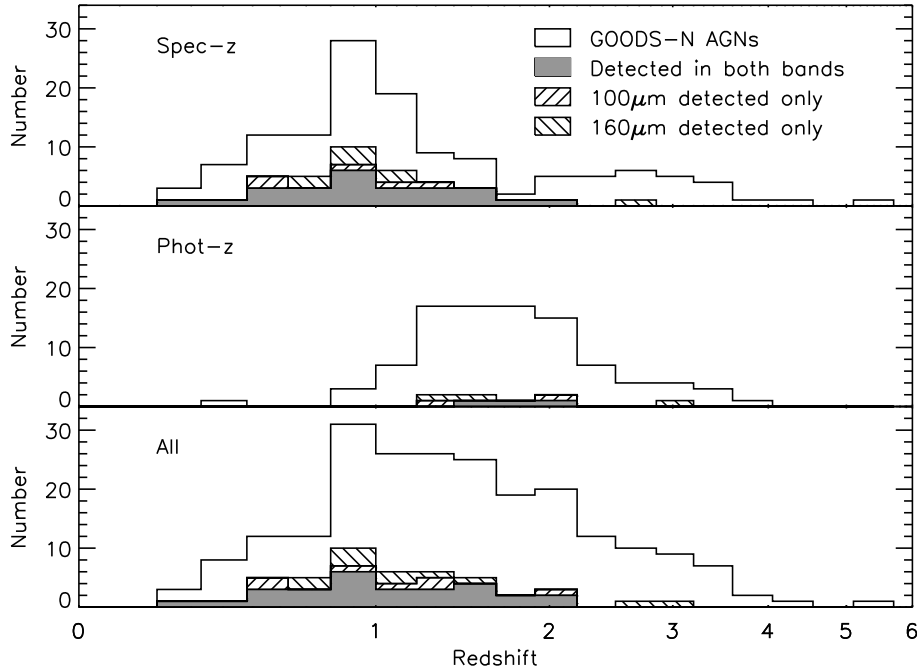


Figure 4.1: Redshift distribution of the 224 GOODS-N X-ray AGNs in the region with good PACS coverage. 46 of them are individually detected in at least one of the PACS bands.

the position of X-ray AGNs, with the stacking library developed by M. Bethermin et al. [30]. Since the K-correction is strong for PACS fluxes in the redshift range of $0 < z < 3$, for each stack we restrict the stacked objects in a relatively narrow redshift bin with $\Delta z / (1 + z) < 0.4$ ($0.2 < z < 0.8$, $0.8 < z < 1.4$ and $1.4 < z < 2.5$). In order to minimize the necessary assumption, we compute the rest-frame $60 \mu\text{m}$ luminosities simply using the detection wavelength closer to rest-frame $60 \mu\text{m}$ or log-linearly interpolating for detections in both PACS bands at $0.67 < z < 1.67$. We drop the objects at very high redshifts ($z > 2.5$) where the PACS bands are no longer able to measure the far-IR emission related with star formation.

4.3 Results

4.3.1 Far-IR Luminosity as a Function of Redshift

Our high redshift sample is built up in a way that both the AGN selection and the star formation rate estimation are done uniformly at any redshifts. It covers a large redshift range, allowing a study of star formation in AGN hosts at different cosmic time. Figure 4.2 shows that the rest-frame $60 \mu\text{m}$ luminosities in AGN hosts increase with redshift. The increase for PACS detections can be interpreted as a selection effect that only brighter objects are observed at higher redshift. However, as we also see the increase in the stacked

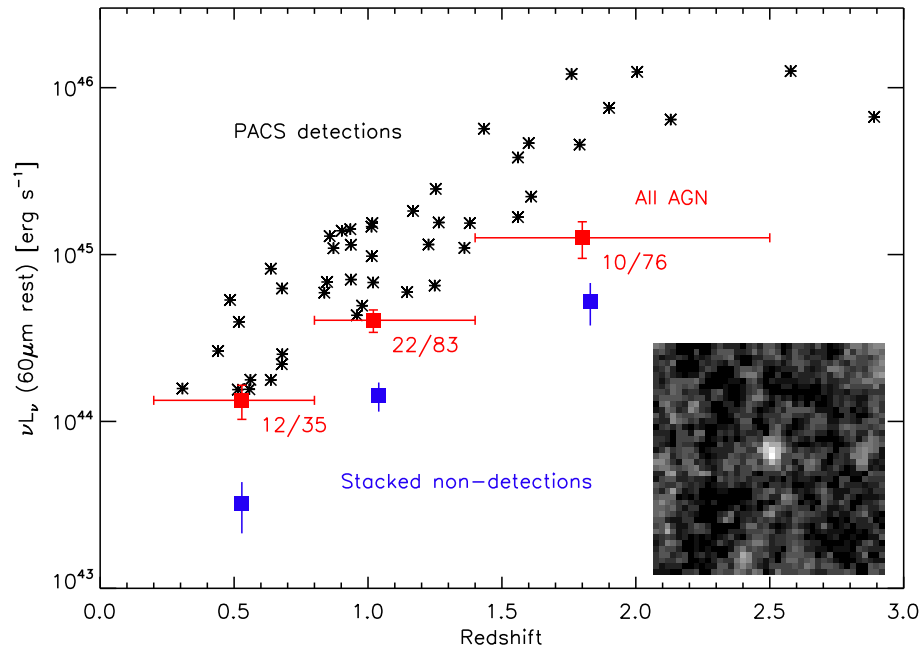


Figure 4.2: Rest-frame $60\ \mu\text{m}$ luminosities of GOODS-N X-ray AGNs as a function of redshift. The black stars are individually PACS detected objects. The blue symbols are the stacked non-detections. The red symbols are the average of detections and non-detections. The uncertainty is derived by bootstrapping within the sample bin. The number of detections and total number of objects in each bin is indicated. The bottom-right inserted image shows the stack for the individually undetected objects in redshift bin $0.8 < z < 1.4$.

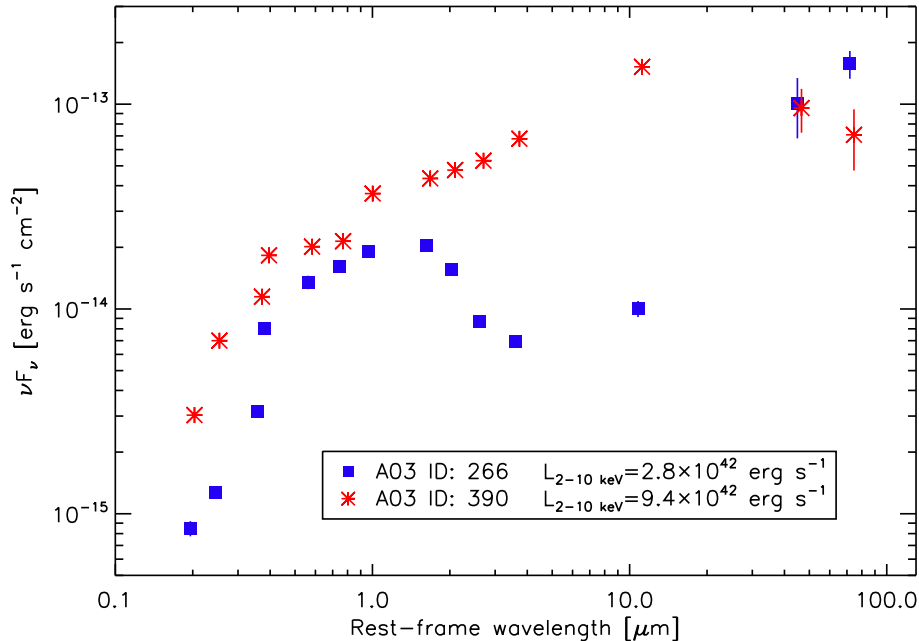


Figure 4.3: Two examples of optical to far-IR SEDs of $z \sim 1.2$ AGNs. ID 390 [2] is dominated by AGN continuum over the whole spectral range, while ID 266 is an obscured AGN dominated by an optical/near-IR stellar bump and a far-IR peak.

non-detections, and in the combined sample of all detections and non-detections, it is unlikely that the trend is simply driven by the far-IR flux limit. Here we note that although the non-detections are not detected individually, the stacks usually show detectable signal in the center (see the inserted stack image on the bottom-right corner of Figure 4.2 as an example). The photometric error is negligible comparing to the variation in the underlying population, hence the uncertainty of the average value is estimated by bootstrapping within the specific sample.

The mean fluxes for the detected sources and stacked mean values differ by around an order of magnitude, in any of the redshift bins. This large difference implies a wide intrinsic distribution of the far-IR luminosities of AGN hosts. If we assume the far-IR luminosities follow a log-normal distribution, then the ratio of detection mean value to the stacked non-detection mean value, as well as the $\sim 20\%$ detection rate, is consistent with an intrinsic dispersion of about 0.5 dex in each bin. Though the detailed distribution is not well constrained, it is wide for sure. Hence the typical (median) flux must be lower by a factor of ~ 2 for the log-normal distribution. This kind of variety can also be observed in mid-IR as well as the mid- to far-IR SED shape (see Figure 4.3).

However, there is another possible degeneracy that the increase of host far-IR emission with redshift is influenced by the increase of the AGN luminosity with redshift. This is, somehow, inevitable because the AGN sample itself is an X-ray flux limited sample. In order to break the degeneracy, we further bin the AGN sample into 3×4 grid bins, by redshift ($0.2 < z < 0.8$, $0.8 < z < 1.4$ and $1.4 < z < 2.5$) and by intrinsic X-

z	$L_{2-10\text{keV}}$ erg s^{-1}	N_{det}/N	Detected $\nu L_{\nu}(60\ \mu\text{m rest})$	Stack	All $10^{44}\ \text{erg s}^{-1}$
0.2–0.8	all	12/35	3.3	0.32	1.33 ± 0.31
0.8–1.4	all	22/83	11.3	1.43	4.04 ± 0.62
1.4–2.5	all	10/76	61.1	5.27	12.61 ± 3.12
0.2–0.8	$< 10^{42}$	4/16	1.9	0.09	0.55 ± 0.23
0.8–1.4	$< 10^{42}$	1/9	6.9	1.40	2.01 ± 0.91
1.4–2.5	$< 10^{42}$	0/1		3.92	
0.2–0.8	10^{42-43}	2/12	4.4	0.60	1.23 ± 0.51
0.8–1.4	10^{42-43}	7/37	12.3	1.56	3.60 ± 0.73
1.4–2.5	10^{42-43}	6/18	63.4	4.35	24.04 ± 8.45
0.2–0.8	10^{43-44}	6/7	3.8	1.91	3.54 ± 0.89
0.8–1.4	10^{43-44}	13/32	10.5	1.61	5.22 ± 1.11
1.4–2.5	10^{43-44}	3/51	69.3	5.30	9.06 ± 2.80
0.2–0.8	$> 10^{44}$	0/0			
0.8–1.4	$> 10^{44}$	1/5	18.2	2.32	5.50 ± 3.56
1.4–2.5	$> 10^{44}$	1/6	22.2	8.58	10.85 ± 4.77
z	N_{H} cm^{-2}	N_{det}/N	Detected $\nu L_{\nu}(60\ \mu\text{m rest})$	Stack	All $10^{44}\ \text{erg s}^{-1}$
0.8–1.4	$< 10^{22}$	2/10	13.7	1.12	4.15 ± 1.25
0.8–1.4	10^{22-23}	6/25	11.6	1.47	3.89 ± 0.91
0.8–1.4	10^{23-24}	10/28	9.6	1.76	4.57 ± 0.89
0.8–1.4	$> 10^{24}$	0/5		1.67	1.67 ± 0.88

Table 4.1: Average far-IR luminosities of different AGN subsamples. The far-IR luminosities are given separately for the individual $> 3\sigma$ detections, the stack of the non-detections, and the number-weighted average for all sources. Errors for luminosities are standard deviations from bootstrapping and are dominated by the dispersion of the AGN population rather than measurement error.

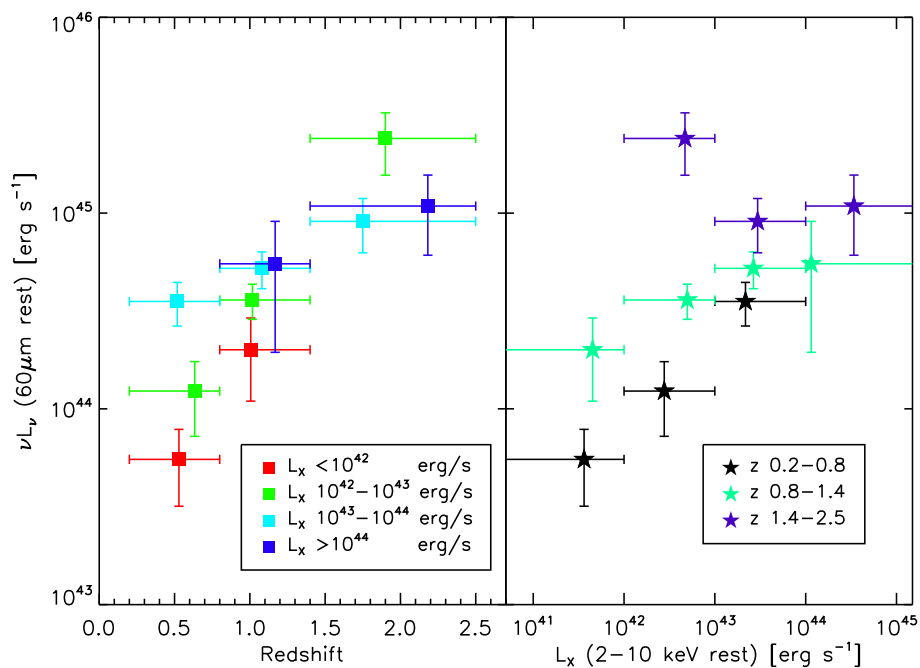


Figure 4.4: Left panel: far-IR luminosity as a function of redshift, for different bins in intrinsic rest frame 2–10 keV X-ray luminosity. The errors are based on bootstrapping within the specific sample. Right panel: far-IR luminosity as a function of intrinsic hard X-ray luminosity, for different redshift bins.

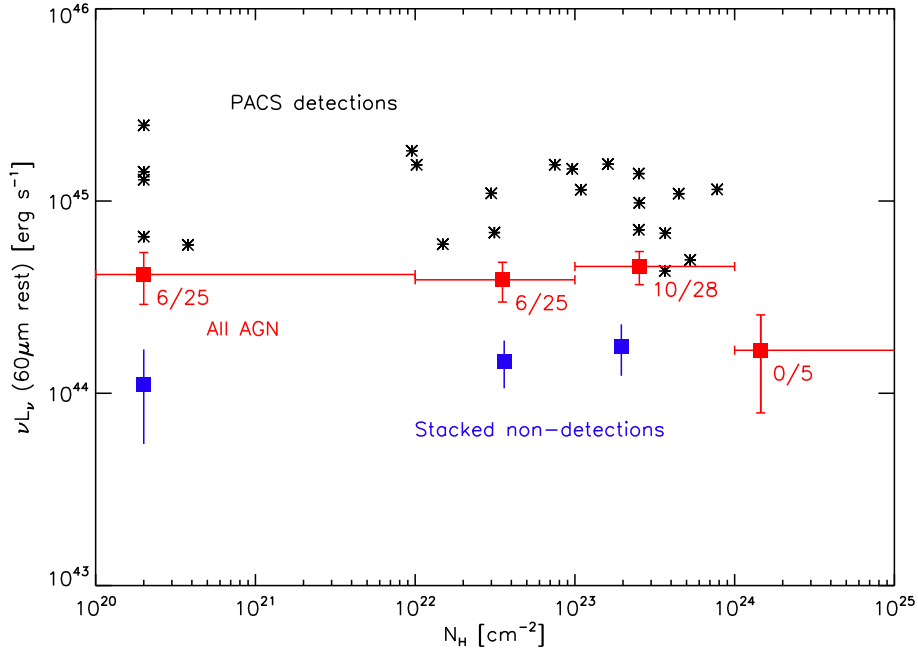


Figure 4.5: Far-IR luminosity as a function of X-ray column density for AGNs at redshift $0.8 < z < 1.4$. Low obscuration objects are placed at $2 \times 10^{20} \text{ cm}^{-2}$. Symbols are the same as Figure 4.2.

ray luminosity $L_{2-10 \text{ keV}}$ ($L_{2-10 \text{ keV}} < 10^{42} \text{ erg s}^{-1}$, $10^{42} \text{ erg s}^{-1} < L_{2-10 \text{ keV}} < 10^{43} \text{ erg s}^{-1}$, $10^{43} \text{ erg s}^{-1} < L_{2-10 \text{ keV}} < 10^{44} \text{ erg s}^{-1}$ and $L_{2-10 \text{ keV}} > 10^{44} \text{ erg s}^{-1}$). Table 4.1 shows host far-IR luminosities for these bins. In the following discussions we discard the bins with less than 5 objects and correspondingly large errors. In Figure 4.4 we display the stacking results of the grid subsamples in two different ways. In the left panel, we show that the increase of the host far-IR luminosity with redshift is preserved when considering AGN luminosity bins separately. In any specific X-ray luminosity bin, the increase of average IR luminosity with redshift is statistically significant, especially in low X-ray luminosity bins. For example, if focusing on the AGNs with $10^{42} \text{ erg s}^{-1} < L_{2-10 \text{ keV}} < 10^{43} \text{ erg s}^{-1}$, there is no overlap in the 99% confidence intervals of far-IR luminosity when comparing the $0.2 < z < 0.8$ and $1.4 < z < 2.5$ bins ($< 2.8 \times 10^{44} \text{ erg s}^{-1}$ and $> 6.1 \times 10^{44} \text{ erg s}^{-1}$). On the contrary, although the X-ray luminosity is strongly correlated with far-IR luminosity at low redshift $0.2 < z < 0.8$, the increase trend flattens at intermediate redshift and disappears in the highest redshift $1.4 < z < 2.5$ bin.

4.3.2 Far-IR Luminosity as a Function of X-ray Obscuration

In the X-ray luminosity range covered by our sample, there is no significant trend of far-IR luminosity with X-ray column density, as shown in Figure 4.5. This is also valid when considering detections and non-detections separately. We note that the analysis is limited by the statistics at very high column density $N_{\text{H}} > 10^{24} \text{ cm}^{-2}$ (totally 5 objects without

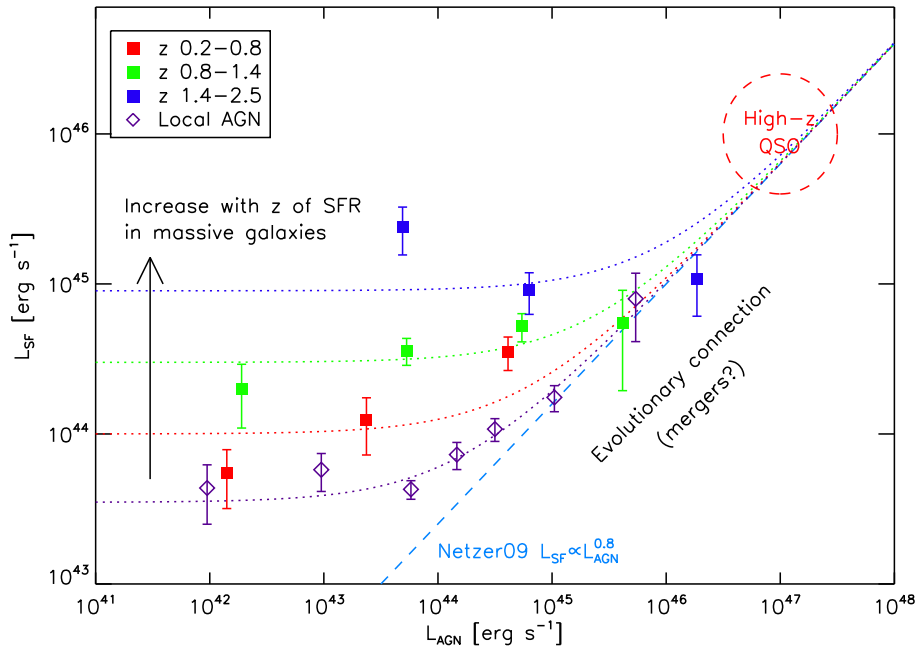


Figure 4.6: The host star formation rate against AGN luminosity. The red, green and blue solid squares are the results from *Chandra*-PACS AGN sample in the GOODS-N field for different redshifts. The magenta empty diamonds are BAT-*IRAS* AGN sample for local AGNs with $z < 0.3$. The dotted lines are not fitting to the data but rather to show how we interpret the data. The cyan dashed line shows the correlation in high luminosity regime, with the slope taken from local Seyferts result.

PACS detections). It may be due to the intrinsically rarity of such kind of objects or the limitation of 2–10 keV X-ray surveys that highly obscured objects are still missing from deep X-ray survey.

4.4 Discussion

Given the excellent sensitivity of *Herschel* PACS to the rest-frame far-IR emission in the hosts of X-ray selected AGN at redshift of $0.2 < z < 2.5$, we successfully establish the relation between AGN X-ray luminosity and host far-IR luminosity at various redshifts, by breaking up the strong degeneracy between redshift and luminosity which strongly affects the previous submm-based studies of AGN host star formation [83, 218, 14, 192, 258, 163, 156]. We make the minimal assumption to the IR SED shape to estimate the star formation rate by taking the rest-frame $60 \mu\text{m}$ luminosity as a direct indicator.

A variety of studies have already established a local correlation between AGN luminosity and star forming luminosity, in the luminosity regime of bright Seyferts and quasars [209, 182, 181]. The high redshift quasars extend this relation to higher luminosities [217, 157]. We overplot our results on the AGN versus star formation plane as in Figure 4.6. By

combining with local ($z < 0.3$) *Swift* BAT sample (magenta diamonds), we are able to cover a larger redshift range and better understand the star formation-AGN relation for AGNs with X-ray luminosity of $10^{42} \text{ erg s}^{-1} \lesssim L_{2-10\text{keV}} \lesssim 10^{46} \text{ erg s}^{-1}$. We also convert the X-ray luminosity into AGN bolometric luminosity L_{AGN} with empirical bolometric calibrations. The $L_{2-10\text{keV}}$ is first converted into monochromatic luminosity of AGN continuum at 5100 \AA L_{5100} [164], and then scaled up by a bolometric correction factor of ~ 7 .

In high luminosity regime, our data follow the Seyfert-quasar track (the blue dashed line, the log-linear relation obtained by H. Netzer [181]) very well. This suggests bright AGNs are connected with host star formation by some common mechanism, probably galaxy-galaxy merger/interactions [119], as implied in Chapter 3. However, for low luminosity AGNs, their host star formation rates seem to deviate from that correlation. The independence between host star formation rate and AGN luminosity implies a secular evolution path, that the host stellar mass growth is not coupled with supermassive black hole activity at a spatial scale of the whole galaxy, though they may still correlated with each other at smaller scale. The dotted lines in Figure 4.6 are combination of a redshift independent log-linear correlation component and a redshift dependent constant component. They are not real fitting but guide lines to the data, showing how the results are explained. The constant component at redshift 0 is at a level of $\sim 4 \times 10^{43} \text{ erg s}^{-1}$. The constant value scales up by a factor of ~ 3 , ~ 7.5 , ~ 20 , at redshift ~ 0.5 , ~ 1 and ~ 2 , respectively. Although the accurate values are not well constrained only by our data with current statistics, the trend is consistent with a study of star formation rate of normal star forming galaxies, parametrized as a function of stellar mass and redshift by N. Bouché et al. [35]. This elevated “constant” star formation is also consistent with the increase of typical star formation rate of normal massive galaxies with redshift [186, 72, 61]. As a natural consequence, the AGN luminosity of the upturn point increases with redshift. At redshift 0, the host star formation is already coupled with nuclear activity for moderately luminous ($10^{44} \text{ erg s}^{-1}$) AGNs, while at redshift ~ 2 only the brightest AGNs with luminosity higher than $10^{46} \text{ erg s}^{-1}$ are affected. On the other hand, the increase of host star formation rate with redshift can only be observed in low AGN luminosity regime. In a study based on *Spitzer* $70 \mu\text{m}$ data, J.R. Mullaney et al. [175] find that the far-IR to X-ray ratio increases with redshift for AGNs with $L_X = 10^{42}-10^{43} \text{ erg s}^{-1}$ while the ratio remains unchanged at higher AGN luminosity. This is consistent with our work and easy to understand by using the two-path interpretation presented here.

The existence of such horizontal branch seems inconsistent with the tight correlation between black hole mass and host bulge mass [166, 107]. However, it could be explained by a time delay between the host star formation and AGN activity. They occur at very different spatial scales and the time for gas travelling from galaxy outer region to the central black hole may be as long as $\sim 100 \text{ Myr}$, comparable to the lifetime of AGN activity [168, 121]. The increase of the “constant” star formation rate may be simply due to the increase of typical galaxy gas fraction with redshift [94, 86, 60, 237, 91, 50, 238, 18] and increased gas disturbance which can drives the cold gas inward [86, 76, 54, 237]. It also worths to mention again that the black hole accretion itself may also have two different modes [126], roughly corresponding to low and high luminosity AGNs here, though this is

originally expressed in term of Eddington ratio. Many low luminosity AGNs are found to be fed by the hot gas from stellar mass loss of evolved stars due to lack of feeding cold gas. Their AGN activity is not necessarily correlated with host star formation which occurs at much larger scale.

Previous similar study based on *SDSS* AGN sample fails to find such horizontal branch [181]. In order to get further insights about this problem we make directly comparison between the results from the X-ray selected AGN sample and the *SDSS* optical AGN sample in Figure 4.7. The bolometric correction of [OIII] luminosities is ~ 500 , calibrated using *SDSS* quasars with good measurement of [OIII] line and the Balmer decrement. The star formation rate within fiber is estimated with 4000 Å break and the stellar mass of the host galaxy [41]. Then a fiber correction is applied to obtain the total star formation rate², which is comparable to the results shown in Figure 4.6. The star formation 60 μm luminosities, are then calculated from the empirical $L_{\text{IR}}\text{--SFR}$ relation [52, 116].

From the grey contour, it seems that the correlation between AGN luminosity and star formation rate is significant over the whole luminosity range, and the optical AGNs deviate from the X-ray results. However, the deviation only occurs in the low luminosity regime, and it is known that at low luminosity the optical classifications will miss AGNs due to host star formation contamination in the fiber aperture with fixed angular size. As mentioned in Section 2.2, the weak optical AGNs (black dots) are strongly biased while the strong optical AGNs (the red dots) are scarcely affected. Interestingly, the deviation starts to occur at the boundary luminosity $L[\text{OIII}] \sim 10^7 L_{\odot}$, implying that the inconsistency is probably due to the selection effect in optical sample. And indeed, for strong optical AGNs, the optical result follows the similar trend as the X-ray one. The gradually flattening of the AGN-SF relation with decreasing AGN luminosity is observed in strong optical AGNs too, by using our stellar mass complete sample. The strong/weak AGN separation interrupts this trend at $L_{\text{AGN}} \sim 10^{43} \text{ erg s}^{-1}$. This probably explains why the horizontal branch is not revealed in previous optical studies: *SDSS* optical AGN classification is only complete at ($L[\text{OIII}] \gtrsim 10^7 L_{\odot}$, i.e. $L_{\text{AGN}} \gtrsim 3 \times 10^{43} \text{ erg s}^{-1}$), but at this AGN luminosity level the horizontal component is no longer dominant. However, we must emphasize, with current *SDSS* analysis, it is not possible to make strong constrain to the horizontal branch.

The star formation rate offset between X-ray and optical results (magenta dotted curve and green dashed curve) is not quantitatively determined. First, both curves are not real fitting to the data. Second, the horizontal branch is not well constrained with *SDSS* strong AGNs. Third, the different redshift ranges of the X-ray and optical samples ($z < 0.3$ versus $0.02 < z < 0.21$) may cause some intrinsic offset. Hence we are not able to directly compare the star formation rates of X-ray AGNs with that of optical AGNs. But we note that in the same *SDSS* stellar mass complete sample, the strong AGNs clearly have higher host star formation rates than the field galaxies, even at $L[\text{OIII}] \sim 10^7 L_{\odot}$, where the proposed horizontal branch starts to dominate. That probably implies the cold gas supply is important to trigger AGNs, no matter which evolution mode the hosts are in. This also implies that the star formation level of the proposed horizontal branch may not

²<http://www.mpa-garching.mpg.de/SDSS/DR7/sfrs.html>

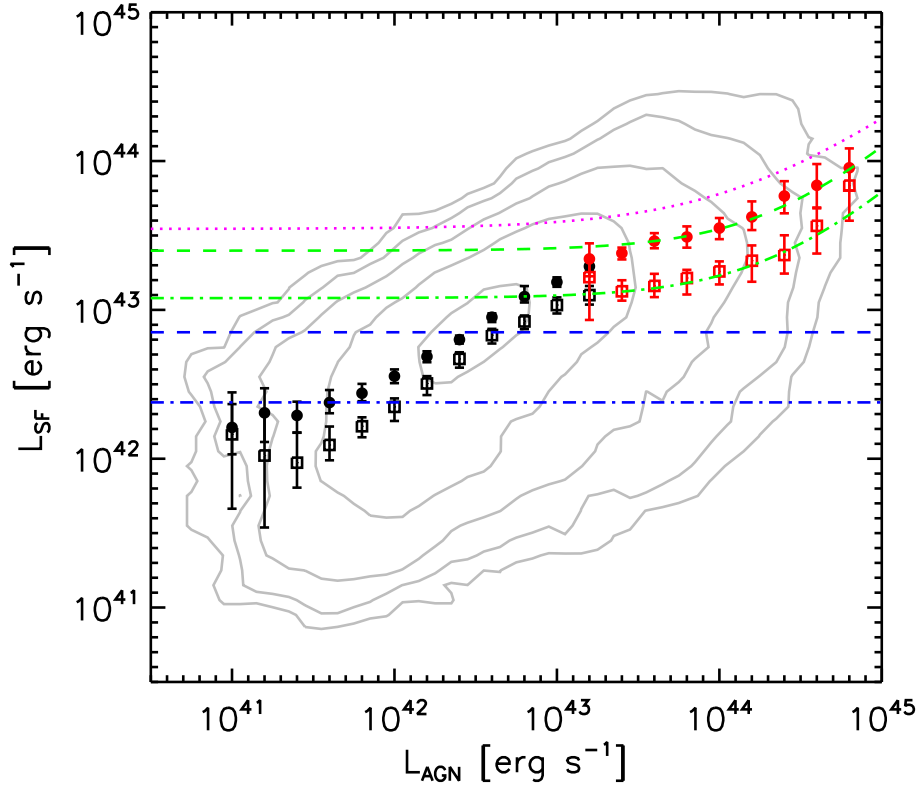


Figure 4.7: The host star formation rate against AGN luminosity for *SDSS* optical AGNs, similar to Figure 4.6. The grey contour is the distribution of local AGNs in sample S1 (see also Section 2.2). The solid circles and open squares are volume-weighted mean and median values of host star formation rates in each AGN luminosity bins. The black and red data points are for weak ($L[\text{OIII}] < 10^7 L_{\odot}$) and strong AGNs ($L[\text{OIII}] > 10^7 L_{\odot}$) respectively. The magenta dotted line is identical to the one in Figure 4.6, showing mean star formation rates of the BAT-*IRAS* AGNs. The green dashed and dot-dashed lines are slightly modified curves to show the trend of *SDSS* strong AGN sample, corresponding to the mean and median values respectively. They are not quantitative fittings, but only show our interpretation to the data. The blue dashed and dot-dashed lines are the mean and median values of star formation rates of field galaxies, with redshift of $0.02 < z < 0.21$ and stellar mass of $9.8 < \log(M_*/M_{\odot}) < 11.8$.

exactly the same as the star formation level of normal galaxies at any given redshift. And it is especially important when comparing our result to other high redshift observations because at high redshift usually it is impossible to observe red sequence galaxies.

Another interesting result is the lack of correlation between host star formation and X-ray column density. In major merger-driven scenario, which invokes an evolution sequence of starburst galaxy - obscured AGN - unobscured AGN [212, 119], the obscured AGNs are expected to be hosted by starburst galaxies while the star formation in unobscured AGN hosts is quenched by the strong feedback. There are evidences that high luminosity quasars are consistent with this picture [192, 191, 234]. However, for our moderately luminous AGNs, the merger scenario seems no longer valid. It is also consistent with our interpretation that the majority of our GOODS-N AGNs are located on the horizontal branch on the $L_{\text{SF}}-L_{\text{AGN}}$ diagram, i.e. their AGN activities are not coupled with host star formation so that they are unlikely major merger driven objects. On the other hand, the result is consistent with the AGN unification model prediction, that the observed obscuration purely depends on the viewing angle: for an unbiased AGN sample, the host star formation have no impact to the observed X-ray column density.

A limitation of this study is that the small $\sim 11' \times 16'$ field restricts the number of high luminosity ($L_{2-10\text{keV}} > 10^{44} \text{ erg s}^{-1}$) AGNs. In a follow-up study with more *Herschel*-PACS observations in larger field COSMOS, Rosario et al. [207] find similar results as we do here, except that the enhancement of star formation rate in luminous AGNs weakens or disappears at high redshift ($z > 1$). This may imply that the coupling of AGN activity and host star formation mainly happens in low redshift $z < 1$ and high luminosity regime $L_{2-10\text{keV}} > 10^{43} \text{ erg s}^{-1}$.

Another caveat for this study is that the 2–10 keV survey may miss the Compton-thick AGNs [97, 243]. Using harder X-ray bands can solve this problem. However, current hard X-ray facilities are not capable to detect large sample of high redshift AGNs. Another possible solution is to use other AGN identification methods capable to detect Compton-thick objects, like IR selection [193, 170, 99]. Though, as we have shown in Chapter 2, the mid-IR color selections are not useful to discover low luminosity AGNs, it may help to better understand the AGN-host connection for unbiased luminous AGNs at high redshift.

Chapter 5

Summary and Prospective

This thesis tries to build up the AGN-host connection, which is one of key issues to better understand the galaxy formation, and hence the whole evolution picture of the observable Universe. From Chapter 2 to 4, the study covers the AGNs from low to high redshifts, giving a good census of their host galaxies in the period that both the AGN and the star formation are the most active throughout the whole cosmic time.

In local Universe, the combination of optical and IR surveys, i.e. *SDSS* and *WISE*, gives a sample of ~ 30000 optically selected AGNs with multi-band photometric and optical spectral information. Besides the [OIII] line luminosities commonly used in previous works, mid-IR luminosities are also used to estimate the black hole accretion rate. Due to the heavy host galaxy contamination in the mid-IR bands, the nuclear IR emission is obtained in a statistical way. It is found that the mid-IR host component is mainly determined by the host stellar mass and the star formation rate. To avoid AGN contamination to the measurement of the star formation, $D_n(4000)$ is used instead of emission lines like $H\alpha$. Then the host component in each AGN is estimated from normal galaxies with similar host stellar masses and star formation rates. The resulting mid-IR luminosities from torus are in good correlation with well studied [OIII] luminosities for type 2 Seyfert galaxies. This correlation is further expanded to a total range of 4 order of magnitude by adding local *SDSS* quasars into the study. Using this new IR AGN activity indicator, it is confirmed that a major fraction of the total AGN radiation output comes from the galaxies with young stellar population ($D_n(4000) < 1.6$) and intermediate concentrations ($R_{90}/R_{50} = 2.2\text{--}3.0$). This is consistent with previous studies, suggesting a tight AGN-host star formation connection at $z \sim 0$. A direct comparison between the AGN luminosity and the host star formation rate also supports the existence of the connection. The AGN hosts tend to have higher average star formation rates than normal galaxies with the same stellar masses. Unfortunately, due to strong selection bias in low AGN luminosity regime ($L[\text{OIII}] < 10^7 L_\odot$), the picture is not well clarified.

The [OIII] and IR emissivity distributions are very similar for Seyfert galaxies, supporting the validity of the standard AGN unification model. The torus is a common feature, and the Seyferts selected both in IR and optical are representative to the same AGN population. Another important AGN population, LINERs, are also investigated in the same

way. A sub-population of IR-bright LINERs are consistent with Seyfert galaxies. However, due to the relatively low IR nuclear emission detection rate, the result is inconclusive for the whole LINER population.

This multi-wavelength approach is further applied to the study of AGN environments. The key question, why the AGNs and host galaxies are connected, could be partly answered by investigating the galaxy-galaxy interactions. The external driving of cold gas by merger/interaction, is one of the acknowledged mechanisms to explain the strong coupling of AGN activity and host star formation. It is found in a study of close companions that the AGN IR emission is somehow related with interactions while the [OIII] luminosities are not. The interaction-obscured AGN-unobscured AGN sequence within the merger framework can explain the results, though the timescale of the obscured stage must be very short comparing to the whole AGN duration. It is also possible that the AGN feedback is regulating the inner region of the accretion system, from torus to accretion disk. The importance of the merger in the triggering of local AGNs is not clear yet. Further detailed studies could be carried to solve this problem.

In addition to the optical/IR AGN sample, local hard X-ray survey provides a relatively smaller AGN sample but in principle unbiased by intrinsic obscuration. Though without detailed spectral information, using all sky far-IR surveys helps to determine the star formation rates in these AGN host galaxies. It is shown that the host star formation rates are well linked with AGN luminosities for high luminosity AGNs while the link disappears for low luminosity AGNs. It is probably that there are two modes of AGN host evolution: co-evolution branch where the host star formation and AGN activity are coupled, and horizontal branch (secular evolution) where the host star formation is irrelevant to the nuclear activity. For the former branch, some mechanisms must regulate the co-evolution: e.g. common gas inflow processes, merger driven accretion, etc. For the latter one, it is possible that there is a time lag between gas accretion onto the host galaxy and onto the black hole. Unfortunately, the horizontal branch is not well constrained due to technical limitations and low statistics. In spite of the flattening trend of $L_{\text{SF}}-L_{\text{AGN}}$ relation with decreasing luminosity, the *SDSS* AGN sample also fails to give a solid conclusion for the horizontal branch. The study of low luminosity AGNs in an unbiased way is a key to make better insights of that.

The study of measuring AGN host star formation rate is extended into higher redshifts, with deeper *Chandra* X-ray data and *Herschel* PACS images. Comparing with local AGNs, the AGN host star formation rates are elevated, consistent with current high redshift observations showing the increasing star formation level of normal galaxies with redshift. And this seems to weaken the AGN-host connection at high redshift. The horizontal branch (if exist) appears to dominate the whole AGN luminosity range in the study at $z \sim 2$. Studies directly comparing the low and high redshift AGN host galaxies should be aware of this potential bias.

There are still many open questions on the AGN-host co-evolution. For example, the mechanism responsible for the AGN-host co-evolution is still not fully understood. The mild interaction can cause the activities of moderately luminous AGNs, then how about violent mergers? Is the minor merger and interactions sufficient to explain the whole co-

evolution branch? Is it necessary to introduce major merger to explain the triggering of more luminous AGNs, like quasars? These questions are not yet answered in this thesis. Instead of clustering studies conducted in this thesis, morphological studies searching for disturbed AGN hosts may help to understand the role of mergers in the AGN-host co-evolution. Based on previous parameterized morphological studies [154], it seems possible to systematically investigate the morphology properties of local galaxies and try to find the link between AGN, host star formation and the strength of disturbance. It could be extended to higher redshifts [32] where the merger rates are probably higher, though the identification of AGNs will be more complicated. In case of high luminosity AGNs, a tricky technique to subtract the nuclear emission from images may be needed to study the host galaxies.

The current picture of cold gas inflow triggered AGN also needs to be refined. If a time lag between host star formation and observed AGN activity is important, then it should be reflected on the star formation history of AGN host galaxies. Fitting the spectra of host galaxies with stellar synthesis models may show distinguishable features for different types of AGN-star formation time delay. Using multi-wavelength data is important, as the observed time delay can be affected by many other factors, such as obscuration of nuclear activity. The environmental difference between IR and optically selected AGNs, could be further explored by comparing the star formation history of them. This will also be helpful to understand the torus structure, which may be a gas reservoir for further gas accretion and hence important in the process of feeding gas onto the accretion disk.

The low luminosity AGN is another issue. Till now there is no unbiased AGN study in the low luminosity regime due to technical difficulties. Currently the most promising method is to use hard X-ray observatories and to push the detection limit to lower luminosities with much longer exposure time. This may be achieved in near future with updated hard X-ray catalogs. And it will be interesting to re-visit the $L_{\text{SF}}-L_{\text{AGN}}$ diagram then.

The star formation measurement is another important issue in the study of AGN-host connection. Deep X-ray and far-IR data are expansive and limited to small samples. Instead, public survey data covering large sample of galaxies could be used for this purpose. The SED decomposition technique can be used to measure the AGN luminosity and the host star formation rate simultaneously. And indeed, this has been accomplished with small samples [174]. With larger sample, the observed AGN-host connection could be revisited in more details with better statistics. The triggering mechanism of AGNs on the horizontal branch, and its relation with the stellar wind mode of AGN accretion, could be of interest.

Bibliography

- [1] M.A. Abramowicz, B. Czerny, J.P. Lasota und E. Szuszkiewicz, *ApJ* **332** (1988), 646.
- [2] D.M. Alexander, F.E. Bauer, W.N. Brandt, D.P. Schneider, A.E. Hornschemeier, C. Vignali, A.J. Barger, P.S. Broos, L.L. Cowie, G.P. Garmire, L.K. Townsley, M.W. Bautz, G. Chartas und W.L.W. Sargent, *AJ* **126** (2003), 539.
- [3] D.M. Alexander und R.C. Hickox, *New A Rev.* **56** (2012), 93.
- [4] O. Almaini, B.J. Boyle, R.E. Griffiths, T. Shanks, G.C. Stewart und I. Georgantopoulos, *MNRAS* **277** (1995), L31.
- [5] M.S. Alonso, D.G. Lambas, P. Tissera und G. Coldwell, *MNRAS* **375** (2007), 1017.
- [6] A. Alonso-Herrero, P.G. Pérez-González, D.M. Alexander, G.H. Rieke, D. Rigopoulou, E. Le Flo'ch, P. Barmby, C. Papovich, J.R. Rigby, F.E. Bauer, W.N. Brandt, E. Egami, S.P. Willner, H. Dole und J.S. Huang, *ApJ* **640** (2006), 167.
- [7] R.R.J. Antonucci und J.S. Miller, *ApJ* **297** (1985), 621.
- [8] R.J. Assef, C.S. Kochanek, M. Brodwin, R. Cool, W. Forman, A.H. Gonzalez, R.C. Hickox, C. Jones, E. Le Flo'ch, J. Moustakas, S.S. Murray und D. Stern, *ApJ* **713** (2010), 970.
- [9] R.J. Assef, D. Stern, C.S. Kochanek, A.W. Blain, M. Brodwin, M.J.I. Brown, E. Donoso, P.R.M. Eisenhardt, B.T. Jannuzi, T.H. Jarrett, S.A. Stanford, C.W. Tsai, J. Wu und L. Yan, *ApJ* **772** (2013), 26.
- [10] H. Awaki, H. Kunieda, Y. Tawara und K. Koyama, *PASJ* **43** (1991), L37.
- [11] J.A. Baldwin, *ApJ* **214** (1977), 679.
- [12] J.A. Baldwin, M.M. Phillips und R. Terlevich, *PASP* **93** (1981), 5.
- [13] A.J. Barger, L.L. Cowie, P. Capak, D.M. Alexander, F.E. Bauer, E. Fernandez, W.N. Brandt, G.P. Garmire und A.E. Hornschemeier, *AJ* **126** (2003), 632.

- [14] A.J. Barger, L.L. Cowie, A.T. Steffen, A.E. Hornschemeier, W.N. Brandt und G.P. Garmire, *ApJ* **560** (2001), L23.
- [15] A.J. Barger, L.L. Cowie und W.H. Wang, *ApJ* **689** (2008), 687.
- [16] S.D. Barthelmy: *Burst Alert Telescope (BAT) on the Swift MIDEX mission. Burst Alert Telescope (BAT) on the Swift MIDEX mission*, In *Society of Photo-Optical Instrumentation Engineers (SPIE) Conference Series*, herausgegeben von K. A. Flanagan und O. H. W. Siegmund, Band 5165 von *Society of Photo-Optical Instrumentation Engineers (SPIE) Conference Series*. (Februar 2004) Seiten 175–189.
- [17] F.E. Bauer, D.M. Alexander, W.N. Brandt, D.P. Schneider, E. Treister, A.E. Hornschemeier und G.P. Garmire, *AJ* **128** (2004), 2048.
- [18] A. Bauermeister, L. Blitz, A. Bolatto, M. Bureau, A. Leroy, E. Ostriker, P. Teuben, T. Wong und M. Wright, *ApJ* **768** (2013), 132.
- [19] S.A. Baum, J.F. Gallimore, C.P. O’Dea, C.L. Buchanan, J. Noel-Storr, D.J. Axon, A. Robinson, M. Elitzur, M. Dorn und S. Staudaher, *ApJ* **710** (2010), 289.
- [20] W.H. Baumgartner, J. Tueller, C.B. Markwardt, G.K. Skinner, S. Barthelmy, R.F. Mushotzky, P.A. Evans und N. Gehrels, *ApJS* **207** (2013), 19.
- [21] T. Beckert, T. Driebe, S.F. Hönig und G. Weigelt, *A&A* **486** (2008), L17.
- [22] V. Beckmann und C.R. Shrader: *Active Galactic Nuclei*, August 2012.
- [23] E.F. Bell, D.H. McIntosh, N. Katz und M.D. Weinberg, *ApJS* **149** (2003), 289.
- [24] E.F. Bell, C. Wolf, K. Meisenheimer, H.W. Rix, A. Borch, S. Dye, M. Kleinheinrich, L. Wisotzki und D.H. McIntosh, *ApJ* **608** (2004), 752.
- [25] N. Bennert, H. Falcke, Y. Shchekinov und A.S. Wilson: *Comparing AGN broad and narrow line regions. Comparing AGN broad and narrow line regions*, In *The Interplay Among Black Holes, Stars and ISM in Galactic Nuclei*, herausgegeben von T. Storchi-Bergmann, L. C. Ho und H. R. Schmitt, Band 222 von *IAU Symposium*. (November 2004) Seiten 307–308.
- [26] M.C. Bentz, J.L. Walsh, A.J. Barth, N. Baliber, V.N. Bennert, G. Canalizo, A.V. Filippenko, M. Ganeshalingam, E.L. Gates, J.E. Greene, M.G. Hidas, K.D. Hiner, N. Lee, W. Li, M.A. Malkan, T. Minezaki, Y. Sakata, F.J.D. Serduke, J.M. Silverman, T.N. Steele, D. Stern, R.A. Street, C.E. Thornton, T. Treu, X. Wang, J.H. Woo und Y. Yoshii, *ApJ* **705** (2009), 199.
- [27] M. Bernardi, R.K. Sheth, J. Annis, S. Burles, D.P. Finkbeiner, R.H. Lupton, D.J. Schlegel, M. SubbaRao, N.A. Bahcall, J.P. Blakeslee, J. Brinkmann, F.J. Castander, A.J. Connolly, I. Csabai, M. Doi, M. Fukugita, J. Frieman, T. Heckman,

- G.S. Hennessy, Ž. Ivezić, G.R. Knapp, D.Q. Lamb, T. McKay, J.A. Munn, R. Nichol, S. Okamura, D.P. Schneider, A.R. Thakar und D.G. York, *AJ* **125** (2003), 1882.
- [28] S. Berta, B. Magnelli, D. Lutz, B. Altieri, H. Aussel, P. Andreani, O. Bauer, A. Bongiovanni, A. Cava, J. Cepa, A. Cimatti, E. Daddi, H. Dominguez, D. Elbaz, H. Feuchtgruber, N.M. Förster Schreiber, R. Genzel, C. Gruppioni, R. Katterloher, G. Magdis, R. Maiolino, R. Nordon, A.M. Pérez García, A. Poglitsch, P. Popesso, F. Pozzi, L. Riguccini, G. Rodighiero, A. Saintonge, P. Santini, M. Sanchez-Portal, L. Shao, E. Sturm, L.J. Tacconi, I. Valtchanov, M. Wetzstein und E. Wieprecht, *A&A* **518** (2010), L30.
- [29] P.N. Best, G. Kauffmann, T.M. Heckman, J. Brinchmann, S. Charlot, Ž. Ivezić und S.D.M. White, *MNRAS* **362** (2005), 25.
- [30] M. Béthermin, H. Dole, A. Beelen und H. Aussel, *A&A* **512** (2010), A78.
- [31] M.R. Blanton, D.J. Schlegel, M.A. Strauss, J. Brinkmann, D. Finkbeiner, M. Fukugita, J.E. Gunn, D.W. Hogg, Ž. Ivezić, G.R. Knapp, R.H. Lupton, J.A. Munn, D.P. Schneider, M. Tegmark und I. Zehavi, *AJ* **129** (2005), 2562.
- [32] A. Böhm, L. Wisotzki, E.F. Bell, K. Jahnke, C. Wolf, D. Bacon, M. Barden, M.E. Gray, G. Hoeppe, S. Jogee, D.H. McIntosh, C.Y. Peng, A.R. Robaina, M. Balogh, F.D. Barazza, J.A.R. Caldwell, C. Heymans, B. Häußler, E. van Kampen, K. Lane, K. Meisenheimer, S.F. Sánchez, A.N. Taylor und X. Zheng, *A&A* **549** (2013), A46.
- [33] T. Boroson, *AJ* **130** (2005), 381.
- [34] C. Borys, A.W. Blain, A. Dey, E. Le Floc'h, B.T. Jannuzi, V. Barnard, C. Bian, M. Brodwin, K. Menéndez-Delmestre, D. Thompson, K. Brand, M.J.I. Brown, C.D. Dowell, P. Eisenhardt, D. Farrah, D.T. Frayer, J. Higdon, S. Higdon, T. Phillips, B.T. Soifer, D. Stern und D. Weedman, *ApJ* **636** (2006), 134.
- [35] N. Bouché, A. Dekel, R. Genzel, S. Genel, G. Cresci, N.M. Förster Schreiber, K.L. Shapiro, R.I. Davies und L. Tacconi, *ApJ* **718** (2010), 1001.
- [36] F. Bournaud, A. Dekel, R. Teyssier, M. Cacciato, E. Daddi, S. Juneau und F. Shankar, *ApJ* **741** (2011), L33.
- [37] R.J. Bouwens, G.D. Illingworth, P.A. Oesch, M. Stiavelli, P. van Dokkum, M. Trenti, D. Magee, I. Labbé, M. Franx, C.M. Carollo und V. Gonzalez, *ApJ* **709** (2010), L133.
- [38] R.G. Bower, A.J. Benson, R. Malbon, J.C. Helly, C.S. Frenk, C.M. Baugh, S. Cole und C.G. Lacey, *MNRAS* **370** (2006), 645.

- [39] K. Brand, J. Moustakas, L. Armus, R.J. Assef, M.J.I. Brown, R.R. Cool, V. Desai, A. Dey, E. Le Floch, B.T. Jannuzi, C.S. Kochanek, J. Melbourne, C.J. Papovich und B.T. Soifer, *ApJ* **693** (2009), 340.
- [40] W.N. Brandt, D.M. Alexander, A.E. Hornschemeier, G.P. Garmire, D.P. Schneider, A.J. Barger, F.E. Bauer, P.S. Broos, L.L. Cowie, L.K. Townsley, D.N. Burrows, G. Chartas, E.D. Feigelson, R.E. Griffiths, J.A. Nousek und W.L.W. Sargent, *AJ* **122** (2001), 2810.
- [41] J. Brinchmann, S. Charlot, S.D.M. White, C. Tremonti, G. Kauffmann, T. Heckman und J. Brinkmann, *MNRAS* **351** (2004), 1151.
- [42] M. Brusa, F. Fiore, P. Santini, A. Grazian, A. Comastri, G. Zamorani, G. Hasinger, A. Merloni, F. Civano, A. Fontana und V. Mainieri, *A&A* **507** (2009), 1277.
- [43] G. Bruzual und S. Charlot, *MNRAS* **344** (2003), 1000.
- [44] L. Burtscher, W. Jaffe, D. Raban, K. Meisenheimer, K.R.W. Tristram und H. Röttgering, *ApJ* **705** (2009), L53.
- [45] C.N. Cardamone, C.M. Urry, M. Damen, P. van Dokkum, E. Treister, I. Labbé, S.N. Virani, P. Lira und E. Gawiser, *ApJ* **680** (2008), 130.
- [46] C.N. Cardamone, C.M. Urry, K. Schawinski, E. Treister, G. Brammer und E. Gawiser, *ApJ* **721** (2010), L38.
- [47] R. Cid Fernandes, G. Stasińska, A. Mateus und N. Vale Asari, *MNRAS* **413** (2011), 1687.
- [48] L. Ciotti und J.P. Ostriker, *ApJ* **665** (2007), 1038.
- [49] D.L. Clements, W.J. Sutherland, R.G. McMahon und W. Saunders, *MNRAS* **279** (1996), 477.
- [50] F. Combes, S. García-Burillo, J. Braine, E. Schinnerer, F. Walter und L. Colina, *A&A* **550** (2013), A41.
- [51] S. Cotini, E. Ripamonti, A. Caccianiga, M. Colpi, R. Della Ceca, M. Mapelli, P. Severgnini und A. Segreto, *MNRAS* **431** (2013), 2661.
- [52] L. Cram, A. Hopkins, B. Mobasher und M. Rowan-Robinson, *ApJ* **507** (1998), 155.
- [53] D.M. Crenshaw, S.B. Kraemer und J.R. Gabel, *AJ* **126** (2003), 1690.
- [54] G. Cresci, E.K.S. Hicks, R. Genzel, N.M.F. Schreiber, R. Davies, N. Bouché, P. Buschkamp, S. Genel, K. Shapiro, L. Tacconi, J. Sommer-Larsen, A. Burkert, F. Eisenhauer, O. Gerhard, D. Lutz, T. Naab, A. Sternberg, A. Cimatti, E. Daddi, D.K. Erb, J. Kurk, S.L. Lilly, A. Renzini, A. Shapley, C.C. Steidel und K. Caputi, *ApJ* **697** (2009), 115.

- [55] G. Cusumano: *The Palermo Swift-BAT Hard X-ray Catalogue: Results after 39 Months of Sky Survey. The Palermo Swift-BAT Hard X-ray Catalogue: Results after 39 Months of Sky Survey*, In *American Institute of Physics Conference Series*, herausgegeben von J. Rodriguez und P. Ferrando, Band 1126 von *American Institute of Physics Conference Series*. (Mai 2009) Seiten 104–107.
- [56] G. Cusumano, V. La Parola, A. Segreto, C. Ferrigno, A. Maselli, B. Sbarufatti, P. Romano, G. Chincarini, P. Giommi, N. Masetti, A. Moretti, P. Parisi und G. Tagliaferri, *A&A* **524** (2010), A64.
- [57] G. Cusumano, V. La Parola, A. Segreto, V. Mangano, C. Ferrigno, A. Maselli, P. Romano, T. Mineo, B. Sbarufatti, S. Campana, G. Chincarini, P. Giommi, N. Masetti, A. Moretti und G. Tagliaferri, *A&A* **510** (2010), A48.
- [58] G. Cusumano, A. Segreto, V. La Parola und A. Maselli: *The Palermo Swift-BAT hard X-ray catalogue. Results after 66 months of sky survey. The Palermo Swift-BAT hard X-ray catalogue. Results after 66 months of sky survey.*, In *39th COSPAR Scientific Assembly*, Band 39 von *COSPAR Meeting*. (Juli 2012) Seite 382.
- [59] R.M. Cutri, E.L. Wright, T. Conrow, J. Bauer, D. Benford, H. Brandenburg, J. Daley, P.R.M. Eisenhardt, T. Evans, S. Fajardo-Acosta, J. Fowler, C. Gelino, C. Grillmair, M. Harbut, D. Hoffman, T. Jarrett, J.D. Kirkpatrick, D. Leisawitz, W. Liu, A. Mainzer, K. Marsh, F. Masci, H. McCallon, D. Padgett, M.E. Ressler, D. Royer, M.F. Skrutskie, S.A. Stanford, P.L. Wyatt, D. Tholen, C.W. Tsai, S. Wachter, S.L. Wheelock, L. Yan, R. Alles, R. Beck, T. Grav, J. Masiero, B. McCollum, P. McGehee, M. Papin und M. Wittman. *Explanatory Supplement to the WISE All-Sky Data Release Products*. Technischer Bericht, März 2012.
- [60] E. Daddi, F. Bournaud, F. Walter, H. Dannerbauer, C.L. Carilli, M. Dickinson, D. Elbaz, G.E. Morrison, D. Riechers, M. Onodera, F. Salmi, M. Krips und D. Stern, *ApJ* **713** (2010), 686.
- [61] E. Daddi, M. Dickinson, G. Morrison, R. Chary, A. Cimatti, D. Elbaz, D. Frayer, A. Renzini, A. Pope, D.M. Alexander, F.E. Bauer, M. Giavalisco, M. Huynh, J. Kurk und M. Mignoli, *ApJ* **670** (2007), 156.
- [62] D.W. Darg, S. Kaviraj, C.J. Lintott, K. Schawinski, M. Sarzi, S. Bamford, J. Silk, D. Andreescu, P. Murray, R.C. Nichol, M.J. Raddick, A. Slosar, A.S. Szalay, D. Thomas und J. Vandenberg, *MNRAS* **401** (2010), 1552.
- [63] R.I. Davies, W. Maciejewski, E.K.S. Hicks, L.J. Tacconi, R. Genzel und H. Engel, *ApJ* **702** (2009), 114.
- [64] T. de Graauw, F.P. Helmich, T.G. Phillips, J. Stutzki, E. Caux, N.D. Whyborn, P. Dieleman, P.R. Roelfsema, H. Aarts, R. Assendorp, R. Bachiller, W. Baechtold,

- A. Barcia, D.A. Beintema, V. Belitsky, A.O. Benz, R. Bieber, A. Boogert, C. Borys, B. Bumble, P. Caïs, M. Caris, P. Cerulli-Irelli, G. Chattopadhyay, S. Cherednichenko, M. Ciechanowicz, O. Coeur-Joly, C. Comito, A. Cros, A. de Jonge, G. de Lange, B. Delforges, Y. Delorme, T. den Boggende, J.M. Desbat, C. Diez-González, A.M. di Giorgio, L. Dubbeldam, K. Edwards, M. Eggens, N. Erickson, J. Evers, M. Fich, T. Finn, B. Franke, T. Gaier, C. Gal, J.R. Gao, J.D. Gallego, S. Gauffre, J.J. Gill, S. Glenz, H. Golstein, H. Goulooze, T. Gunsing, R. Güsten, P. Hartogh, W.A. Hatch, R. Higgins, E.C. Honingh, R. Huisman, B.D. Jackson, H. Jacobs, K. Jacobs, C. Jarchow, H. Javadi, W. Jellema, M. Justen, A. Karpov, C. Kasemann, J. Kawamura, G. Keizer, D. Kester, T.M. Klapwijk, T. Klein, E. Kollberg, J. Kooi, P.P. Kooiman, B. Kopf, M. Krause, J.M. Krieg, C. Kramer, B. Kruizenga, T. Kuhn, W. Laauwen, R. Lai, B. Larsson, H.G. Leduc, C. Leinz, R.H. Lin, R. Liseau, G.S. Liu, A. Loose, I. López-Fernandez, S. Lord, W. Luinge, A. Marston, J. Martín-Pintado, A. Maestrini, F.W. Maiwald, C. McCoe, I. Mehdi, A. Megej, M. Melchior, L. Meinsma, H. Merkel, M. Michalska, C. Monstein, D. Moratschke, P. Morris, H. Muller, J.A. Murphy, A. Naber, E. Natale, W. Nowosielski, F. Nuzzolo, M. Olberg, M. Olbrich, R. Orfei, P. Orleanski, V. Ossenkopf, T. Peacock, J.C. Pearson, I. Peron, S. Phillip-May, L. Piazzo, P. Planesas, M. Rataj, L. Ravera, C. Risacher, M. Salez, L.A. Samoska, P. Saraceno, R. Schieder, E. Schlecht, F. Schlöder, F. Schmülling, M. Schultz, K. Schuster, O. Siebertz, H. Smit, R. Szczerba, R. Shipman, E. Steinmetz, J.A. Stern, M. Stokroos, R. Teipen, D. Teyssier, T. Tils, N. Trappe, C. van Baaren, B.J. van Leeuwen, H. van de Stadt, H. Visser, K.J. Wildeman, C.K. Wafelbakker, J.S. Ward, P. Wesselius, W. Wild, S. Wulff, H.J. Wunsch, X. Tielens, P. Zaal, H. Zirath, J. Zmuidzinis und F. Zwart, *A&A* **518** (2010), L6.
- [65] P. Di Matteo, F. Combes, A.L. Melchior und B. Semelin, *A&A* **468** (2007), 61.
- [66] T. Di Matteo, J. Colberg, V. Springel, L. Hernquist und D. Sijacki, *ApJ* **676** (2008), 33.
- [67] T. Di Matteo, V. Springel und L. Hernquist, *Nature* **433** (2005), 604.
- [68] M. Dickinson, M. Giavalisco und GOODS Team: *The Great Observatories Origins Deep Survey. The Great Observatories Origins Deep Survey*, In *The Mass of Galaxies at Low and High Redshift*, herausgegeben von R. Bender und A. Renzini. (2003) Seite 324.
- [69] J.L. Donley, G.H. Rieke, P.G. Pérez-González und G. Barro, *ApJ* **687** (2008), 111.
- [70] R.J.H. Dunn und A.C. Fabian, *MNRAS* **385** (2008), 757.
- [71] A. Einstein, *Annalen der Physik* **354** (1916), 769.
- [72] D. Elbaz, E. Daddi, D. Le Borgne, M. Dickinson, D.M. Alexander, R.R. Chary, J.L. Starck, W.N. Brandt, M. Kitzbichler, E. MacDonald, M. Nonino, P. Popesso, D. Stern und E. Vanzella, *A&A* **468** (2007), 33.

- [73] M. Elitzur und I. Shlosman, *ApJ* **648** (2006), L101.
- [74] S.L. Ellison, D.R. Patton, J.T. Mendel und J.M. Scudder, *MNRAS* **418** (2011), 2043.
- [75] S.L. Ellison, D.R. Patton, L. Simard und A.W. McConnachie, *AJ* **135** (2008), 1877.
- [76] B.G. Elmegreen: *Star Formation in Disks: Spiral Arms, Turbulence, and Triggering Mechanisms*. *Star Formation in Disks: Spiral Arms, Turbulence, and Triggering Mechanisms*, In *IAU Symposium*, herausgegeben von J. Andersen, Nordströara, B. m und J. Bland-Hawthorn, Band 254 von *IAU Symposium*. (März 2009) Seiten 289–300.
- [77] P. Englmaier und I. Shlosman, *ApJ* **617** (2004), L115.
- [78] M. Eskew, D. Zaritsky und S. Meidt, *AJ* **143** (2012), 139.
- [79] I.N. Evans, H.C. Ford, A.L. Kinney, R.R.J. Antonucci, L. Armus und S. Caganoff, *ApJ* **369** (1991), L27.
- [80] A.C. Fabian, *MNRAS* **308** (1999), L39.
- [81] A.C. Fabian, *Astronomische Nachrichten* **329** (2008), 155.
- [82] A.C. Fabian, J.S. Sanders, G.B. Taylor, S.W. Allen, C.S. Crawford, R.M. Johnstone und K. Iwasawa, *MNRAS* **366** (2006), 417.
- [83] A.C. Fabian, I. Smail, K. Iwasawa, S.W. Allen, A.W. Blain, C.S. Crawford, S. Ettori, R.J. Ivison, R.M. Johnstone, J.P. Kneib und R.J. Wilman, *MNRAS* **315** (2000), L8.
- [84] B.L. Fanaroff und J.M. Riley, *MNRAS* **167** (1974), 31P.
- [85] L. Ferrarese und D. Merritt, *ApJ* **539** (2000), L9.
- [86] N.M. Förster Schreiber, R. Genzel, N. Bouché, G. Cresci, R. Davies, P. Buschkamp, K. Shapiro, L.J. Tacconi, E.K.S. Hicks, S. Genel, A.E. Shapley, D.K. Erb, C.C. Steidel, D. Lutz, F. Eisenhauer, S. Gillessen, A. Sternberg, A. Renzini, A. Cimatti, E. Daddi, J. Kurk, S. Lilly, X. Kong, M.D. Lehnert, N. Nesvadba, A. Verma, H. McCracken, N. Arimoto, M. Mignoli und M. Onodera, *ApJ* **706** (2009), 1364.
- [87] D.A. Gadotti und G. Kauffmann, *MNRAS* **399** (2009), 621.
- [88] E. Gallo, T. Treu, P.J. Marshall, J.H. Woo, C. Leipski und R. Antonucci, *ApJ* **714** (2010), 25.
- [89] R. Ganguly und M.S. Brotherton, *ApJ* **672** (2008), 102.

- [90] G.P. Garmire, M.W. Bautz, P.G. Ford, J.A. Nousek und G.R. Ricker, Jr.: *Advanced CCD imaging spectrometer (ACIS) instrument on the Chandra X-ray Observatory. Advanced CCD imaging spectrometer (ACIS) instrument on the Chandra X-ray Observatory*, In *Society of Photo-Optical Instrumentation Engineers (SPIE) Conference Series*, herausgegeben von J. E. Truemper und H. D. Tananbaum, Band 4851 von *Society of Photo-Optical Instrumentation Engineers (SPIE) Conference Series*. (März 2003) Seiten 28–44.
- [91] J.E. Geach, I. Smail, S.M. Moran, L.A. MacArthur, C.d.P. Lagos und A.C. Edge, *ApJ* **730** (2011), L19.
- [92] K. Gebhardt, R. Bender, G. Bower, A. Dressler, S.M. Faber, A.V. Filippenko, R. Green, C. Grillmair, L.C. Ho, J. Kormendy, T.R. Lauer, J. Magorrian, J. Pinkney, D. Richstone und S. Tremaine, *ApJ* **539** (2000), L13.
- [93] N. Gehrels, G. Chincarini, P. Giommi, K.O. Mason, J.A. Nousek, A.A. Wells, N.E. White, S.D. Barthelmy, D.N. Burrows, L.R. Cominsky, K.C. Hurley, F.E. Marshall, P. Mészáros, P.W.A. Roming, L. Angelini, L.M. Barbier, T. Belloni, S. Campana, P.A. Caraveo, M.M. Chester, O. Citterio, T.L. Cline, M.S. Cropper, J.R. Cummings, A.J. Dean, E.D. Feigelson, E.E. Fenimore, D.A. Frail, A.S. Fruchter, G.P. Garmire, K. Gendreau, G. Ghisellini, J. Greiner, J.E. Hill, S.D. Hunsberger, H.A. Krimm, S.R. Kulkarni, P. Kumar, F. Lebrun, N.M. Lloyd-Ronning, C.B. Markwardt, B.J. Mattson, R.F. Mushotzky, J.P. Norris, J. Osborne, B. Paczynski, D.M. Palmer, H.S. Park, A.M. Parsons, J. Paul, M.J. Rees, C.S. Reynolds, J.E. Rhoads, T.P. Sasseen, B.E. Schaefer, A.T. Short, A.P. Smale, I.A. Smith, L. Stella, G. Tagliaferri, T. Takahashi, M. Tashiro, L.K. Townsley, J. Tueller, M.J.L. Turner, M. Vietri, W. Voges, M.J. Ward, R. Willingale, F.M. Zerbi und W.W. Zhang, *ApJ* **611** (2004), 1005.
- [94] R. Genzel, A. Burkert, N. Bouché, G. Cresci, N.M. Förster Schreiber, A. Shapley, K. Shapiro, L.J. Tacconi, P. Buschkamp, A. Cimatti, E. Daddi, R. Davies, F. Eisenhauer, D.K. Erb, S. Genel, O. Gerhard, E. Hicks, D. Lutz, T. Naab, T. Ott, S. Rabien, A. Renzini, C.C. Steidel, A. Sternberg und S.J. Lilly, *ApJ* **687** (2008), 59.
- [95] R. Genzel, D. Lutz, E. Sturm, E. Egami, D. Kunze, A.F.M. Moorwood, D. Rigopoulou, H.W.W. Spoon, A. Sternberg, L.E. Tacconi-Garman, L. Tacconi und N. Thatte, *ApJ* **498** (1998), 579.
- [96] A. Georgakakis, A.L. Coil, E.S. Laird, R.L. Griffith, K. Nandra, J.M. Lotz, C.M. Pierce, M.C. Cooper, J.A. Newman und A.M. Koekemoer, *MNRAS* **397** (2009), 623.
- [97] R. Gilli, A. Comastri und G. Hasinger, *A&A* **463** (2007), 79.
- [98] A.D. Goulding, D.M. Alexander, B.D. Lehmer und J.R. Mullaney, *MNRAS* **406** (2010), 597.

- [99] A.D. Goulding, D.M. Alexander, J.R. Mullaney, J.M. Gelbord, R.C. Hickox, M. Ward und M.G. Watson, *MNRAS* **411** (2011), 1231.
- [100] J.E. Greene und L.C. Ho, *ApJ* **667** (2007), 131.
- [101] M.J. Griffin, A. Abergel, A. Abreu, P.A.R. Ade, P. André, J.L. Augueres, T. Babbedge, Y. Bae, T. Baillie, J.P. Baluteau, M.J. Barlow, G. Bendo, D. Benielli, J.J. Bock, P. Bonhomme, D. Brisbin, C. Brockley-Blatt, M. Caldwell, C. Cara, N. Castro-Rodriguez, R. Cerulli, P. Chanical, S. Chen, E. Clark, D.L. Clements, L. Clerc, J. Coker, D. Communal, L. Conversi, P. Cox, D. Crumb, C. Cunningham, F. Daly, G.R. Davis, P. de Antoni, J. Delderfield, N. Devin, A. di Giorgio, I. Didschuns, K. Dohlen, M. Donati, A. Dowell, C.D. Dowell, L. Duband, L. Dumaye, R.J. Emery, M. Ferlet, D. Ferrand, J. Fontignie, M. Fox, A. Franceschini, M. Frerking, T. Fulton, J. Garcia, R. Gastaud, W.K. Gear, J. Glenn, A. Goizel, D.K. Griffin, T. Grundy, S. Guest, L. Guillemet, P.C. Hargrave, M. Harwit, P. Hastings, E. Hatziminaoglou, M. Herman, B. Hinde, V. Hristov, M. Huang, P. Imhof, K.J. Isaak, U. Israelsson, R.J. Ivison, D. Jennings, B. Kiernan, K.J. King, A.E. Lange, W. Latter, G. Laurent, P. Laurent, S.J. Leeks, E. Lellouch, L. Levenson, B. Li, J. Li, J. Lilienthal, T. Lim, S.J. Liu, N. Lu, S. Madden, G. Mainetti, P. Marliani, D. McKay, K. Mercier, S. Molinari, H. Morris, H. Moseley, J. Mulder, M. Mur, D.A. Naylor, H. Nguyen, B. O'Halloran, S. Oliver, G. Olofsson, H.G. Olofsson, R. Orfei, M.J. Page, I. Pain, P. Panuzzo, A. Papageorgiou, G. Parks, P. Parr-Burman, A. Pearce, C. Pearson, I. Pérez-Fournon, F. Pinsard, G. Pisano, J. Podosek, M. Pohlen, E.T. Polehampton, D. Pouliquen, D. Rigopoulou, D. Rizzo, I.G. Roseboom, H. Roussel, M. Rowan-Robinson, B. Rownd, P. Saraceno, M. Sauvage, R. Savage, G. Savini, E. Sawyer, C. Scharmberg, D. Schmitt, N. Schneider, B. Schulz, A. Schwartz, R. Shafer, D.L. Shupe, B. Sibthorpe, S. Sidher, A. Smith, A.J. Smith, D. Smith, L. Spencer, B. Stobie, R. Sudiwala, K. Sukhatme, C. Surace, J.A. Stevens, B.M. Swinyard, M. Trichas, T. Tourette, H. Triou, S. Tseng, C. Tucker, A. Turner, M. Vaccari, I. Valtchanov, L. Vigroux, E. Virique, G. Voellmer, H. Walker, R. Ward, T. Waskett, M. Weilert, R. Wesson, G.J. White, N. Whitehouse, C.D. Wilson, B. Winter, A.L. Woodcraft, G.S. Wright, C.K. Xu, A. Zavagno, M. Zemcov, L. Zhang und E. Zonca, *A&A* **518** (2010), L3.
- [102] B.A. Groves, T.M. Heckman und G. Kauffmann, *MNRAS* **371** (2006), 1559.
- [103] Q. Gu und J. Huang, *ApJ* **579** (2002), 205.
- [104] K. Gültekin, D.O. Richstone, K. Gebhardt, T.R. Lauer, S. Tremaine, M.C. Aller, R. Bender, A. Dressler, S.M. Faber, A.V. Filippenko, R. Green, L.C. Ho, J. Kormendy, J. Magorrian, J. Pinkney und C. Siopis, *ApJ* **698** (2009), 198.
- [105] J.E. Gunn, M. Carr, C. Rockosi, M. Sekiguchi, K. Berry, B. Elms, E. de Haas, Ž. Ivezić, G. Knapp, R. Lupton, G. Pauls, R. Simcoe, R. Hirsch, D. Sanford,

- S. Wang, D. York, F. Harris, J. Annis, L. Bartozek, W. Boroski, J. Bakken, M. Halde-
man, S. Kent, S. Holm, D. Holmgren, D. Petravick, A. Prosapio, R. Rechenmacher,
M. Doi, M. Fukugita, K. Shimasaku, N. Okada, C. Hull, W. Siegmund, E. Mannery,
M. Blouke, D. Heidtman, D. Schneider, R. Lucinio und J. Brinkman, *AJ* **116** (1998),
3040.
- [106] F. Haardt und L. Maraschi, *ApJ* **413** (1993), 507.
- [107] N. Häring und H.W. Rix, *ApJ* **604** (2004), L89.
- [108] F.D.A. Hartwick und D. Schade, *ARA&A* **28** (1990), 437.
- [109] G. Hasinger, T. Miyaji und M. Schmidt, *A&A* **441** (2005), 417.
- [110] T.M. Heckman, G. Kauffmann, J. Brinchmann, S. Charlot, C. Tremonti und
S.D.M. White, *ApJ* **613** (2004), 109.
- [111] T.M. Heckman, A. Ptak, A. Hornschemeier und G. Kauffmann, *ApJ* **634** (2005),
161.
- [112] R.C. Hickox, C. Jones, W.R. Forman, S.S. Murray, C.S. Kochanek, D. Eisenstein,
B.T. Jannuzi, A. Dey, M.J.I. Brown, D. Stern, P.R. Eisenhardt, V. Gorjian, M. Brod-
win, R. Narayan, R.J. Cool, A. Kenter, N. Caldwell und M.E. Anderson, *ApJ* **696**
(2009), 891.
- [113] L.C. Ho, *ARA&A* **46** (2008), 475.
- [114] S.F. Hönig, M. Kishimoto, R. Antonucci, A. Marconi, M.A. Prieto, K. Tristram und
G. Weigelt, *ApJ* **755** (2012), 149.
- [115] S.F. Hönig, M. Kishimoto, P. Gandhi, A. Smette, D. Asmus, W. Duschl, M. Polletta
und G. Weigelt, *A&A* **515** (2010), A23.
- [116] A.M. Hopkins, R.E. Schulte-Ladbeck und I.O. Drozdovsky, *AJ* **124** (2002), 862.
- [117] P.F. Hopkins, K. Bundy, D. Croton, L. Hernquist, D. Keres, S. Khochfar, K. Stewart,
A. Wetzel und J.D. Younger, *ApJ* **715** (2010), 202.
- [118] P.F. Hopkins, C.C. Hayward, D. Narayanan und L. Hernquist, *MNRAS* **420** (2012),
320.
- [119] P.F. Hopkins, L. Hernquist, T.J. Cox, T. Di Matteo, B. Robertson und V. Springel,
ApJS **163** (2006), 1.
- [120] P.F. Hopkins, L. Hernquist, T.J. Cox und D. Kereš, *ApJS* **175** (2008), 356.
- [121] P.F. Hopkins und E. Quataert, *MNRAS* **407** (2010), 1529.

- [122] E.P. Hubble, *ApJ* **64** (1926), 321.
- [123] H.S. Hwang, M.J. Geller, M.J. Kurtz, I.P. Dell'Antonio und D.G. Fabricant, *ApJ* **758** (2012), 25.
- [124] W. Jaffe, K. Meisenheimer, H.J.A. Röttgering, C. Leinert, A. Richichi, O. Chesneau, D. Fraix-Burnet, A. Glazeborg-Kluttig, G.L. Granato, U. Graser, B. Heijligers, R. Köhler, F. Malbet, G.K. Miley, F. Paresce, J.W. Pel, G. Perrin, F. Przygodda, M. Schoeller, H. Sol, L.B.F.M. Waters, G. Weigelt, J. Woillez und P.T. de Zeeuw, *Nature* **429** (2004), 47.
- [125] G. Kauffmann und M. Haehnelt, *MNRAS* **311** (2000), 576.
- [126] G. Kauffmann und T.M. Heckman, *MNRAS* **397** (2009), 135.
- [127] G. Kauffmann, T.M. Heckman, T. Budavári, S. Charlot, C.G. Hoopes, D.C. Martin, M. Seibert, T.A. Barlow, L. Bianchi, T. Conrow, J. Donas, K. Forster, P.G. Friedman, Y.W. Lee, B.F. Madore, B. Milliard, P.F. Morrissey, S.G. Neff, R.M. Rich, D. Schiminovich, T. Small, A.S. Szalay, T.K. Wyder und S.K. Yi, *ApJS* **173** (2007), 357.
- [128] G. Kauffmann, T.M. Heckman, G. De Lucia, J. Brinchmann, S. Charlot, C. Tremonti, S.D.M. White und J. Brinkmann, *MNRAS* **367** (2006), 1394.
- [129] G. Kauffmann, T.M. Heckman, C. Tremonti, J. Brinchmann, S. Charlot, S.D.M. White, S.E. Ridgway, J. Brinkmann, M. Fukugita, P.B. Hall, Ž. Ivezić, G.T. Richards und D.P. Schneider, *MNRAS* **346** (2003), 1055.
- [130] G. Kauffmann, T.M. Heckman, S.D.M. White, S. Charlot, C. Tremonti, J. Brinchmann, G. Bruzual, E.W. Peng, M. Seibert, M. Bernardi, M. Blanton, J. Brinkmann, F. Castander, I. Csábai, M. Fukugita, Z. Ivezić, J.A. Munn, R.C. Nichol, N. Padmanabhan, A.R. Thakar, D.H. Weinberg und D. York, *MNRAS* **341** (2003), 33.
- [131] G. Kauffmann, T.M. Heckman, S.D.M. White, S. Charlot, C. Tremonti, E.W. Peng, M. Seibert, J. Brinkmann, R.C. Nichol, M. SubbaRao und D. York, *MNRAS* **341** (2003), 54.
- [132] L.J. Kewley, M.A. Dopita, R.S. Sutherland, C.A. Heisler und J. Trevena, *ApJ* **556** (2001), 121.
- [133] L.J. Kewley, B. Groves, G. Kauffmann und T. Heckman, *MNRAS* **372** (2006), 961.
- [134] A. King, *ApJ* **596** (2003), L27.
- [135] A.R. King, K. Zubovas und C. Power, *MNRAS* **415** (2011), L6.
- [136] M. Kishimoto, S.F. Hönic, R. Antonucci, R. Barvainis, T. Kotani, K.R.W. Tristram, G. Weigelt und K. Levin, *A&A* **527** (2011), A121.

- [137] M. Kishimoto, S.F. Hönig, R. Antonucci, F. Millour, K.R.W. Tristram und G. Weigelt, *A&A* **536** (2011), A78.
- [138] M. Kishimoto, S.F. Hönig, K.R.W. Tristram und G. Weigelt, *A&A* **493** (2009), L57.
- [139] J.H. Knapen und P.A. James, *ApJ* **698** (2009), 1437.
- [140] D.D. Kocevski, S.M. Faber, M. Mozena, A.M. Koekemoer, K. Nandra, C. Rangel, E.S. Laird, M. Brusa, S. Wuyts, J.R. Trump, D.C. Koo, R.S. Somerville, E.F. Bell, J.M. Lotz, D.M. Alexander, F. Bournaud, C.J. Conselice, T. Dahlen, A. Dekel, J.L. Donley, J.S. Dunlop, A. Finoguenov, A. Georgakakis, M. Giavalisco, Y. Guo, N.A. Grogin, N.P. Hathi, S. Juneau, J.S. Kartaltepe, R.A. Lucas, E.J. McGrath, D.H. McIntosh, B. Mobasher, A.R. Robaina, D. Rosario, A.N. Straughn, A. van der Wel und C. Villforth, *ApJ* **744** (2012), 148.
- [141] J. Kormendy und R.C. Kennicutt, Jr., *ARA&A* **42** (2004), 603.
- [142] J. Kormendy und D. Richstone, *ARA&A* **33** (1995), 581.
- [143] M. Koss, R. Mushotzky, S. Veilleux, L.M. Winter, W. Baumgartner, J. Tueller, N. Gehrels und L. Valencic, *ApJ* **739** (2011), 57.
- [144] C.Y. Kuo, J. Lim, Y.W. Tang und P.T.P. Ho, *ApJ* **679** (2008), 1047.
- [145] M. Lacy, L.J. Storrie-Lombardi, A. Sajina, P.N. Appleton, L. Armus, S.C. Chapman, P.I. Choi, D. Fadda, F. Fang, D.T. Frayer, I. Heinrichsen, G. Helou, M. Im, F.R. Marleau, F. Masci, D.L. Shupe, B.T. Soifer, J. Surace, H.I. Teplitz, G. Wilson und L. Yan, *ApJS* **154** (2004), 166.
- [146] S.M. LaMassa, T.M. Heckman, A. Ptak, L. Martins, V. Wild und P. Sonnentrucker, *ApJ* **720** (2010), 786.
- [147] S.M. LaMassa, T.M. Heckman, A. Ptak, D. Schiminovich, M. O'Dowd und B. Bertin-court, *ApJ* **758** (2012), 1.
- [148] A. Lawrence, *MNRAS* **252** (1991), 586.
- [149] C. Li, G. Kauffmann, T.M. Heckman, Y.P. Jing und S.D.M. White, *MNRAS* **385** (2008), 1903.
- [150] C. Li, G. Kauffmann, T.M. Heckman, S.D.M. White und Y.P. Jing, *MNRAS* **385** (2008), 1915.
- [151] C. Li, G. Kauffmann, L. Wang, S.D.M. White, T.M. Heckman und Y.P. Jing, *MNRAS* **373** (2006), 457.
- [152] L.X. Li, *MNRAS* **388** (2008), 1487.

- [153] X. Liu, Y. Shen und M.A. Strauss, *ApJ* **745** (2012), 94.
- [154] J.M. Lotz, J. Primack und P. Madau, *AJ* **128** (2004), 163.
- [155] B. Luo, F.E. Bauer, W.N. Brandt, D.M. Alexander, B.D. Lehmer, D.P. Schneider, M. Brusa, A. Comastri, A.C. Fabian, A. Finoguenov, R. Gilli, G. Hasinger, A.E. Hornschemeier, A. Koekemoer, V. Mainieri, M. Paolillo, P. Rosati, O. Shemmer, J.D. Silverman, I. Smail, A.T. Steffen und C. Vignali, *ApJS* **179** (2008), 19.
- [156] D. Lutz, V. Mainieri, D. Rafferty, L. Shao, G. Hasinger, A. Weiß, F. Walter, I. Smail, D.M. Alexander, W.N. Brandt, S. Chapman, K. Coppin, N.M. Förster Schreiber, E. Gawiser, R. Genzel, T.R. Greve, R.J. Ivison, A.M. Koekemoer, P. Kurczynski, K.M. Menten, R. Nordon, P. Popesso, E. Schinnerer, J.D. Silverman, J. Wardlow und Y.Q. Xue, *ApJ* **712** (2010), 1287.
- [157] D. Lutz, E. Sturm, L.J. Tacconi, E. Valiante, M. Schweitzer, H. Netzer, R. Maiolino, P. Andreani, O. Shemmer und S. Veilleux, *ApJ* **684** (2008), 853.
- [158] W. Maciejewski, *MNRAS* **354** (2004), 892.
- [159] P. Madau, *arXiv:astro-ph/9812087* (1998).
- [160] P. Madau, L. Pozzetti und M. Dickinson, *ApJ* **498** (1998), 106.
- [161] B. Magnelli, D. Elbaz, R.R. Chary, M. Dickinson, D. Le Borgne, D.T. Frayer und C.N.A. Willmer, *A&A* **496** (2009), 57.
- [162] B. Magnelli, D. Elbaz, R.R. Chary, M. Dickinson, D. Le Borgne, D.T. Frayer und C.N.A. Willmer, *VizieR Online Data Catalog* **352** (2011), 89035.
- [163] V. Mainieri, P. Rosati, P. Tozzi, J. Bergeron, R. Gilli, G. Hasinger, M. Nonino, I. Lehmann, D.M. Alexander, R. Idzi, A.M. Koekemoer, C. Norman, G. Szokoly und W. Zheng, *A&A* **437** (2005), 805.
- [164] R. Maiolino, O. Shemmer, M. Imanishi, H. Netzer, E. Oliva, D. Lutz und E. Sturm, *A&A* **468** (2007), 979.
- [165] M.A. Malkan, V. Gorjian und R. Tam, *ApJS* **117** (1998), 25.
- [166] A. Marconi und L.K. Hunt, *ApJ* **589** (2003), L21.
- [167] A. Marconi, G. Risaliti, R. Gilli, L.K. Hunt, R. Maiolino und M. Salvati, *MNRAS* **351** (2004), 169.
- [168] P. Martini, M.W. Regan, J.S. Mulchaey und R.W. Pogge, *ApJ* **589** (2003), 774.

- [169] S.E. Meidt, E. Schinnerer, J.H. Knapen, A. Bosma, E. Athanassoula, K. Sheth, R.J. Buta, D. Zaritsky, E. Laurikainen, D. Elmegreen, B.G. Elmegreen, D.A. Gadotti, H. Salo, M. Regan, L.C. Ho, B.F. Madore, J.L. Hinz, R.A. Skibba, A. Gil de Paz, J.C. Muñoz-Mateos, K. Menéndez-Delmestre, M. Seibert, T. Kim, T. Mizusawa, J. Laine und S. Comerón, *ApJ* **744** (2012), 17.
- [170] M. Meléndez, S.B. Kraemer, B.K. Armentrout, R.P. Deo, D.M. Crenshaw, H.R. Schmitt, R.F. Mushotzky, J. Tueller, C.B. Markwardt und L. Winter, *ApJ* **682** (2008), 94.
- [171] J.S. Miller und R.W. Goodrich, *ApJ* **355** (1990), 456.
- [172] H.J. Mo, S. Mao und S.D.M. White, *MNRAS* **295** (1998), 319.
- [173] M. Moshir, G. Kopman und T.A.O. Conrow: *IRAS Faint Source Survey, Explanatory supplement version 2*, 1992.
- [174] J.R. Mullaney, D.M. Alexander, A.D. Goulding und R.C. Hickox, *MNRAS* **414** (2011), 1082.
- [175] J.R. Mullaney, D.M. Alexander, M. Huynh, A.D. Goulding und D. Frayer, *MNRAS* **401** (2010), 995.
- [176] F. Müller Sánchez, R.I. Davies, R. Genzel, L.J. Tacconi, F. Eisenhauer, E.K.S. Hicks, S. Friedrich und A. Sternberg, *ApJ* **691** (2009), 749.
- [177] K. Nandra, A. Georgakakis, C.N.A. Willmer, M.C. Cooper, D.J. Croton, M. Davis, S.M. Faber, D.C. Koo, E.S. Laird und J.A. Newman, *ApJ* **660** (2007), L11.
- [178] K. Nandra, T. Le, I.M. George, R.A. Edelson, R.F. Mushotzky, B.M. Peterson und T.J. Turner, *ApJ* **544** (2000), 734.
- [179] R. Narayan und I. Yi, *ApJ* **452** (1995), 710.
- [180] J. Negroponte und S.D.M. White, *MNRAS* **205** (1983), 1009.
- [181] H. Netzer, *MNRAS* **399** (2009), 1907.
- [182] H. Netzer, D. Lutz, M. Schweitzer, A. Contursi, E. Sturm, L.J. Tacconi, S. Veilleux, D.C. Kim, D. Rupke, A.J. Baker, K. Dasyra, J. Mazzarella und S. Lord, *ApJ* **666** (2007), 806.
- [183] H. Netzer, V. Mainieri, P. Rosati und B. Trakhtenbrot, *A&A* **453** (2006), 525.
- [184] H. Netzer und B. Trakhtenbrot, *ApJ* **654** (2007), 754.

- [185] G. Neugebauer, H.J. Habing, R. van Duinen, H.H. Aumann, B. Baud, C.A. Beichman, D.A. Beintema, N. Boggess, P.E. Clegg, T. de Jong, J.P. Emerson, T.N. Gautier, F.C. Gillett, S. Harris, M.G. Hauser, J.R. Houck, R.E. Jennings, F.J. Low, P.L. Marsden, G. Miley, F.M. Oton, S.R. Pottasch, E. Raimond, M. Rowan-Robinson, B.T. Soifer, R.G. Walker, P.R. Wesselius und E. Young, *ApJ* **278** (1984), L1.
- [186] K.G. Noeske, B.J. Weiner, S.M. Faber, C. Papovich, D.C. Koo, R.S. Somerville, K. Bundy, C.J. Conselice, J.A. Newman, D. Schiminovich, E. Le Floch, A.L. Coil, G.H. Rieke, J.M. Lotz, J.R. Primack, P. Barmby, M.C. Cooper, M. Davis, R.S. Ellis, G.G. Fazio, P. Guhathakurta, J. Huang, S.A. Kassin, D.C. Martin, A.C. Phillips, R.M. Rich, T.A. Small, C.N.A. Willmer und G. Wilson, *ApJ* **660** (2007), L43.
- [187] C. Norman und N. Scoville, *ApJ* **332** (1988), 124.
- [188] G. Orban de Xivry, R. Davies, M. Schartmann, S. Komossa, A. Marconi, E. Hicks, H. Engel und L. Tacconi, *MNRAS* **417** (2011), 2721.
- [189] D.E. Osterbrock, *ApJ* **215** (1977), 733.
- [190] D.E. Osterbrock: *Astrophysics of gaseous nebulae and active galactic nuclei*, 1989.
- [191] M.J. Page, J.A. Stevens, R.J. Ivison und F.J. Carrera, *ApJ* **611** (2004), L85.
- [192] M.J. Page, J.A. Stevens, J.P.D. Mittaz und F.J. Carrera, *Science* **294** (2001), 2516.
- [193] F. Panessa, L. Bassani, M. Cappi, M. Dadina, X. Barcons, F.J. Carrera, L.C. Ho und K. Iwasawa, *A&A* **455** (2006), 173.
- [194] A. Pappa, I. Georgantopoulos, G.C. Stewart und A.L. Zezas, *MNRAS* **326** (2001), 995.
- [195] B.M. Peterson, L. Ferrarese, K.M. Gilbert, S. Kaspi, M.A. Malkan, D. Maoz, D. Merritt, H. Netzer, C.A. Onken, R.W. Pogge, M. Vestergaard und A. Wandel, *ApJ* **613** (2004), 682.
- [196] B.M. Peterson und K. Horne, *Astronomische Nachrichten* **325** (2004), 248.
- [197] G.L. Pilbratt, J.R. Riedinger, T. Passvogel, G. Crone, D. Doyle, U. Gageur, A.M. Heras, C. Jewell, L. Metcalfe, S. Ott und M. Schmidt, *A&A* **518** (2010), L1.
- [198] A. Poglitsch, C. Waelkens, N. Geis, H. Feuchtgruber, B. Vandenbussche, L. Rodriguez, O. Krause, E. Renotte, C. van Hoof, P. Saraceno, J. Cepa, F. Kerschbaum, P. Agnèse, B. Ali, B. Altieri, P. Andreani, J.L. Augeres, Z. Balog, L. Barl, O.H. Bauer, N. Belbachir, M. Benedettini, N. Billot, O. Boulade, H. Bischof, J. Blommaert, E. Callut, C. Cara, R. Cerulli, D. Cesarsky, A. Contursi, Y. Creten, W. De Meester, V. Doublier, E. Doumayrou, L. Duband, K. Exter, R. Genzel, J.M. Gillis,

- U. Grözinger, T. Henning, J. Herreros, R. Huygen, M. Inguscio, G. Jakob, C. Jamar, C. Jean, J. de Jong, R. Katterloher, C. Kiss, U. Klaas, D. Lemke, D. Lutz, S. Madden, B. Marquet, J. Martignac, A. Mazy, P. Merken, F. Montfort, L. Morbidelli, T. Müller, M. Nielbock, K. Okumura, R. Orfei, R. Ottensamer, S. Pezzuto, P. Popesso, J. Putzeys, S. Regibo, V. Reveret, P. Royer, M. Sauvage, J. Schreiber, J. Stegmaier, D. Schmitt, J. Schubert, E. Sturm, M. Thiel, G. Tofani, R. Vavrek, M. Wetzstein, E. Wieprecht und E. Wiezorrek, *A&A* **518** (2010), L2.
- [199] M. Polletta, M. Tajer, L. Maraschi, G. Trinchieri, C.J. Lonsdale, L. Chiappetti, S. Andreon, M. Pierre, O. Le Fèvre, G. Zamorani, D. Maccagni, O. Garcet, J. Surdej, A. Franceschini, D. Alloin, D.L. Shupe, J.A. Surace, F. Fang, M. Rowan-Robinson, H.E. Smith und L. Tresse, *ApJ* **663** (2007), 81.
- [200] D.A. Rafferty, B.R. McNamara, P.E.J. Nulsen und M.W. Wise, *ApJ* **652** (2006), 216.
- [201] J.A. Rich, P. Torrey, L.J. Kewley, M.A. Dopita und D.S.N. Rupke, *ApJ* **753** (2012), 5.
- [202] G.T. Richards, N.E. Kruczek, S.C. Gallagher, P.B. Hall, P.C. Hewett, K.M. Leighly, R.P. Deo, R.M. Kratzer und Y. Shen, *AJ* **141** (2011), 167.
- [203] G.T. Richards, M. Lacy, L.J. Storrie-Lombardi, P.B. Hall, S.C. Gallagher, D.C. Hines, X. Fan, C. Papovich, D.E. Vanden Berk, G.B. Trammell, D.P. Schneider, M. Vestergaard, D.G. York, S. Jester, S.F. Anderson, T. Budavári und A.S. Szalay, *ApJS* **166** (2006), 470.
- [204] G.T. Richards, D.E. Vanden Berk, T.A. Reichard, P.B. Hall, D.P. Schneider, M. SubbaRao, A.R. Thakar und D.G. York, *AJ* **124** (2002), 1.
- [205] G. Rodighiero, C. Gruppioni, F. Civano, A. Comastri, A. Franceschini, M. Mignoli, J. Fritz, C. Vignali und T. Treu, *MNRAS* **376** (2007), 416.
- [206] D.J. Rosario, M. Mozena, S. Wuyts, K. Nandra, A. Koekemoer, E. McGrath, N.P. Hathi, A. Dekel, J. Donley, J.S. Dunlop, S.M. Faber, H. Ferguson, M. Giavalisco, N. Grogin, Y. Guo, D.D. Kocevski, D.C. Koo, E. Laird, J. Newman, C. Rangel und R. Somerville, *ApJ* **763** (2013), 59.
- [207] D.J. Rosario, P. Santini, D. Lutz, L. Shao, R. Maiolino, D.M. Alexander, B. Altieri, P. Andreani, H. Aussel, F.E. Bauer, S. Berta, A. Bongiovanni, W.N. Brandt, M. Brusa, J. Cepa, A. Cimatti, T.J. Cox, E. Daddi, D. Elbaz, A. Fontana, N.M. Förster Schreiber, R. Genzel, A. Grazian, E. Le Floch, B. Magnelli, V. Mainieri, H. Netzer, R. Nordon, I. Pérez Garcia, A. Poglitsch, P. Popesso, F. Pozzi, L. Riguccini, G. Rodighiero, M. Salvato, M. Sanchez-Portal, E. Sturm, L.J. Tacconi, I. Valtchanov und S. Wuyts, *A&A* **545** (2012), A45.

- [208] P. Rosati, P. Tozzi, R. Giacconi, R. Gilli, G. Hasinger, L. Kewley, V. Mainieri, M. Nonino, C. Norman, G. Szokoly, J.X. Wang, A. Zirm, J. Bergeron, S. Borgani, R. Gilmozzi, N. Grogin, A. Koekemoer, E. Schreier und W. Zheng, *ApJ* **566** (2002), 667.
- [209] M. Rowan-Robinson, *MNRAS* **272** (1995), 737.
- [210] S. Salim, R.M. Rich, S. Charlot, J. Brinchmann, B.D. Johnson, D. Schiminovich, M. Seibert, R. Mallery, T.M. Heckman, K. Forster, P.G. Friedman, D.C. Martin, P. Morrissey, S.G. Neff, T. Small, T.K. Wyder, L. Bianchi, J. Donas, Y.W. Lee, B.F. Madore, B. Milliard, A.S. Szalay, B.Y. Welsh und S.K. Yi, *ApJS* **173** (2007), 267.
- [211] D.B. Sanders, *Ap&SS* **266** (1999), 331.
- [212] D.B. Sanders, B.T. Soifer, J.H. Elias, B.F. Madore, K. Matthews, G. Neugebauer und N.Z. Scoville, *ApJ* **325** (1988), 74.
- [213] K. Schawinski, C.M. Urry, S. Virani, P. Coppi, S.P. Bamford, E. Treister, C.J. Lintott, M. Sarzi, W.C. Keel, S. Kaviraj, C.N. Cardamone, K.L. Masters, N.P. Ross, D. Andreescu, P. Murray, R.C. Nichol, M.J. Raddick, A. Slosar, A.S. Szalay, D. Thomas und J. Vandenberg, *ApJ* **711** (2010), 284.
- [214] M. Schmidt und R.F. Green, *ApJ* **269** (1983), 352.
- [215] D.P. Schneider, G.T. Richards, P.B. Hall, M.A. Strauss, S.F. Anderson, T.A. Boroson, N.P. Ross, Y. Shen, W.N. Brandt, X. Fan, N. Inada, S. Jester, G.R. Knapp, C.M. Krawczyk, A.R. Thakar, D.E. Vanden Berk, W. Voges, B. Yanny, D.G. York, N.A. Bahcall, D. Bizyaev, M.R. Blanton, H. Brewington, J. Brinkmann, D. Eisenstein, J.A. Frieman, M. Fukugita, J. Gray, J.E. Gunn, P. Hibon, Ž. Ivezić, S.M. Kent, R.G. Kron, M.G. Lee, R.H. Lupton, E. Malanushenko, V. Malanushenko, D. Oravetz, K. Pan, J.R. Pier, T.N. Price, III, D.H. Saxe, D.J. Schlegel, A. Simmons, S.A. Snedden, M.U. SubbaRao, A.S. Szalay und D.H. Weinberg, *AJ* **139** (2010), 2360.
- [216] K. Schwarzschild, *Abh. Konigl. Preuss. Akad. Wissenschaften Jahre 1906,92, Berlin,1907* (1916), 189.
- [217] M. Schweitzer, D. Lutz, E. Sturm, A. Contursi, L.J. Tacconi, M.D. Lehnert, K.M. Dasyra, R. Genzel, S. Veilleux, D. Rupke, D.C. Kim, A.J. Baker, H. Netzer, A. Sternberg, J. Mazzarella und S. Lord, *ApJ* **649** (2006), 79.
- [218] P. Severgnini, R. Maiolino, M. Salvati, D. Axon, A. Cimatti, F. Fiore, R. Gilli, F. La Franca, A. Marconi, G. Matt, G. Risaliti und C. Vignali, *A&A* **360** (2000), 457.
- [219] C.K. Seyfert, *ApJ* **97** (1943), 28.
- [220] N.I. Shakura und R.A. Sunyaev, *A&A* **24** (1973), 337.

- [221] Z. Shang, M.S. Brotherton, R.F. Green, G.A. Kriss, J. Scott, J.K. Quijano, O. Blaes, I. Hubeny, J. Hutchings, M.E. Kaiser, A. Koratkar, W. Oegerle und W. Zheng, *ApJ* **619** (2005), 41.
- [222] Y. Shen, G.T. Richards, M.A. Strauss, P.B. Hall, D.P. Schneider, S. Snedden, D. Bizyaev, H. Brewington, V. Malanushenko, E. Malanushenko, D. Oravetz, K. Pan und A. Simmons, *ApJS* **194** (2011), 45.
- [223] J. Silk und M.J. Rees, *A&A* **331** (1998), L1.
- [224] J.D. Silverman, P. Kampczyk, K. Jahnke, R. Andrae, S.J. Lilly, M. Elvis, F. Civano, V. Mainieri, C. Vignali, G. Zamorani, P. Nair, O. Le Fèvre, L. de Ravel, S. Bardelli, A. Bongiorno, M. Bolzonella, A. Cappi, K. Caputi, C.M. Carollo, T. Contini, G. Coppa, O. Cucciati, S. de la Torre, P. Franzetti, B. Garilli, C. Halliday, G. Hasinger, A. Iovino, C. Knobel, A.M. Koekemoer, K. Kovač, F. Lamareille, J.F. Le Borgne, V. Le Brun, C. Maier, M. Mignoli, R. Pello, E. Pérez-Montero, E. Ricciardelli, Y. Peng, M. Scodreggio, M. Tanaka, L. Tasca, L. Tresse, D. Vergani, E. Zucca, M. Brusa, N. Cappelluti, A. Comastri, A. Finoguenov, H. Fu, R. Gilli, H. Hao, L.C. Ho und M. Salvato, *ApJ* **743** (2011), 2.
- [225] J.D. Silverman, F. Lamareille, C. Maier, S.J. Lilly, V. Mainieri, M. Brusa, N. Cappelluti, G. Hasinger, G. Zamorani, M. Scodreggio, M. Bolzonella, T. Contini, C.M. Carollo, K. Jahnke, J.P. Kneib, O. Le Fèvre, A. Merloni, S. Bardelli, A. Bongiorno, H. Brunner, K. Caputi, F. Civano, A. Comastri, G. Coppa, O. Cucciati, S. de la Torre, L. de Ravel, M. Elvis, A. Finoguenov, F. Fiore, P. Franzetti, B. Garilli, R. Gilli, A. Iovino, P. Kampczyk, C. Knobel, K. Kovač, J.F. Le Borgne, V. Le Brun, M. Mignoli, R. Pello, Y. Peng, E. Perez Montero, E. Ricciardelli, M. Tanaka, L. Tasca, L. Tresse, D. Vergani, C. Vignali, E. Zucca, D. Bottini, A. Cappi, P. Cassata, M. Fumana, R. Griffiths, J. Kartaltepe, A. Koekemoer, C. Marinoni, H.J. McCracken, P. Memeo, B. Meneux, P. Oesch, C. Porciani und M. Salvato, *ApJ* **696** (2009), 396.
- [226] C. Simpson, *MNRAS* **360** (2005), 565.
- [227] M.F. Skrutskie, R.M. Cutri, R. Stiening, M.D. Weinberg, S. Schneider, J.M. Carpenter, C. Beichman, R. Capps, T. Chester, J. Elias, J. Huchra, J. Liebert, C. Lonsdale, D.G. Monet, S. Price, P. Seitzer, T. Jarrett, J.D. Kirkpatrick, J.E. Gizis, E. Howard, T. Evans, J. Fowler, L. Fullmer, R. Hurt, R. Light, E.L. Kopan, K.A. Marsh, H.L. McCallon, R. Tam, S. Van Dyk und S. Wheelock, *AJ* **131** (2006), 1163.
- [228] B.T. Soifer, G. Helou und M. Werner, *ARA&A* **46** (2008), 201.
- [229] A. Soltan, *MNRAS* **200** (1982), 115.
- [230] V. Springel, *MNRAS* **312** (2000), 859.
- [231] V. Springel, T. Di Matteo und L. Hernquist, *MNRAS* **361** (2005), 776.

- [232] D. Stern, R.J. Assef, D.J. Benford, A. Blain, R. Cutri, A. Dey, P. Eisenhardt, R.L. Griffith, T.H. Jarrett, S. Lake, F. Masci, S. Petty, S.A. Stanford, C.W. Tsai, E.L. Wright, L. Yan, F. Harrison und K. Madsen, *ApJ* **753** (2012), 30.
- [233] D. Stern, P. Eisenhardt, V. Gorjian, C.S. Kochanek, N. Caldwell, D. Eisenstein, M. Brodwin, M.J.I. Brown, R. Cool, A. Dey, P. Green, B.T. Jannuzi, S.S. Murray, M.A. Pahre und S.P. Willner, *ApJ* **631** (2005), 163.
- [234] J.A. Stevens, M.J. Page, R.J. Ivison, F.J. Carrera, J.P.D. Mittaz, I. Smail und I.M. McHardy, *MNRAS* **360** (2005), 610.
- [235] T. Storchi-Bergmann, O.L. Dors, Jr., R.A. Riffel, K. Fathi, D.J. Axon, A. Robinson, A. Marconi und G. Östlin, *ApJ* **670** (2007), 959.
- [236] T. Storchi-Bergmann, R.D.S. Lopes, P.J. McGregor, R.A. Riffel, T. Beck und P. Martini, *MNRAS* **402** (2010), 819.
- [237] L.J. Tacconi, R. Genzel, R. Neri, P. Cox, M.C. Cooper, K. Shapiro, A. Bolatto, N. Bouché, F. Bournaud, A. Burkert, F. Combes, J. Comerford, M. Davis, N.M.F. Schreiber, S. García-Burillo, J. Gracia-Carpio, D. Lutz, T. Naab, A. Omont, A. Shapley, A. Sternberg und B. Weiner, *Nature* **463** (2010), 781.
- [238] L.J. Tacconi, R. Neri, R. Genzel, F. Combes, A. Bolatto, M.C. Cooper, S. Wuyts, F. Bournaud, A. Burkert, J. Comerford, P. Cox, M. Davis, N.M. Förster Schreiber, S. García-Burillo, J. Gracia-Carpio, D. Lutz, T. Naab, S. Newman, A. Omont, A. Saintonge, K. Shapiro Griffin, A. Shapley, A. Sternberg und B. Weiner, *ApJ* **768** (2013), 74.
- [239] C. Tasse, P.N. Best, H. Röttgering und D. Le Borgne, *A&A* **490** (2008), 893.
- [240] M. Tegmark, M.A. Strauss, M.R. Blanton, K. Abazajian, S. Dodelson, H. Sandvik, X. Wang, D.H. Weinberg, I. Zehavi, N.A. Bahcall, F. Hoyle, D. Schlegel, R. Scoccimarro, M.S. Vogeley, A. Berlind, T. Budavari, A. Connolly, D.J. Eisenstein, D. Finkbeiner, J.A. Frieman, J.E. Gunn, L. Hui, B. Jain, D. Johnston, S. Kent, H. Lin, R. Nakajima, R.C. Nichol, J.P. Ostriker, A. Pope, R. Scranton, U. Seljak, R.K. Sheth, A. Stebbins, A.S. Szalay, I. Szapudi, Y. Xu, J. Annis, J. Brinkmann, S. Burles, F.J. Castander, I. Csabai, J. Loveday, M. Doi, M. Fukugita, B. Gillespie, G. Hennessy, D.W. Hogg, Ž. Ivezić, G.R. Knapp, D.Q. Lamb, B.C. Lee, R.H. Lupton, T.A. McKay, P. Kunszt, J.A. Munn, L. O’Connell, J. Peoples, J.R. Pier, M. Richmond, C. Rockosi, D.P. Schneider, C. Stoughton, D.L. Tucker, D.E. vanden Berk, B. Yanny und D.G. York, *Phys. Rev. D* **69** (2004), 103501.
- [241] H.D. Tran, J.S. Miller und L.E. Kay, *ApJ* **397** (1992), 452.
- [242] Q.D. Tran, D. Lutz, R. Genzel, D. Rigopoulou, H.W.W. Spoon, E. Sturm, M. Gerin, D.C. Hines, A.F.M. Moorwood, D.B. Sanders, N. Scoville, Y. Taniguchi und M. Ward, *ApJ* **552** (2001), 527.

- [243] E. Treister, C.M. Urry und S. Virani, *ApJ* **696** (2009), 110.
- [244] S. Tremaine, K. Gebhardt, R. Bender, G. Bower, A. Dressler, S.M. Faber, A.V. Filippenko, R. Green, C. Grillmair, L.C. Ho, J. Kormendy, T.R. Lauer, J. Magorrian, J. Pinkney und D. Richstone, *ApJ* **574** (2002), 740.
- [245] K.R.W. Tristram, K. Meisenheimer, W. Jaffe, M. Schartmann, H.W. Rix, C. Leinert, S. Morel, M. Wittkowski, H. Röttgering, G. Perrin, B. Lopez, D. Raban, W.D. Cotton, U. Graser, F. Paresce und T. Henning, *A&A* **474** (2007), 837.
- [246] K.R.W. Tristram, D. Raban, K. Meisenheimer, W. Jaffe, H. Röttgering, L. Burtscher, W.D. Cotton, U. Graser, T. Henning, C. Leinert, B. Lopez, S. Morel, G. Perrin und M. Wittkowski, *A&A* **502** (2009), 67.
- [247] L. Trouille und A.J. Barger, *ApJ* **722** (2010), 212.
- [248] J.R. Trump, C.D. Impey, B.C. Kelly, F. Civano, J.M. Gabor, A.M. Diamond-Stanic, A. Merloni, C.M. Urry, H. Hao, K. Jahnke, T. Nagao, Y. Taniguchi, A.M. Koeke-moer, G. Lanzuisi, C. Liu, V. Mainieri, M. Salvato und N.Z. Scoville, *ApJ* **733** (2011), 60.
- [249] J. Tueller, W.H. Baumgartner, C.B. Markwardt, G.K. Skinner, R.F. Mushotzky, M. Ajello, S. Barthelmy, A. Beardmore, W.N. Brandt, D. Burrows, G. Chincarini, S. Campana, J. Cummings, G. Cusumano, P. Evans, E. Fenimore, N. Gehrels, O. Godet, D. Grupe, S. Holland, J. Kennea, H.A. Krimm, M. Koss, A. Moretti, K. Mukai, J.P. Osborne, T. Okajima, C. Pagani, K. Page, D. Palmer, A. Parsons, D.P. Schneider, T. Sakamoto, R. Sambruna, G. Sato, M. Stamatikos, M. Stroh, T. Ukwata und L. Winter, *ApJS* **186** (2010), 378.
- [250] T.J. Turner und L. Miller, *A&A Rev.* **17** (2009), 47.
- [251] Y. Ueda, M. Akiyama, K. Ohta und T. Miyaji, *ApJ* **598** (2003), 886.
- [252] C.M. Urry und P. Padovani, *PASP* **107** (1995), 803.
- [253] S. Veilleux, *ApJS* **75** (1991), 383.
- [254] S. Veilleux, D.C. Kim, D.S.N. Rupke, C.Y. Peng, L.J. Tacconi, R. Genzel, D. Lutz, E. Sturm, A. Contursi, M. Schweitzer, K.M. Dasyra, L.C. Ho, D.B. Sanders und A. Burkert, *ApJ* **701** (2009), 587.
- [255] S. Veilleux und D.E. Osterbrock, *ApJS* **63** (1987), 295.
- [256] A. von der Linden, V. Wild, G. Kauffmann, S.D.M. White und S. Weinmann, *MNRAS* **404** (2010), 1231.
- [257] A. Wandel, B.M. Peterson und M.A. Malkan, *ApJ* **526** (1999), 579.

- [258] T.J. Waskett, S.A. Eales, W.K. Gear, E.M. Puchnarewicz, S. Lilly, H. Flores, T. Webb, D. Clements, J.A. Stevens und T.X. Thuan, *MNRAS* **341** (2003), 1217.
- [259] M.C. Weisskopf, H.D. Tananbaum, L.P. Van Speybroeck und S.L. O'Dell: *Chandra X-ray Observatory (CXO): overview*. *Chandra X-ray Observatory (CXO): overview*, In *Society of Photo-Optical Instrumentation Engineers (SPIE) Conference Series*, herausgegeben von J. E. Truemper und B. Aschenbach, Band 4012 von *Society of Photo-Optical Instrumentation Engineers (SPIE) Conference Series*. (Juli 2000) Seiten 2–16.
- [260] V. Wild, G. Kauffmann, T. Heckman, S. Charlot, G. Lemson, J. Brinchmann, T. Reichard und A. Pasquali, *MNRAS* **381** (2007), 543.
- [261] D.F. Woods und M.J. Geller, *AJ* **134** (2007), 527.
- [262] D.F. Woods, M.J. Geller und E.J. Barton, *AJ* **132** (2006), 197.
- [263] E.L. Wright, P.R.M. Eisenhardt, A.K. Mainzer, M.E. Ressler, R.M. Cutri, T. Jarrett, J.D. Kirkpatrick, D. Padgett, R.S. McMillan, M. Skrutskie, S.A. Stanford, M. Cohen, R.G. Walker, J.C. Mather, D. Leisawitz, T.N. Gautier, III, I. McLean, D. Benford, C.J. Lonsdale, A. Blain, B. Mendez, W.R. Irace, V. Duval, F. Liu, D. Royer, I. Heinrichsen, J. Howard, M. Shannon, M. Kendall, A.L. Walsh, M. Larsen, J.G. Cardon, S. Schick, M. Schwalm, M. Abid, B. Fabinsky, L. Naes und C.W. Tsai, *AJ* **140** (2010), 1868.
- [264] Y.Q. Xue, W.N. Brandt, B. Luo, D.A. Rafferty, D.M. Alexander, F.E. Bauer, B.D. Lehmer, D.P. Schneider und J.D. Silverman, *ApJ* **720** (2010), 368.
- [265] Y.Q. Xue, B. Luo, W.N. Brandt, F.E. Bauer, B.D. Lehmer, P.S. Broos, D.P. Schneider, D.M. Alexander, M. Brusa, A. Comastri, A.C. Fabian, R. Gilli, G. Hasinger, A.E. Hornschemeier, A. Koekemoer, T. Liu, V. Mainieri, M. Paolillo, D.A. Rafferty, P. Rosati, O. Shemmer, J.D. Silverman, I. Smail, P. Tozzi und C. Vignali, *ApJS* **195** (2011), 10.
- [266] R. Yan und M.R. Blanton, *ApJ* **747** (2012), 61.
- [267] D.G. York, J. Adelman, J.E. Anderson, Jr., S.F. Anderson, J. Annis, N.A. Bahcall, J.A. Bakken, R. Barkhouser, S. Bastian, E. Berman, W.N. Boroski, S. Bracker, C. Briegel, J.W. Briggs, J. Brinkmann, R. Brunner, S. Burles, L. Carey, M.A. Carr, F.J. Castander, B. Chen, P.L. Colestock, A.J. Connolly, J.H. Crocker, I. Csabai, P.C. Czarapata, J.E. Davis, M. Doi, T. Dombeck, D. Eisenstein, N. Ellman, B.R. Elms, M.L. Evans, X. Fan, G.R. Federwitz, L. Fiscelli, S. Friedman, J.A. Frieman, M. Fukugita, B. Gillespie, J.E. Gunn, V.K. Gurbani, E. de Haas, M. Halderman, F.H. Harris, J. Hayes, T.M. Heckman, G.S. Hennessy, R.B. Hindsley, S. Holm, D.J. Holmgren, C.h. Huang, C. Hull, D. Husby, S.I. Ichikawa, T. Ichikawa,

- Ž. Ivezić, S. Kent, R.S.J. Kim, E. Kinney, M. Klaene, A.N. Kleinman, S. Kleinman, G.R. Knapp, J. Korienek, R.G. Kron, P.Z. Kunszt, D.Q. Lamb, B. Lee, R.F. Leger, S. Limmongkol, C. Lindenmeyer, D.C. Long, C. Loomis, J. Loveday, R. Lucinio, R.H. Lupton, B. MacKinnon, E.J. Mannery, P.M. Mantsch, B. Margon, P. McGehee, T.A. McKay, A. Meiksin, A. Merelli, D.G. Monet, J.A. Munn, V.K. Narayanan, T. Nash, E. Neilsen, R. Neswold, H.J. Newberg, R.C. Nichol, T. Nicinski, M. Nonino, N. Okada, S. Okamura, J.P. Ostriker, R. Owen, A.G. Pauls, J. Peoples, R.L. Peterson, D. Petravick, J.R. Pier, A. Pope, R. Pordes, A. Protopio, R. Rechenmacher, T.R. Quinn, G.T. Richards, M.W. Richmond, C.H. Rivetta, C.M. Rockosi, K. Ruthmansdorfer, D. Sandford, D.J. Schlegel, D.P. Schneider, M. Sekiguchi, G. Sergey, K. Shimasaku, W.A. Siegmund, S. Smee, J.A. Smith, S. Snedden, R. Stone, C. Stoughton, M.A. Strauss, C. Stubbs, M. SubbaRao, A.S. Szalay, I. Szapudi, G.P. Szokoly, A.R. Thakar, C. Tremonti, D.L. Tucker, A. Uomoto, D. Vanden Berk, M.S. Vogeley, P. Waddell, S.i. Wang, M. Watanabe, D.H. Weinberg, B. Yanny, N. Yasuda und SDSS Collaboration, *AJ* **120** (2000), 1579.
- [268] S. Young, D.J. Axon, A. Robinson, J.H. Hough und J.E. Smith, *Nature* **450** (2007), 74.
- [269] T.T. Yuan, L.J. Kewley und D.B. Sanders, *ApJ* **709** (2010), 884.
- [270] N.L. Zakamska, M.A. Strauss, J.H. Krolik, M.J. Collinge, P.B. Hall, L. Hao, T.M. Heckman, Ž. Ivezić, G.T. Richards, D.J. Schlegel, D.P. Schneider, I. Strateva, D.E. Vanden Berk, S.F. Anderson und J. Brinkmann, *AJ* **126** (2003), 2125.

Thanks

This thesis is finished under the advise of Dr. Guinevere Kauffmann and Dr. Cheng Li. Their scientific guide is essential to finally accomplish this work. They spent a lot of time to discuss with me, help me refine the results, and teach me how to do good scientific work. I learned a lot and I think these will still help me in future. I am glad to have such great advisers. I will never forget the days in Shanghai and later in Munich, working on *SDSS* and *WISE* data, under their kind support. I would like to thank them for their invaluable help during the past years, especially my hard days in 2011. I believe without their help this thesis will never be finished.

I thank Prof. Simon White to be the first supervisor of my thesis and the chair of my thesis committee. He kindly helps me a lot to submit this thesis to the University. I also thank for his very useful comments to my work during my Ph.D. study.

I thank Dr. Dieter Lutz for advising me during my study in MPE. I learned a lot about IR astronomy, which was totally new to me. It was good experience to get my first paper with him. That work is an important part of this thesis. By joining his group in MPE, I came to Munich. That is an important milestone in my life.

I thank my collaborator Prof. Timothy Heckman for kindly providing many good suggestions for my second paper. Our face-to-face discussion in Leiden was nice experience.

I thank my friends and collaborators in MPE, Paola Popesso and Stefano Berta. I really enjoy their friendship and their support to my first work. I also thank the other collaborators during my stay in MPE, Raanan Nordon, Benjamin Magnelli, Amélie Saintonge, Javier Graciá Carpio, Paola Santini, Linda Tacconi and Reinhard Genzel.

I thank my colleague Thorsten Naab, who is a native German speaker, for helping me to translate my English abstract into German.

I thank the secretaries in MPA and MPE, especially Mrs. Gabriele Kratschmann. I may not survive the days in Munich without their great help.

Finally I thank my family who always support me. My parents, and my wife Jing Wang helped me a lot to overcome many difficulties during my Ph.D. study. I would like to make this thesis as the best gift to them. This is also the best present to my newborn baby Yunya. Her birth in 2013 summer, the last months of my Ph.D. study, has given me great joy.

Curriculum Vitae

Personal

Name: Li Shao

Gender: Male

Date of birth: 23.09.1982

Place of birth: Hangzhou, China

Address: Karl-Schwarszchild-Str. 1, Garching, 85748, Germany

Office Phone: +49-89-300002179

Email: lishao@mpa-garching.mpg.de

Education

- 10.2009 – present Ph.D., Department of Physics, Ludwig Maximilians University, Munich, Germany.
- 09.2005 – 07.2008 Department of Physics, Tsinghua University, Beijing, China.
M.S., “*Eight years of monitoring blazar PKS 2155-304 with XMM-Newton: Spectral variation analysis*”
- 09.2003 – 07.2005 Department of Physics, Tsinghua University, Beijing, China.
B.S., “*The luminosity function and distribution of gamma-ray bursts*”
- 09.2001 – 08.2003 Department of Engineering Mechanics, Tsinghua University, Beijing, China.

Work Experience

- 01.2012 – present Student, Max Planck Institute for Astrophysics, Garching, Germany.
- 04.2011 – 12.2011 Visiting student, Shanghai Astronomical Observatory, Shanghai, China.
- 09.2008 – 10.2010 Student, Max Planck Institute for Extraterrestrial Physics, Garching, Germany.

Award

- 11.2007 Graduate student scholarship, Tsinghua University, Beijing, China.

Publications

1. **L. Shao**, G. Kauffmann, C. Li, et al., “The nature of obscuration in AGN: I. Insights from host galaxies”, 2013, MNRAS, in press.[†]
2. **L. Shao**, D. Lutz, R. Nordon, et al., “Star formation in AGN hosts in GOODS-N”, 2010, A&A, 518, L26.[†]
3. **L. Shao**, C. Li, G. Kauffmann et al., “The nature of obscuration in AGN: II. Insights from clustering properties”, in preparation.[†]
4. D. Rosario, P. Santini, D. Lutz, **L. Shao**, et al., “The mean star formation rate of X-ray selected active galaxies and its evolution from $z \sim 2.5$: results from PEP-Herschel”, 2012, A&A, 545, A45.
5. P. Santini, D. Rosario, **L. Shao**, et al., “Enhanced star formation rates in AGN hosts with respect to inactive galaxies from PEP-Herschel observations”, 2012, A&A, 540, A109.
6. R. Nordon, D. Lutz, **L. Shao**, et al., “The star-formation rates of $1.5 < z < 2.5$ massive galaxies”, 2010, A&A, 518, L24.
7. D. Lutz, V. Mainieri, D. Rafferty, **L. Shao**, et al., “The LABOCA Survey of the Extended Chandra Deep Field South: Two Modes of Star Formation in Active Galactic Nucleus Hosts?”, 2010, AJ, 712, 1287.
8. Y. Zhang, Z. Hou, **L. Shao**, et al., “Discovery of a high confidence soft lag from an X-ray flare of Markarian 421”, 2010, Science in China G: Physics and Astronomy, 53, 224.

And other 15 publications as co-author.

†: content used in the thesis.

Conferences

1. “IAU S304: Multiwavelength AGN Surveys and Studies”, 10.2013, Yerevan, Armenia (15 min talk).
2. “Gas, Stars, and Black Holes in the Galaxy Ecosystem”, 07.2012, Leiden, Netherlands, (poster).
3. “The 9th Sino-German Workshop on Galaxy Formation and Cosmology”, 04.2011, Hangzhou, China (15 min talk).
4. “Galaxy Evolution: Infrared to Millimeter Wavelength Perspective”, 10.2010, Guilin, China (15 min talk).
5. “Herschel First Results Symposium” (ESLAB 2010), 05.2010, ESTEC, Noordwijk, Netherlands (poster).